European GDR

Centre National
de la Recherche
Scientifique

European Research Network

Eighth meeting

Wave propagation in complex media for quantitative and Non-Destructive Evaluation

Gregynog Hall, Wales

23rd to 27th June 2014

EPSRC
Engineering and Physical Sciences
Research Council

RCNDE
UK Research Centre in
Nondestructive Evaluation

Welcome to the GDRE workshop !

The organisers of the GDRE are delighted to welcome all participants to the workshop being held in the week 23rd to 27th June 2014.

As you will have seen, this is the eighth meeting of our successful research network. Welcome back friends and colleagues who have attended previous meetings, and especial welcome to new participants of the GDRE. As in previous years, the venue has been carefully chosen so that delegates can get away from the usual distractions of life and focus on science in a convivial and stimulating environment. We hope you enjoy this year's venue, Gregynog Hall, which is renowned for its beautiful location, its elegant buildings, its interesting history, and its excellent chef !

Thank you to the participants who have submitted abstracts for a full programme of presentations, covering a wide range of topics within the interests of the GDRE community. Thank you also to all the researchers who have chosen to come to this workshop, to participate in the discussions and in continuing to support the important collaborations between French and UK researchers, and between applied mathematicians and engineers.

Many thanks to all who have contributed in the organisation of the conference, including Beatrice Desoudin (University of Bordeaux), Jenny Gradwell (University of Manchester), Rachael Evans (Gregynog Hall), and Richard Challis (University of Nottingham and Imperial College).

Please let us or Gregynog staff know if there is anything that you need.

We wish you a very happy and successful week.

The GDRE steering committee:
Marc Deschamps (University of Bordeaux – I2M)
Alain Leger (University of Marseille)
David Abrahams (University of Manchester)
Mike Lowe (Imperial College London)

Introduction to the European Research Network (GDRE)

Scope: Experiments, applied mathematics, numerics, and physical acoustics applied to Non-Destructive Evaluation in the fields of power generation, oil and gas engineering, civil infrastructure, aeronautics, automotive engineering and medicine

A CNRS research network Groupe de Recherche (GDR 2501) was started in France in 2002, and was joined by researchers in the UK in 2008. The network linked groups of academics and researchers in Ultrasonic Wave Phenomena with each other, and with industrial research centres and companies. The teams involved focused particularly on the theoretical end of the research spectrum, and include mathematicians, physicists and engineers, with applications to Non-Destructive Evaluation (NDE)..

The GDR was succeeded in 2011 by a new Network, which is now a European Research Network (GDRE) entitled *Wave Propagation in Complex Media for Quantitative and Non Destructive Evaluation*. In a similar manner to the GDR, this new network aims to give opportunities for interactions between researchers through informal meetings, workshops and colloquia, alternately in France and in the UK.

The research topics have evolved progressively and are now the following :

- scattering by thin layers and bonding
- material properties and metamaterials
- inverse problems and imaging
- material and contact nonlinearities in acoustics
- stratified and composite media, multidiffusion and structural noise

Gregynog Hall

The GDRE meeting in June 2014 is being held in Gregynog Hall, in Wales.

Gregynog (pronounced "gregg-gun-og") is a large country mansion in the village of Tregynon, 4 miles (6 km) northwest of Newtown in the old county of Montgomeryshire, now Powys, in mid Wales. There has been a settlement on the site since the twelfth century. From the fifteenth to the nineteenth centuries it was the home of the Blayney and Hanbury-Tracy families. In 1960 it was transferred to the University of Wales as a conference and study centre by Margaret Davies, granddaughter of the nineteenth century industrial magnate and philanthropist, David Davies 'Top Sawyer' of Llandinam.

The original mansion was rebuilt in the 1840s by Charles Hanbury-Tracy, 1st Baron Sudeley. Its concrete cladding, designed to replicate the black-and-white timber-framed architecture of Montgomeryshire farmhouses, is among the earliest examples of concrete use in building in the modern era. The Sudeleys were also pioneers of the use of concrete in the building of new cottages and farmhouses on the Gregynog estate, and many Cadw-listed examples can still be seen in Tregynon and the surrounding countryside. At its largest, the Gregynog estate was over 18,000 acres (73 km²) in extent, but the estate was broken up in 1913, leaving the mansion with 750 acres (3 km²) of farms, woodlands and formal gardens. The sunken garden and arboretum are of particular note.

Gregynog was bought by Margaret and her elder sister Gwendoline Davies in 1920 with the intention of establishing a centre of excellence for the arts, crafts and music which would enrich the lives of the people of Wales in the aftermath of the World War One. It became famous for music, fine printing and for the sisters' art collections which they bequeathed to the nation. These can now be seen in the Davies Galleries of the National Museum of Wales, Cardiff. Theirs was one of the most important British collections of French Impressionist and Post-Impressionist painting acquired before 1920. Their advisor Hugh Blaker was the younger brother of their governess Jane Blaker. The French collection was only one aspect of their interests – it hung at Gregynog alongside Old Masters, prints by Dürer, Rembrandt and Whistler, Chinese and Islamic ceramics, contemporary hand-made furniture commissioned by the sisters, Welsh vernacular furniture as well as contemporary ceramics and crafts. Seen as a whole, the sisters' collections are a tribute to the multiplicity and Catholicism of their tastes.

The Gregynog Music Festival, Wales's oldest surviving classical music festival, was established in 1933 by the Davies sisters, with the advice of their friend and advisor, Sir Henry Walford Davies (later Master of the King's Music). Many famous names are associated with the Gregynog Festivals, including Gustav Holst, Ralph Vaughan Williams, Edward Elgar and Sir Adrian Boult. The Festival is still held at Gregynog every June. In more recent years, leading international artistes have performed at Gregynog, including Benjamin Britten and Peter Pears. The sisters also established the Gregynog Press, which still exists under the name of Gwasg Gregynog, and is famous for its limited edition hand-printed books with fine bindings and exquisite wood-engraved illustrations

Since Margaret Davies's gift of Gregynog to the University of Wales in 1960, the hall has hosted a wide range of conferences, seminars and summer schools from every academic discipline, from International Politics to Welsh Literature to Fine Art, from Geography to Simultaneous Equations. The growing understanding of the ecological importance of the grounds, especially the ancient woodlands, has led to their designation in March 2013 as a National Nature Reserve. The training apiary of the Montgomeryshire Beekeepers Association is also situated in the Gregynog grounds.

(Information from Wikipedia)

Eighth Meeting of the GDR in Gregynog

23rd to 27th June 2014

Wave Propagation in complex media for quantitative and Non-Destructive Evaluation

Scientific Program

Monday, June 23rd 2014 - Morning

9:00 *Welcome*

9:30 **Dubus B. and Granger C.**, *Physical analysis of ultrasonic cavitation bubble structures observed at high intensity with horn transducers (invited)*

10:30 *Coffee break*

11:00 **Pinfield V.**, *Thermoelastic scattering in concentrated media: the Rayleigh limit for second order concentration effects*

11:30 **Mattesi V. and Tordeux S.**, *Equivalent source modelling of small heterogeneities in the context of 3D time-domain wave propagation equation*

12:00 **Luppe F., Conoir J.M. and Pareige P.**, *Dynamic mass density of random arrays of cylinders in an ideal fluid and the generalized self consistent method*

12:30 *Lunch*

Monday, June 23rd 2014 - Afternoon

14:00 **Yaacoubi S., Mckeon P., Yaacoubi W. and Declercq N.F.**, *Steps toward a new technique for improving guided waves detection sensitivity*

14:30 **Huthwaite P.**, *Thickness mapping by guided wave tomography*

15:00 **Treyssède F. and Laguerre L.**, *Excitation of prestressed multi-wire helical waveguides*

15:30 *Coffee break*

16:00 **Tant K. and Mulholland A.**, *A fractional Fourier transform analysis of the scattering of ultrasonic chirps*

16:30 **Yaacoubi W. and Yaacoubi S.**, *Issues to reduce false calls in guided waves structural health monitoring: survey and discussion*

17:00 **Nguyen K.L., Treyssède F., Hazard C. and Bonnet-Ben Dhia A.S.**, *Finite element computation of leaky modes in straight and helical elastic waveguides*

19:30 *Dinner*

Tuesday, June 24th 2014 - Morning

9:00 **Habault D.**, *ESAA Project - Toward an active anechoic room (invited)*

10:00 **Parnell W.J., Shearer T. and Abrahams D.**, *Elastic wave scattering in pre-stressed nonlinear inhomogeneous materials*

10:30 *Coffee break*

11:00 **Fan S., Choi W., Skelton E., Lowe M. and Craster R.**, *The validity of the 3D elastic Kirchhoff approximation for rough crack scattering signals using a finite element approach*

11:30 **Mora P., Ducasse E. and Deschamps M.**, *Elastodynamic response of an embedded layered anisotropic plate to a transient localized source*

12:00 **Kamta Djakou A., Darmon M. and Potel C.**, *The Uniform Theory of Diffraction (UTD) for elastic wave scattering from a half-plane*

12:30 *Lunch*

Tuesday, June 24th 2014 - Afternoon

14:00 **Carta G., Brun M. and Movchan A.**, *Wave propagation and localised modes in structures with diffuse cracks*

14:30 **Joyce D., Abrahams D. and Parnell W.J.**, *The higher order integral equation method of homogenization: antiplane elasticity*

15:00 **Hernando Quintanilla F., Lowe M. and Craster R.**, *Spectral Methods: An alternative to root-finding routines for finding dispersion curves of anisotropic homogeneous media*

15:30 *Coffee break*

16:00 **Haslinger S.**, *Flexural waves in structured elastic plates - trapped modes, transmission resonances and Elasto-Dynamically Inhibited Transmission (EDIT)*

16:30 **Sargent C.**, *Trapped modes in two dimensional waveguides*

17:00 **Massacret N., Moysan J., Jeannot J.P., Ploix M.A. and Corneloup G.**, *Development of ultrasonic propagation simulation for acoustic thermometry in liquid sodium*

19:30 *Welsh Speciality Dinner*

Wednesday, June 25th 2014 - Morning

9:00 **Barnwell E., Parnell W.J. and Abrahams D.**, *Tunable elastodynamic band-gaps*

9:30 **O'Neill J., Selsil O., Mcphedran R.C., Movchan A. and Movchan N.**, *Cloaking of finite inclusions for flexural waves in thin Kirchhoff plates using active control sources*

10:00 *Coffee break*

10:30 **Colquitt D., Brun M., Gei M., Movchan A., Movchan N. and Jones I.**, *Transformation platonics and cloaking*

11:00 **Thompson I.**, *Block wave excitation*

11:30 **Mansoura S.A., Marechal P., Morvan B. and Dubus B.**, *Active control of phononic crystals*

12:00 *Lunch*

Wednesday, June 25th 2014 - Afternoon

14:00 *Walk in countryside near Gregynog*

19:30 *Drinks Reception followed by Conference Dinner*

Thursday, June 26th 2014 - Morning

9:00 **Gunn D., Holyoake S. and Dashwood B.**, *Low frequency ultrasound propagation in layered media (invited)*

10:00 **Cunningham L. and Mulholland A.**, *A multi-frequency, model based method for sizing cracks in an elastic solid*

10:30 *Coffee break*

11:00 **Lowe M. and Fan Z.**, *Array imaging of austenitic welds by measuring weld material map*

11:30 **Li W. and Sharples S.**, *Spatially resolved acoustic spectroscopy: a laser ultrasonic technique for materials characterisation*

12:00 **Bai L., Velichko A. and Drinkwater B.**, *Ultrasonic Characterisation of Crack-Like Defects from Scattering Matrices*

12:30 *Lunch*

Thursday, June 26th 2014 - Afternoon

14:00 **Peake N.**, *The aeroacoustics of the owl (invited)*

15:00 **Destuynder P. and Favre C.**, *Remarks for non destructive testing in a bi-material based on Love waves*

15:30 *Coffee break*

16:00 **Baronian V., Bonnet-Ben Dhia A.S., Fliss S. and Tonnoir A.**, *Exact transparent boundary conditions for diffraction problems in some anisotropic plates*

16:30 **Junca S. and Legrand M.**, *Nonsmooth modal analysis of vibratory systems undergoing purely elastic impacts*

17:00 **Favrie N., Lombard B. and Payan C.**, *Nonlinear elasticity and slow dynamics: physical and numerical modeling*

19:30 *Dinner*

Friday, June 27th 2014 - Morning

9:00 **Pullen R. and Lawrie J.**, *Reflection and transmission at the junction between two sections of circular cylindrical shell*

9:30 **Nigro D. and Abrahams D.**, *Low mach number flow noise from a two-dimensional rough circular cylinder*

10:00 **Brun M. and Slepyan L.**, *Solution of a moving contact problem of dynamic elasticity*

10:30 *Coffee break*

12:00 *Lunch*

Physical analysis of ultrasonic cavitation bubble structures observed at high intensity with horn transducers

Bertrand Dubus and Christian Granger

Abstract
To optimise sonochemistry devices and develop scale-up strategies, it is important to predict how cavitation bubbles are spatially distributed when they are generated by high intensity ultrasonic transducers. The cavitation field generated by an ultrasonic axisymmetrical horn transducer at low frequency (20 kHz) and high acoustic intensities (1 to 10 W/cm^2) is found to self-organize into a conical bubble structure. This structure is constituted by cavitation bubbles which nucleate at horn surface, move parallel to it and finally leave it along streamers that constitute the cone. The presentation will describe the experiments and models developed to understand this nonlinear stochastic, multi-scale and multi-physical problem with analysis of: 1) the properties of the bubble structure at the microscopic and macroscopic levels; 2) the characteristics of the associated acoustic field; 3) the coupling of bubble and acoustic fields with the driving transducer.

Related references

A. Moussatov, C. Granger, B. Dubus, *Cone-like bubble formation in ultrasonic cavitation field*, Ultrasonics Sonochemistry, 10, 191-195, (2003).
C. Campos-Pozuelo, C. Granger, C. Vanhille, A. Moussatov, B. Dubus, *Experimental and theoretical investigation of the mean acoustic pressure in the cavitation field*, Ultrasonics Sonochemistry 12, 79-84, (2004).
V.N. Skokov, V.P. Koverda, A.V. Reshetnikov, A.V. Vinogradov, *1/f fluctuations under acoustic cavitation of liquids*, Physica A 364 (2005) 63-69.
B. Dubus, C. Vanhille, C. Campos-Pozuelo, C. Granger, *On the physical origin of conical bubble structure under ultrasonic horn*, Ultrasonics Sonochemistry, 17, 810-818, (2010).
B. Dubus, C. Granger, *Energy pumping by cavitation bubble cloud in low-frequency ultrasonic horn-type devices*, Proceedings of Acoustics 2013, New Delhi, (2013).

Bertrand Dubus, Institut d'Electronique de Microélectronique et de Nanotechnologie, département ISEN, UMR 8520, 41 boulevard Vauban, 59046 Lille cedex, , bertrand.dubus@isen.fr
Christian Granger Institut d'Electronique de Microélectronique et de Nanotechnologie, département ISEN, UMR 8520, 41 boulevard Vauban, 59046 Lille cedex, , christian.granger@isen.fr

Figure 1. Pictures of the conical bubble structure at 20 kHz

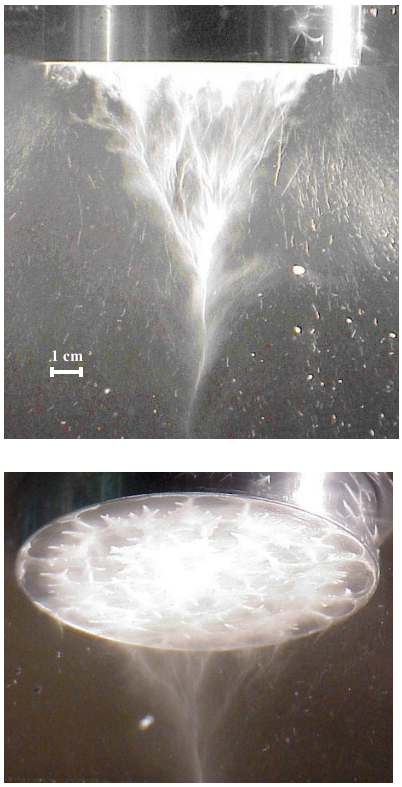

Thermoelastic scattering in concentrated media: the Rayleigh limit for second order concentration effects

Valerie J Pinfield

Abstract Multiple scattering effects for compressional wave propagation in concentrated dispersions are considered in the low frequency (Rayleigh) limit. This paper considers the additional contributions due to thermal "overlap", in which thermal waves produced by scattering of the compressional mode at an individual particle do not completely decay in the region between particles. Results are presented for the low frequency limit for the scattering coefficients (transition factors) for incident compressional and thermal waves, and for the dependence of the resulting speed and attenuation in the low frequency limit.

1 Introduction

Measurements of attenuation of a planar compressional wave propagating through a dispersion can be used to determine the concentration and/or particle size distribution of the dispersed particles. Whilst the single particle scattering problem for a spherical particle has a well-established solution, the multiple scattering of the compressional wave mode has not been well-defined. The most commonly used multiple scattering model is that of Lloyd and Berry[1] with similar results by Fikioris and Waterman[2], Waterman and Truell[3], and a more recent derivation by Linton and Martin[4]. However, these models consider only the multiple scattering contribution of the compressional mode itself; they neglect the contribution of thermal and shear waves to the exciting field at any particle. At low frequencies, the thermal and shear wave decay lengths are sufficiently large for these waves to reach neighbouring particles at significant amplitude. Scattering at the neighbouring particle, with an incident (exciting) field of all three wave modes, produces further scattered waves. The effect of the additional thermal and shear contributions is to reduce the attenuation of a compressional wave propagating through the dispersion. Comparisons of experimental measurements of attenuation in suspensions and emulsions have confirmed that the compressional wave multiple scattering models are inaccurate at low frequencies where the thermal or shear wave overlap condition occurs.

Luppé, Conoir and Norris[5] have presented a modified multiple scattering model which includes the contributions of thermal and shear waves which were previously neglected. In their model, coherent waves of all three wave modes exist in

Valerie J Pinfield, Chemical Engineering Department, Loughborough University, Loughborough, LE11 3TU, UK, email: v.pinfield@lboro.ac.uk

the dispersion. The principal result (for applications relating to compressional mode propagation through dispersions) is the effective wavenumber of the compressional mode. In this paper, the contributions of the thermal multiple scattering terms are considered, which are of relevance in emulsions at high concentration.

2 Theory

Luppé, Conoir and Norris[5] present a solution for the effective wavenumber for a dispersion at low frequency (equation 36 of their paper). The solution is written as a series in concentration, in which the second order terms include the additional contributions due to thermal and shear wave overlap. These are expressed as infinite sums over scattering transition factors representing the conversion between wave modes of all types at a single particle. The focus of this paper is the extra contributions due to thermal effects.

Previous studies of scattering in emulsions have shown that for liquid in liquid systems, the zero-order transition factor (Rayleigh partial wave coefficient) is dominant. This factor incorporates the energy lost from the compressional wave by conversion into thermal waves. Therefore, the wavenumber equation can be simplified by considering only the zero order transitions for the incident compressional wave. In this case, the transition factor for conversion from an incident compressional wave into a thermal wave is relevant. This is combined with the conversion from an incident thermal wave to produce compressional waves. It is assumed again, that the zero order will dominate the process. Hence the additional term in the effective wavenumber for emulsions at low frequency is given by

$$\Delta\frac{K^2}{k_C^2}=-\frac{27\phi^2}{(k_C a)^6}\frac{k_C^3}{3k_T\left(k_C^2-k_T^2\right)}T_0^{CT}T_0^{TC} \tag{1}$$

where subscripts T and C represent thermal and compressional wave modes, k is the wavenumber of the continuous phase, for each mode, denoted by its subscript, K is the wavenumber of the compressional mode in the dispersion, ϕ is the volume fraction and a the radius of the particles. The transition factors are defined such that T_0^{CT} is the zero-order transition factor for an incident compressional wave converting to a thermal wave. It is important to note that the "low frequency" region requires all wave modes to have a wavelength much larger than the particle size. This is more restrictive than the common definition of the long wavelength region, which often only refers to the compressional wavelength.

In order to establish the low frequency limit of this term, the forms of the transition factors must be established. These take the low frequency limit

$$T_0^{CT} = -\frac{i(k_T a)(k_C a)^2}{3}\frac{\tau'\sigma}{\tau\sigma'}(\gamma-1)\left[1-\frac{\rho\Gamma_C'}{\rho'\Gamma_C}\right] \tag{2}$$

$$T_0^{TC} = -\frac{i(k_C a)(k_T' a)^2}{3}\frac{\tau'}{\tau}\left[1-\frac{\tau\Gamma_T}{\tau'\Gamma_T'}\right]\left(1+\mathrm{O}\left((k_T a)^2\right)\right) \tag{3}$$

where ρ is the density, γ the ratio of specific heat capacities, τ is the thermal conductivity and σ the thermal diffusivity. The thermal factors (temperature/wave potential) are denoted by Γ. Primed variables relate to the dispersed phase, and unprimed are for the continuous phase.

The final terms in square brackets in each coefficient incorporate the difference in thermal properties between continuous and dispersed phases. Each reduces to

$$\left[1-\frac{\beta'/\left(\rho' C_p'\right)}{\beta/\left(\rho C_p\right)}\right] \tag{4}$$

where β is the thermal expansivity and C_p is the heat capacity. This illustrates its connection with the thermal property difference.

Substituting the low frequency expressions for the scattering coefficients into the effective wavenumber equation leads to

$$\Delta\frac{K^2}{k^2} = -\phi^2\frac{\tau'^2\sigma^2}{\tau^2\sigma'^2}(\gamma-1)\left[1-\frac{\beta'/\left(\rho' C_p'\right)}{\beta/\left(\rho C_p\right)}\right]^2\left(1+\mathrm{O}\left((k_T a)^2\right)\right) \tag{5}$$

To obtain the low frequency limit of speed, the following relationship can be applied

$$\frac{\Delta C}{C} \approx -\mathrm{Re}\left(\Delta\frac{K^2}{k^2}\right) \tag{6}$$

i.e. the fractional change in the speed of compressional wave propagation through the suspension. The low frequency limit of the real part of equation (5) is negative and independent of frequency, and therefore there is a small increase in wave speed due to the additional thermal terms, which is also independent of frequency.

The additional contribution to attenuation relates to the effective wavenumber as follows

$$\Delta\alpha = \frac{\omega C}{2c^2}\,\mathrm{Im}\left(\Delta\frac{K^2}{k^2}\right) \tag{7}$$

and this is expected to be negative i.e. a reduction in attenuation due to thermal overlap effects. Numerical results for the additional attenuation show that at low frequency

$$\mathrm{Im}\left(\Delta\frac{K^2}{k^2}\right) \propto -\omega \tag{8}$$

resulting in an attenuation which is proportional to the square of frequency. However, this dependence arises from higher order terms in the coefficients than those included in equations (2) and (3). The leading term in the coefficient T_0^{TC} is real (equation (3)), and therefore further terms of higher orders in frequency must be retained in order to obtain its imaginary part. It is this part which contributes to the attenuation component of the effective wavenumber.

8 Conclusion

The effects of thermal contributions to multiple scattering at low frequency result in an increase in speed of propagation of compressional waves which is independent of frequency. The attenuation is reduced, the reduction increasing linearly with frequency.

References

1. P. Lloyd, M. V. Berry, "Wave propagation through an assembly of spheres IV relations between different multiple scattering theories," Proceedings of the Physical Society, London **91,** 678-688 (1967).
2. J. G. Fikioris, P. C. Waterman, "Multiple scattering of waves II. "hole corrections" in the scalar case," J Math. Phys **5,** 1413-1420 (1964).
3. P. C. Waterman, R. Truell, "Multiple scattering of waves," Journal of Mathematical Physics **2,** 512-537 (1961).
4. C. M. Linton, P. A. Martin, "Multiple scattering by multiple spheres: A new proof of the Lloyd- Berry formula for the effective wavenumber," Siam Journal on Applied Mathematics **66,** 1649-1668 (2006).
5. F. Luppé, J. M. Conoir, and A. N. Norris, "Effective wave numbers for thermo-viscoelastic media containing random configurations of spherical scatterers," Journal of the Acoustical Society of America **131,** 1113-1120 (2012).

Equivalent source modelling of small heterogeneities in the context of $3D$ time-domain wave propagation equation

Vanessa Mattesi and Sébastien Tordeux

Abstract In the context of time harmonic wave equation, we are interested in the computation of the scattered field by a small obstacle. The result of a high performance direct numerical simulation is compared to an approximate solution derived by the method of matched asymptotic expansions.

1 Introduction

In the context of acoustic imaging, it is rather difficult to observe heterogeneities with characteristic length smaller than the wave length emitted by the scanner. However, it is possible to detect small heterogeneities in homogeneous media by using high performance computing. In this work, we will propose a way to compute the field scattered by a small obstacle with low computation burden based on the matched asymptotic expansions.

Vanessa Mattesi
Projet Magique-3D, INRIA Bordeaux Sud-Ouest, 200 avenue de la vieille Tour, 33405 Talence and LMA-UMR CNRS 5142, Université de Pau et des Pays de l'Adour, avenue de l'université, 64013 Pau, e-mail: vanessa.mattesi@inria.fr

Sébastien Tordeux
Projet Magique-3D, INRIA Bordeaux Sud-Ouest, 200 avenue de la vieille Tour, 33405 Talence and LMA-UMR CNRS 5142, Université de Pau et des Pays de l'Adour, avenue de l'université, 64013 Pau, e-mail: sebastien.tordeux@inria.fr

2 The considered problem

2.1 Domain definition

Let us consider a small obstacle $B_\varepsilon = \varepsilon\hat{B}$, equipped with Dirichlet boundary conditions, with $\hat{B}$ a reference shape and $\partial B_\varepsilon = \varepsilon\partial\hat{B}$ its boundary. The propagation domain Ω_ε consists of the exterior to the obstacle B_ε : $\Omega_\varepsilon = \mathbb{R}^3 \backslash B_\varepsilon$.

2.2 The system of partial differential equations

We denote by $f \in \mathscr{D}\left(\mathbb{R}^3 \times \overline{\mathbb{R}_+}\right)$ a source term satisfying : there exists $\varepsilon_0 > 0$ such that $f(\mathbf{x},t) = 0, \quad$ for $\|\mathbf{x}\| < \varepsilon_0$ and $t \geq 0$. Let us consider the solution of the $3D$ time-domain wave equation :

$$\frac{\partial^2 u_\varepsilon}{\partial t^2}(\mathbf{x},t) - \Delta u_\varepsilon(\mathbf{x},t) = f(\mathbf{x},t), \quad \mathbf{x} \in \Omega_\varepsilon,\ t \geq 0, \tag{1}$$

equipped with the Dirichlet boundary condition : $u_\varepsilon(\mathbf{x},t) = 0, \quad \mathbf{x} \in \partial\Omega_\varepsilon,\ t > 0$ and homogeneous initial conditions : $u_\varepsilon(\mathbf{x},0) = 0, \quad \partial_t u_\varepsilon(\mathbf{x},0) = 0$.
Remark. We have assumed that the wave speed is equal to 1.

3 Matching of asymptotic expansions

The matching of asymptotic expansions [1] is an asymptotic domain decomposition method with overlapping. It consists in representing the solution with a far-field expansion far away from the obstacle and a near-field expansion near the obstacle. These two expansions are matched in a transition zone with the so-called Van Dyke matching conditions. This approach is equivalent [3] to the corrector method [2].

3.1 The far-field expansion

The far-field expansion is defined on the far-field domain $\Omega_* = \mathbb{R}^3 \setminus \{\mathbf{0}\}$ consisting of the limit of Ω_ε for ε varying to 0. It takes the form of a Taylor series :

$$u_{\varepsilon,I}(\mathbf{x},t) = \sum_{i=0}^{I} u_i(\mathbf{x},t)\varepsilon^i. \tag{2}$$

The first term of this expansion $u_0 : \mathbb{R}^3 \longrightarrow \mathbb{R}$ is the limit of u_ε for ε varying to 0. It is a regular solution over all $\mathbb{R}^3$ of the time-domain wave equation :

$$\frac{\partial^2 u_0}{\partial t^2}(\mathbf{x},t) - \Delta u_0(\mathbf{x},t) = f(\mathbf{x},t), \quad \mathbf{x} \in \mathbb{R}^3,\ t > 0, \tag{3}$$

equipped with the initial conditions : $u_0(\mathbf{x},0) = 0, \quad \partial_t u_0(\mathbf{x},0) = 0, \quad \mathbf{x} \in \mathbb{R}^3$. The next coefficients $u_i : \Omega_* \longrightarrow \mathbb{R}$ of this expansion are solutions of the homogeneous time-domain wave equation :

$$\begin{cases} \dfrac{\partial^2 u_i}{\partial t^2}(\mathbf{x},t) - \Delta u_i(\mathbf{x},t) = 0, & \mathbf{x} \in \Omega_*,\ t > 0, \\ u_i(\mathbf{x},0) = 0, \quad \partial_t u_i(\mathbf{x},0) = 0, & \mathbf{x} \in \Omega_*, \end{cases} \tag{4}$$

which are singular in the neighbourhood of $\mathbf{x} = 0$. This power series aims at approximating the solution u_ε at fixed $\mathbf{x} \neq \mathbf{0}$: $u_\varepsilon(\mathbf{x},t) - u_{\varepsilon,I}(\mathbf{x},t) = \underset{\varepsilon \to 0}{O}(\varepsilon^{I+1})$.

3.2 The near-field expansion

The near-field domain $\widehat{\Omega}$ consists in the normalization of the original domain Ω_ε :

$$\widehat{\Omega} = \frac{\Omega_\varepsilon}{\varepsilon} = \left\{ (X,Y,Z) \in \mathbb{R}^3 : \varepsilon X, \varepsilon Y, \varepsilon Z \in \Omega_\varepsilon \right\} \tag{5}$$

The near-field expansion takes the form : $\sum_{i=0}^{+\infty} U_i(\mathbf{X},t)\varepsilon^i$, which aims at approximating $U_\varepsilon(\mathbf{X},t) = u_\varepsilon(\varepsilon\mathbf{X},t)$ at fixed $\mathbf{X} \in \widehat{\Omega}$. The coefficients of the near field expansion satisfy the hierarchical Laplace equation :

$$\Delta U_i(\mathbf{X},t) = \partial_t^2 U_{i-2}(\mathbf{X},t), \quad \mathbf{X} \in \widehat{\Omega},\ t > 0, \tag{6}$$

equipped with the Dirichlet boundary condition : $U_i(\mathbf{X},t) = 0, \quad \mathbf{X} \in \partial\widehat{\Omega}$, where we have used the convention $U_i \equiv 0$ for $i < 0$.

3.3 The second order far-field expansion

In the case of a spherical obstacle, $B_\varepsilon = \left\{ \mathbf{X} \in \mathbb{R}^3 : \|\mathbf{X}\| \leq \varepsilon \right\}$, the second order far-field expansion is given by :

$$u_{\varepsilon,2}(\mathbf{x},t) = u_0(\mathbf{x},t) - \varepsilon \frac{u_0(0,t-R/c)}{R} - \varepsilon^2 \left(\frac{\partial_t u_0(0,t-R/c)}{R} \right), \tag{7}$$

with $R = \sqrt{x^2+y^2+z^2}$.

4 Results

In this section, we present the results of a numerical experiment. We are in $3D$, our computational domain is $B = \left\{ \mathbf{X} \in \mathbb{R}^3 : \|\mathbf{X}\| \leq 1 \right\}$ and the obstacle is B_ε with $\varepsilon = 0.05$. For the direct numerical simulation, the domain is $B \backslash B_\varepsilon$ whereas for the computation of the far-field expansion, the domain is the whole sphere B. The source term consists in a Rickert localized at point $S = (0, 0.3, 0.3)$.
We compare the second order far-field expansion given in section (3.3) to a direct numerical approximation of u_ε achieved with an Interior Penalty Discontinuous Galerkin Method (IPDG) associated to a second order BGT absorbing boundary condition and to a local space-time mesh refinement [4]. Numerically, we observe that at point $A = (0, 0.5, 0)$, the relative error defined by :

$$e_{rel}^{\varepsilon} = \left| \frac{u_\varepsilon(A,t) - u_{\varepsilon,2}(A,t)}{\max\limits_{\mathrm{t}} |u_\varepsilon(A,t)|} \right| \tag{8}$$

is lower than 6%.

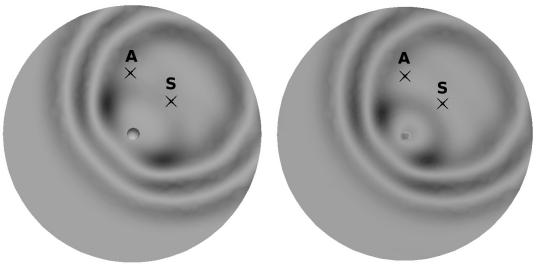

Fig. 1 Comparison between the direct numerical computation of u_ε (left) and its far-field expansion (right)

References

1. A. M. Il'in : Matching of asymptotic expansions of solutions of boundary value problems, *American Mathematical Society*, 1992.
2. V. Maz'ya, S. Nazarov and B. Plamenevskij : Asymptotic theory of elliptic boundary value problems in singularly perturbed domains, *Birkhuser Verlag*, Basel . Boston . Berlin, 2000.
3. M. Dauge, S. Tordeux and G. Vial : Self-similar perturbation near a corner : matching versus multi-scale expansions for a model problem.
4. J. Diaz and M.J. Grote : Energy conserving explicit local time stepping for second-order wave equations *SIAM J. SCI. COMPUT.*, vol. 31, No. 3, pp. 1985-2014.
5. S. Tordeux : Méthodes asymptotiques pour la propagation des ondes dans les milieux comportant des fentes, Thèse de l'Université de Versailles, 2004.

Dynamic mass density of random arrays of cylinders in an ideal fluid and the Generalized Self Consistent Method

F. Luppé, J.M. Conoir, P. Pareige

Abstract We consider a random array of elastic cylinders in an ideal (host) fluid. At low concentration of scatterers, the medium may be replaced by a homogeneous effective fluid that is characterized by a complex frequency dependent wave number and a complex frequency dependent mass density. Assuming one of those two to be known, we are interested in how the Generalized Self Consistent method may help in the determination of the other one.

1 Different expressions for the effective properties

Three different expressions of the effective wave number and three different ones of the effective mass density are used in the generalized Self Consistent Method (GSCM) in order to estimate the sensibility of the latter.

The expressions for the effective wave number K are:

* K_{WT}, given by Waterman and Truell's formula, usually agreed to be incorrect at order 2 of the concentration,
* K_{LM}, given by Linton and Martin [2], usually agreed to be correct at order 2 of the concentration as long as the radius of exclusion defined by Fikioris and Waterman's hole correction may be neglected,
* K_{ex}, which takes into account the radius b of exclusion, and tends to K_{LM} as the latter tends to zero. K_{ex} is given in Ref.[2] as well as in Ref.[5].

The expressions used for the effective mass density ρ are:

F. Luppé, LOMC, UMR CNRS 6294, Université du Havre, 75 rue Bellot, CS 80 540, 76058 Le Havre, France, francine.luppe@univ-lehavre.fr

J.M. Conoir, UPMC Univ Paris 06, UMR 7190, Institut Jean Le Rond d'Alembert, F-75005 Paris, France and CNRS, UMR 7190, Institut Jean Le Rond d'Alembert, F-75005 Paris, France, conoir@lmm.jussieu.fr

P. Pareige, LOMC, UMR CNRS 6294, Université du Havre, 75 rue Bellot, CS 80 540, 76058 Le Havre, France, pascal.pareige@univ-lehavre.fr

* ρ_{SA}, defined as the spatial average of the fluid and cylinders densities,
* ρ_1, an expansion of the effective mass density up to first order in concentration that takes into account the forward and backward form functions of the cylinders, as given for example by Aristegui and Angel [1],
* ρ_2, an expansion of the effective mass density up to order 2 in concentration that is equal to ρ_1 at first order, as given in Refs.[3,4].

Both densities ρ_1 and ρ_2 were found from the identification of the reflection coefficient at the plane interface between two fluids with the one at the plane interface between a fluid and that same fluid with a random array of scatterers within. ρ_2, however, was shown to depend on the incidence angle on the interface in Ref.[3], so that its validity remains to be checked. We use its expression for an incidence angle equal to zero in the GSCM.

2 The Generalized Self Consistent Method

After [5], the GSCM consists in equating the effective wave number K to that, ξ, obtained, with the same formula as that used for K, for a random array of cylindrical tubes in the effective fluid. Each tube consists in a cylinder, radius a, surrounded by a cylindrical ring of the ideal fluid, radius $a/\sqrt{c}$. As every formula for the wave number involves the scattering coefficients of the scatterers, ξ depends obviously on both K and ρ , and we investigate its sensitivity to both parameters. The numerical calculations are done for steel cylinders in water.

Using ρ_{SA} for the mass density shows that the Linton-Martin formula provides a better agreement than K_{WT} between K and ξ as was demonstrated in Ref.[5] in the Rayleigh limit.

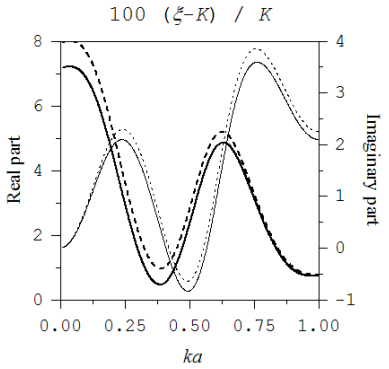

Figure 1: Relative difference between ξ and K for c=0.1 and $\rho=\rho_{SA}$. Thick lines : real parts. Thin lines : imaginary parts. Solid lines : $K=K_{LM}$, dotted lines : $K=K_{WT}$.

Using K_{LM} for the wave number shows that both ρ_1 and ρ_2 provide a better agreement than ρ_{SA} between K and ξ, but we cannot see any difference between the two mass densities ρ_1 and ρ_2 in Fig.2.

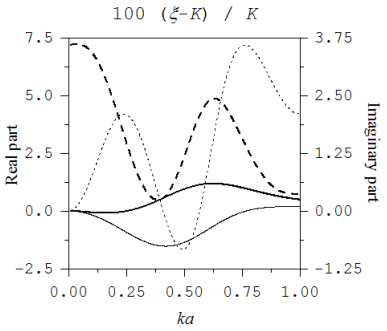

Figure 2: Relative difference between ξ and K for c=0.1 and K=K_{LM}. Thick lines : real parts. Thin lines : imaginary parts. Solid lines : ρ=ρ_2, dotted lines : ρ=ρ_{SA}.

In the Rayleigh regime, the modal series that appear in the expressions of ξ and K as well as in ρ_2 may be reduced to modes n=0 and n=±1 only, and the effective mass density may be looked for by solving the GSCM equation $K^2 = \xi^2$. Assuming that

$$\begin{aligned} \frac{K_{LM}^2}{k_0^2} &= 1 - 4\frac{i}{p}\frac{c}{k_0^2 a^2} f(0) - \frac{8}{p^2}\frac{c^2}{k_0^4 a^4} S_0 + O(c^3) \\ \frac{r}{r_0} &= 1 + \frac{r_1}{p}\frac{c}{k_0^2 a^2} + \frac{r_2}{p^2}\frac{c^2}{k_0^4 a^4} + O(c^3) \end{aligned} , \qquad (1)$$

with subscript 0 relating to the host fluid, one finds

$$\begin{aligned} r_1 &= -2i\left[f(0) + t_0 + 2t_1\right] \\ r_2 &= 2\left[f(0)^2 - 2S_0 + 2f(0)t_0 - 3t_0^2 - 4f(0)t_1 + 4t_0 t_1 - 4t_1^2\right] \end{aligned} , \qquad (2)$$

with t_n the scattering coefficient of order n of the cylinders.

Eq.(2) corresponds to the low frequency approximation of the formula given in Ref.[4] for ρ_2 .

As the frequency increases, however, K_{LM} has to be replaced with K_{ex}, and the corresponding approximation of ρ, which takes into account the radius b of exclusion, must be looked for. This is done in section 3.

3 Taking into account the radius of exclusion

Following the same procedure as in Ref.[3], we find the effective mass density ρ_{ex}, when taking into account the exclusion radius b.

Figure 3 shows the difference between taking into account an exclusion radius b between the cylinders equal to $2.01a$ along with an exclusion radius between tubes equal to $2.01\,a/\sqrt{c}$ and neglecting both exclusion radii in the GSCM.

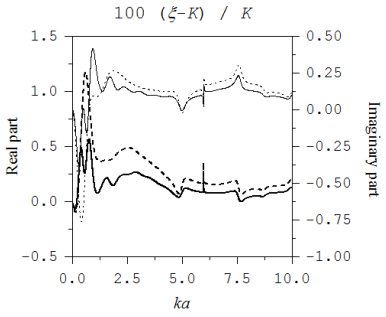

Figure 3: Relative difference between ξ and K for c=0.1. and K=K_{LM}. Thick lines : real parts. Thin lines : imaginary parts. Solid lines : K=K_{ex} and ρ=ρ_{ex}, dotted lines : K=K_{LM} and ρ=ρ_2.

4 Conclusion

The GSCM shows to be much more sensitive to the approximation used for the effective wave number than for the mass density. Numerics cannot thus prove with certainty that the second order in concentration we have found for the effective mass density is correct. It is only after the analytical study of the Rayleigh regime that we can hope it is correct.

References

1. C. Aristégui, Y.C. Angel, " Effective mass density and stiffness derived from P-wave multiple scattering", Wave Motion 44, 153-164 (2007)
2. C.M. Linton, P.A. Martin, "Multiple scattering by random configurations of circular cylinders : second-order corrections for the effective wavenumber", J. Acoust. Soc. Am. 117(6), 3413-3423 (2005)
3. F. Luppé, J.M. Conoir, "Multiple scattering by random configurations of cylinders in a fluid : effective properties", 6th conference of the GDR 2501 joined with the 10th anglo-french conference on physical acoustics, Lake District, UK, 18-22 janvier 2010, J. Phys. : Conf. Ser. 269 012015 doi:10.1088/1742-6596/269/1/012015
4. F. Luppé, J.M. Conoir, P. Pareige, "Dynamic effective properties of a random configuration of cylinders in a fluid", Proceedings of Forum Acusticum 2011, 2445-2449, European Acoustics Association Publisher, ISBN 8469415204, 9788469415207 (2011)
5. A.N. Norris, J.M. Conoir, "Multiple scattering by cylinders immersed in a fluid : High order approximations for the effective wavenumbers", J. Acoust. Soc. Am. 129 (1), 104-113 (2011)

Steps toward a new technique for improving Guided Waves detection sensitivity

S. Yaacoubi, P. McKeon, W. K. Yaacoubi, and N. F. Declercq

Abstract
Ultrasonic guided waves (UGW) techniques are increasingly used in Non-Destructive Testing as well as in Structural Health Monitoring fields. One advantage among others of the said technique is its propagation over long distances. To reach this, waves should be generated at relatively low frequencies. By increasing the wavelength, the defect sensitivity of this technique is consequently decreased. However, detection of early stages of damages is needed to ensure high level safety. In structures subjected to severe stresses, small defect can lead quickly to a rupture.
This communication suggests a method for high-sensitivity damage detection. The method is based on pitch-catch measurements of Lamb waves combined with a baseline subtraction technique in the frequency–wavenumber domain. Small amplitude converted modes, generated during the interaction of propagating waves with damage, can thus be detected with minimal a priori information regarding their expected location in the frequency–wavenumber plane. This method is applied in the present communication to a case of notches with varied depth. Finite element simulations are carried out in the temporal domain to mimic results obtainable in real-world experiments. Two cases are studied, namely when each of the two pure fundamental modes are incident on a notch. With regard to previous works using other methods, the developed method has proved a higher level of sensitivity. To determine the lower limit of sensitivity detection of this method, simulation was achieved in different cases:

- High variation of temperature,
- Large variation of random noise,
- Change in receiver positions

1 Principle and procedure of the method

For the sake of brevity, a brief description is given in this short paper; further details can be found in the conference presentation. The method is based on: UGW, pitch-catch arrangement, fixed emitter, one mobile sensor to accomplish the desired scan or many fixed sensors, an algorithm based on 2D-Fourier Transform.

Slah Yaacoubi
Institut de Soudure, 57970 Yutz, e-mail: s.yaacoubi@institutdesoudure.com

Peter McKeon
Geogea Tech Lorraine, 57070 Metz, e-mail: peter.mckeon@gatech.edu

This method is useful in the context of SHM as well as periodical NDT. The method is applicable for the inspection/monitoring of zones characterized as being crucial to structural safety and vulnerable to damage. Whether within the framework of SHM or periodical NDT, the data to be processed should be collected in two periods (P1 and P2). In the following, the steps are summarized:

I. *For period P1*

1. Fix one emitter (E) on one side of the zone to be tested/monitored and N receivers (Ri) on the other side of it. The receivers should be equidistant (distance between 2 successive receivers, Ri and Ri+1 with i = (1,.., N-1), is constant), and aligned in the direction of propagation;
2. Measure the time domain out-of-plane displacement at the first point (i=1);
3. Apply a rectangular window in time, which is chosen with regard to the distance between the emitter E and the receiver Ri to eliminate unwanted reflections. This window can be constant when the excited mode is non-dispersive, since the duration of the wave packet does not change length as a function of propagated distance.
4. Redo steps 1 and 2 for all receivers (Ri with i = (2,.., N)). The obtained data can be formed into a matrix (S) having dimensions N*M, where M is the size of the temporal vector (length of the sampled signal).
5. Pad with zeros if necessary, and apply a 2DFFT to S.

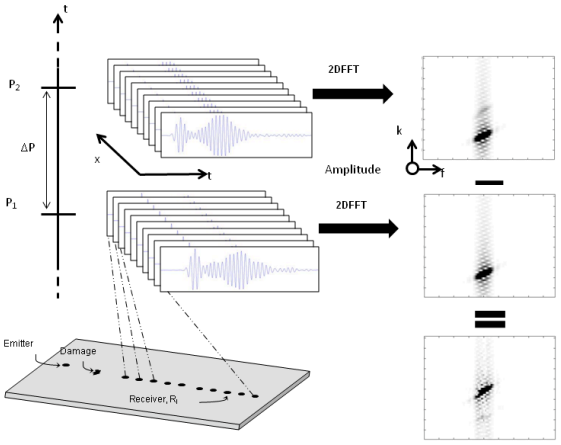

Figure 1: Diagram depicting the method based on the frequency-wavenumber domain baseline subtraction technique**.**

II. *For period P2, (P2 = P1 + ΔP), where ΔP is the time between the two periods P1 and P2*

1. Redo steps 1 to 5 maintaining initial positions from P1
2. Call an algorithm based on equation below:

$$\Gamma(f,k) = \left|2DFFT\left(u_D(t,x)\right)\right| - \left|2DFFT\left(u_B(t,x)\right)\right|$$

Based on the signal-processing steps, a code within the Matlab programming environment was developed. The inputs of this code are the data matrices S1 and S2, obtained respectively in the periods P1 and P2. This procedure and the code are schematically illustrated in Figure 1.

2 Robustness study

Some results of the variation of these factors (as in Figure 2 which concerns corruption of the acquired data by additional noise) will be shown during the presentation.

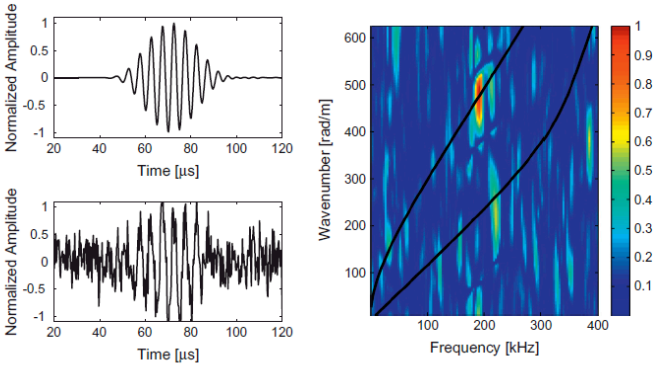

Figure 2 : Small amounts of a converted A0 mode detectable even in the presence of relatively low SNR

As it is well-known today, these parameters, whether environmental or operational, cause a problem in the baseline subtraction technique and so, compromise the reliability of SHM techniques. The method developed in the current study has better resistance than classic methods to these factors effects. Figure 2 shows the case of noise effect, without any compensation technique.

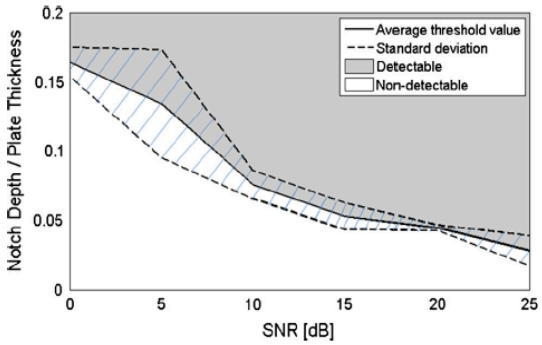

Figure 3 : Notch detectability threshold as a function of SNR. Due to the stochastic nature of noise, the threshold is displayed with standard deviation.

4 Advantages of the method and conclusions

The baseline subtraction technique has been applied to the frequency-wavenumber domain in order to increase the detectability of low amplitude modes. Such modes occur due to mode conversion when an incident wave interacts with damage such as a crack. Since the conversion coefficient is related to notch depth, detectability of low amplitude modes is directly related to the lower limit of damage detection. Through finite element analysis, mode conversion coefficients have been calculated for notch depths of less than 10% of the total plate thickness. The smallest notch depth detected has a depth of around 1.5% of the total plate thickness.

Spectral leakage, which occurs as a direct result of the signal being truncated, i.e. finite, can hide low amplitude converted modes. If a priori assumptions are made concerning the material properties and thickness of the sample, the location of the converted mode can be predicted in the 2DFFT. A novel approach takes the difference between a damaged 2DFFT and a healthy one. This frequency-wavenumber baseline subtraction method makes limited a priori assumptions, and makes low amplitude converted modes apparent. Since the detection floor is no longer determined by spectral leakage, relatively small damage can be detected as long as the signal-to-noise ratio is not a determining factor.

To conclude, the method has the following advantages:

- It improves damage detectability (detection of smaller defects); it allow for the detection of damage in early stage;
- It is applicable in the field of SHM as well as in periodical NDT (data acquired for a `healthy' sample should be saved, since it is the input of this signal processing technique). The technique is very sensitive to small evolution in damage size;
- Experimentally speaking, the method is easy to apply and not exorbitant. In SHM, the actuators/sensors (which are relatively inexpensive) live permanently with the structure and the data is automatically saved. In periodical NDT, a multi-element receiver can be used to save testing time. Evidently, all acquisitions should be taken with the same environmental conditions (temperature, humidity, pressure,...);
- The amount of assumptions made with a priori knowledge concerning structural characteristics (bulk velocities and geometrical dimensions) is minimal.

Thickness mapping by guided wave tomography

P. Huthwaite

Abstract Wall thickness mapping is very important for quantifying corrosion within the petrochemical industry. One approach is guided wave tomography, where Lamb-type waves, which travel at different speeds depending on the thickness due to dispersion, are passed through the region of interest. Wave speed is then reconstructed by a tomographic inversion approach, and is converted to thickness by the known dispersion relationship. Here, the accuracy of three approaches to thickness mapping is evaluated: ray tomography, diffraction tomagraphy, and a hybrid method combining the strengths of each. It is demonstrated that the hybrid method generates the best results, but that there is a fundamental resolution limit of around 2λ introduced by the thickness to velocity mapping, since the varying velocity map cannot accurately capture the guided wave scattering that occurs from small scale features. To achieve better resolution it is therefore necessary to use inversion models which more accurately capture the guided wave scattering from such features.

1 Introduction

In guided wave tomography, Lamb waves are excited within a plate-like structure and transmitted through a region of interest. For a plate of constant thickness, the velocity of the waves is a known function of the frequency-thickness product. This leads to the common approach used for guided wave tomography: a map of velocity is produced from measurements, then converted to thickness taking the known (fixed) frequency and using the relationship above. Despite this technique being widely used, (e.g. [1, 2]), it is unclear how slow the thickness variation must be for it to approximate constant thickness and hence be a valid assumption.

P. Huthwaite
Imperial College London, South Kensington, London, UK, SW7 2AZ e-mail: p.huthwaite@imperial.ac.uk

The accuracy of the algorithms used to produce the velocity reconstruction is also important. Three techniques are considered here. Firstly, ray tomography neglects diffraction and fits a velocity field to produce a set of arrival times matching those extracted from the measured data. Diffraction tomography is an alternative approach, based on the Born approximation [3]. Finally, we consider HARBUT (the hybrid algorithm for robust breast ultrasound tomography) [4], which has been developed to combine the complementary strengths of the previous two algorithms.

2 Theory

Lamb waves are guided elastic waves which travel in infinite plates of constant thickness. Figures 1(a) and (b) plot the phase velocity and group velocity dispersion curves respectively as a function of the product of plate thickness and frequency.

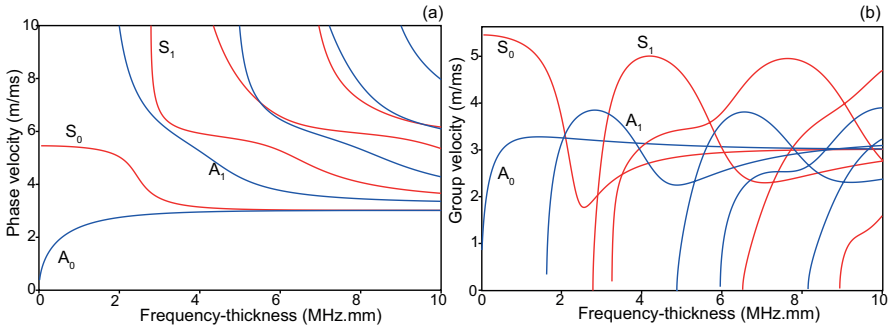

Fig. 1 Lamb waves in a steel plate. (a) gives the phase velocity dispersion curves, and (b) gives the group velocity.

Based on this, we make the assumption that the guided waves behave in the same way as they would within an acoustic medium with varying velocity, corresponding to the local frequency-thickness product. The acoustic model then needs to be inverted to produce a velocity map from acquired measurements. The first technique considered uses the ray approximation, which neglects diffraction. The eikonal equation reformulates the wave equation under ray theory, enabling it to be solved very quickly by an eikonal solver. Inversion then involves iteratively updating a velocity field until the eikonal solver produces arrival times which fit those extracted from the measurements. The resolution of this method is typically poor since the diffraction occurring with small scale defects prevents them from being detected [5].

Diffraction tomography uses the Born approximation to produce a reconstruction. The approximation replaces the total field interacting with the defect with the undisturbed incident field, and therefore assumes that the disturbance caused by the defect is small. Various approaches exist to determine the velocity field from a given

set of data based on this, such as the Fourier Diffraction Theorem [3]. Since the field must not be disturbed significantly, the approach is therefore limited to low contrast, small scatterers, but since the technique accounts for diffraction it is much higher resolution than ray tomography.

HARBUT [4] extends diffraction tomography to relax the requirement for weakly scattering reconstructions under the Born approximation. The approach is to use ray tomography to produce a low resolution reconstruction. Diffraction tomography is then applied on top of this to increase the resolution; the weakly scattering requirement now only applies to the small difference between the ray tomography background and the true field, so the approach is valid for a wider range of defects.

3 Defect analysis

A series of axisymmetric Hann-cross-sectioned defects in a 10mm thick plate were simulated using the finite element package Pogo [6]. The defects had depths from 5% to 60% wall loss, and widths of from 9λ down to 0.8λ, with the width being defined as the diameter where the defect first deviated from the uniform background and where $\lambda = 37$mm is the wavelength for the A_0 mode operating at 50kHz which was used for the simulations. A circular array of diameter 0.36m surrounded the defects, enabling illuminations and measurements to be made from all directions.

The three algorithms were then used to produce thickness reconstructions. The accuracy of these was evaluated and is plotted in Fig. 2(a). This figure plots regions as the defect varies in size and depth where the reconstruction has produced an acceptably accurate reconstruction, taken to be where the maximum thickness is within 10% of the true thickness and the RMS thickness is within 5%, with percentages given as a fraction of the 10mm nominal thickness. It is clear here that ray tomography only works well for larger defects, while DT is only suitable for small, shallow defects. HARBUT achieves good results for a large section of the plot, but seems to show a resolution limit around 2λ, marked by the dotted line.

A similar plot is shown in Fig. 2(b), but instead of using the full 3D elastic guided wave model to generate the test data, an idealised 2D acoustic model is used, where the varying thickness is replaced by equivalent variations in velocity. Since this set of data matches the acoustic models used in the inversion algorithms, it should enable the performance of the algorithms themselves to be evaluated. The conclusions for all three algorithms are simular to those outlined above, but now the overall resolution limit is around $\lambda/2$, marked, notably below the 2λ from before. This is effectively caused by the inaccuracies in the assumptions made by the thickness-to-velocity mapping; this assumption is only valid when thickness varies slowly. More rapid variations (typically of size less than 2λ) do not produce the same response from both models, which manifests itself as a resolution loss.

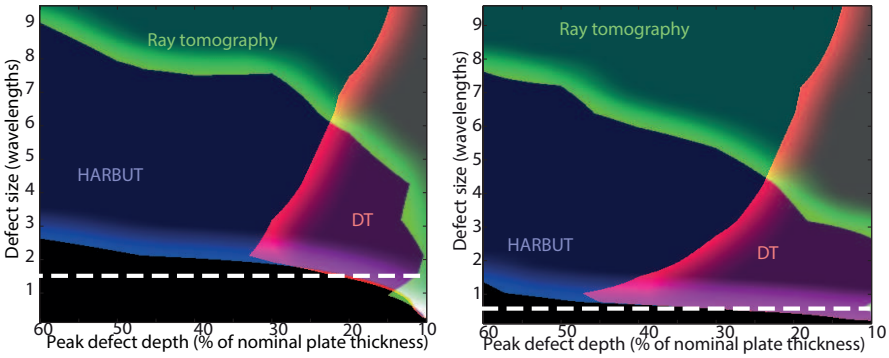

Fig. 2 Regions where the three algorithms produced reconstructions within 5% RMS of the true map, and within 10% variation of the peak wall loss. (a) presents results when test data is produced from a realistic guided wave model; (b) presents results for an idealised acoustic model.

4 Conclusions

This work has compared three different algorithms, ray tomography, diffraction tomography and HARBUT, a hybrid algorithm combining the features of the previous two algorithms. This has confirmed that ray tomography has poor resolution because it neglects diffraction, while diffraction tomography is restricted by the underlying Born approximation to weakly scattering defects. HARBUT, by comparison, generates good reconstructions for the majority of defects.

A fundamental resolution limit of around 2λ was shown for guided wave tomography when using realistic test data from guided wave models. This is caused because the acoustic reconstruction algorithms are unable to accurately describe the complex scattering of the guided waves which occurs when the waves interact with small defects.

References

1. A. Volker and J. Bloom, "Experimental results of guided wave travel time tomography," in *AIP Conference Proceedings*, vol. 1335, p. 215, 2011.
2. P. Huthwaite and F. Simonetti, "High-resolution guided wave tomography," *Wave Motion*, vol. 50, no. 5, pp. 979 – 993, 2013.
3. M. Born and E. Wolf, *Principles of Optics*. Cambridge: Cambridge University Press, 1999.
4. P. Huthwaite and F. Simonetti, "High-resolution imaging without iteration: a fast and robust method for breast ultrasound tomography," *Journal of the Acoustical Society of America*, vol. 130, no. 3, pp. 1721–1734, 2011.
5. P. Williamson, "A guide to the limits of resolution imposed by scattering in ray tomography," *Geophysics*, vol. 56, no. 2, pp. 202–207, 1991.
6. P. Huthwaite, "Accelerated finite element elastodynamic simulations using the GPU," *Journal of Computational Physics*, vol. 257, Part A, no. 0, pp. 687 – 707, 2014.

Excitation of prestressed multi-wire helical waveguides

Fabien Treyssède, Laurent Laguerre

Abstract Elastic guided waves are of interest for the non-destructive evaluation (NDE) of cables. Guided waves are multimodal and dispersive. Cables are complex structures, helical, multi-wired and highly prestressed. This further complicates the interpretation of measurement. Numerical models are required for understanding guided wave propagation and optimizing inspection systems. This paper reports on the modeling of wave propagation inside seven-wire strands, typically encountered in civil-engineering cables, including complicating effects such as geometry curvature and prestress. Special attention is given to the interwire energy transfer occurring in a seven-wire strand excited by a source localized in a single wire. Numerical results show how the energy transfer decreases with frequency, which leads to the discovery of a compressional mode of local type. This mode may have interesting features for the NDE of cables.

1 Introduction

Understanding wave propagation inside cables is a complicated task due to the structural complexity in addition to the multimodal and dispersive nature of guided waves. Cables are generally made of individual helical steel wires that are in contact and subjected to high tensioning forces. This work focuses on seven-wire strands, constituted by one central cylindrical wire and six peripheral helical wires, typically encountered in civil-engineering cables. Numerical tools are required for modeling wave propagation inside such complex structures. In this work, a semi-analytical finite element (SAFE) formulation is proposed. The formulation is specifically written in a non trivial twisting coordinate system and accounts for the effects of axial load.

IFSTTAR; GERS, AI, Route de Bouaye, 44344 Bouguenais, France, e-mail: fabien.treyssede@ifsttar.fr, laurent.laguerre@ifsttar.fr

2 Computation of guided modes

First, we briefly review the twisting SAFE method for the computation of guided modes in prestressed helical structures [1]. A SAFE approach consists in applying a time Fourier transform as well as a spatial Fourier transform along the waveguide axis z before discretizing the cross-section (x,y) by a finite element method. Inside one finite element e, the displacement field is thus expressed as follows:

$$\mathbf{u}(x,y,z,t) = \mathbf{N}^e(x,y)\mathbf{U}^e e^{i(kz-\omega t)} \tag{1}$$

where $\mathbf{U}^e$ is the nodal displacement vector and $\mathbf{N}^e$ is the matrix of nodal interpolating functions of the element e. The variational formulation of three-dimensional elastodynamics yields an eigenvalue problem of the following form:

$$\{\mathbf{K}_1 - \omega^2\mathbf{M} + ik(\mathbf{K}_2 - \mathbf{K}_2^T) + k^2\mathbf{K}_3\}\mathbf{U} = \mathbf{0} \tag{2}$$

In this work, one emphasizes that the equilibrium equations must be rewritten in a twisting coordinate system, defined by a non zero torsion τ. For clarity, the strain-displacement relation written in a twisting system is given by [2]:

$$\boldsymbol{\varepsilon} = (\mathbf{L}_{xy} + \mathbf{L}_z\partial/\partial z)\mathbf{u}, \quad \text{with: } \mathbf{L}_{xy} = \begin{bmatrix} \partial/\partial x & 0 & 0 \\ 0 & \partial/\partial y & 0 \\ 0 & 0 & \Lambda \\ \partial/\partial y & \partial/\partial x & 0 \\ \Lambda & -\tau & \partial/\partial x \\ \tau & \Lambda & \partial/\partial y \end{bmatrix}, \ \mathbf{L}_z = \begin{bmatrix} 0&0&0 \\ 0&0&0 \\ 0&0&1 \\ 0&0&0 \\ 1&0&0 \\ 0&1&0 \end{bmatrix} \tag{3}$$

where $\Lambda = \tau y\partial/\partial x - \tau x\partial/\partial y$. One points out that the expressions for $\mathbf{L}_{xy}$ and $\mathbf{L}_s$ do not depend on s, which proves that guided waves truly exist in helical structures [3].

Furthermore, the variational formulation must account for prestress effects and is augmented by the following additional term, sometimes referred to as geometric stiffness:

$$\int_{V_0} \mathrm{tr}(\nabla_0\delta\mathbf{u}\cdot\boldsymbol{\sigma}_0\cdot\nabla_0\mathbf{u}^T)dV_0 \tag{4}$$

where subscripts 0 are used for the prestressed configuration. $\boldsymbol{\sigma}_0$ denotes Cauchy prestress. In Eq. (2), each matrice must hence be augmented by a term related to the above geometric stiffness operator.

The FE mesh of the seven-wire strand cross-section is shown in Fig. 1a. We suppose that friction is high enough to prevent interwire slip. Figure 1b shows the energy velocity dispersion curves of a strand subjected to an axial tensile strain of 0.6%. Although dispersion curves exhibit a complex pattern, the figure particularly shows an apparent cut-off of the fastest mode (compressional-like $L(0,1)$ mode) around $\omega a/c_s = 0.44$, i.e. 86kHz for steel strands of 15.7mm nominal diameter. This phenomenon, sometimes referred to as 'notch frequency', coincides with experimental results of the literature [4, 5]. It actually corresponds to a sudden veering between two distinct branches [2], denoted as $L(0,1)a$ and $L(0,1)b$. Without load,

the notch frequency is centered around 0.36, i.e. 68kHz (results not shown for conciseness). Numerical experiments have shown that the phenomenon responsible for this frequency shift is indeed the increase of interwire contact area with the axial load.

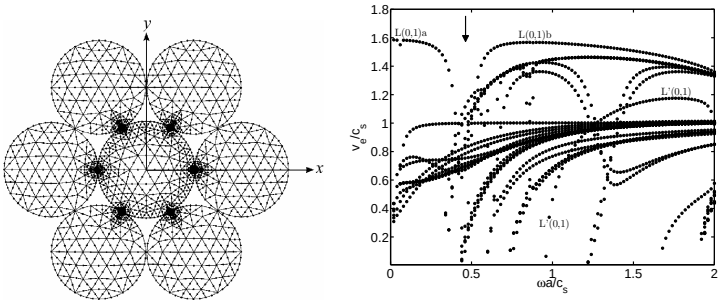

(a) (b)

Fig. 1: (a) Cross-section FE mesh of a seven-wire strand, (b) normalized energy velocity versus frequency under 0.6% tensile strain (the arrow indicates the notch frequency).

3 Response under excitation

Now, we are interested in solving the forced response problem, similar to Eq. (2) but with a non-zero excitation $\mathbf{F}(k)$ at the right hand side. The waveguide response can be obtained by expanding the solution as a sum of guided modes. Taking advantage of biorthogonality relations and applying the Cauchy residue theorem, the authors have shown in Ref. [6] that the SAFE solution as a function of $z > 0$ can be written as:

$$\mathbf{U} = \sum_{m=1}^{M} \alpha_m \frac{\mathbf{U}_m}{\sqrt{P_m}} e^{ik_m z}, \quad \text{with: } \alpha_m = \frac{i\omega}{4\sqrt{P_m}} \mathbf{U}_m^* \mathbf{F}(k_m) \tag{5}$$

The summation in Eq. (5) is performed over positive-going modes. P_m denotes the power flow of the mth mode. The above solution neglects the contribution of non-propagating modes. Viscoelasticity is not considered here.

One considers an excitation $\mathbf{F}$, normal to the cross-section, distributed over the cross-section of the central wire (half-sine function vanishing at its boundary) and concentrated at $z = 0$. One focuses on the transfer of energy from the central wire to the peripheral ones. The acoustic field of interest to quantify the wave energy is the power flow. We define η, the ratio of the power flow inside the six peripheral wires to the power flow of the whole seven-wire strand. Therefore, a small η means a weak energy transfer to the peripheral wires and inversely.

Figure 2a shows η as a function of frequency for a loaded strand (0.6% tensile strain). In the low frequency region, the energy transfer to peripheral wires is high. This is an expected result since the $L(0,1)$-like mode of a strand has a global behavior [2]. Then from $\omega a/c_s = 1$, η suddenly drops. This drop is indeed explained by the excitation of a new compressional-like mode, denoted as $L'(0,1)$ in Fig. 1b, whose motion is localized into the central wire. Figure 2b plots the modulus of the modal coefficients α_m of propagating modes. The power of the localized $L'(0,1)$ mode after its cut-on is clearly greater than the global $L(0,1)$ mode. This new mode could be of interest for NDE applications.

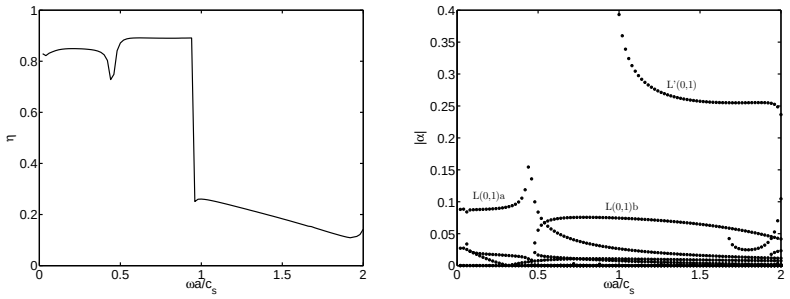

(a) (b)

Fig. 2: (a) Energy transfer ratio, (b) modulus of modal coefficients for a strand subjected to a 0.6% tensile strain

References

1. F. Treyssède, A. Frikha, and P. Cartraud. Mechanical modeling of helical structures accounting for translational invariance. Part 2: Guided wave propagation under axial loads. *International Journal of Solids and Structure*, 50:1383–1393, 2013.
2. F. Treyssède and L. Laguerre. Investigation of elastic modes propagating in multi-wire helical waveguides. *Journal of Sound and Vibration*, 329:1702–1716, 2010.
3. F. Treyssède. Mode propagation in curved waveguides and scattering by inhomogeneities: Application to the elastodynamics of helical structures. *Journal of the Acoustical Society of America*, 129:1857–1868, 2011.
4. H. Kwun, K. A. Bartels, and J. J. Hanley. Effects of tensile loading on the properties of elastic-wave propagation in a strand. *Journal of the Acoustical Society of America*, 103:3370–3375, 1998.
5. L. Laguerre, M. Brissaud, and J. C. Aime. Low-frequency ultrasound reflectometry device based on magnetoelastic transducers for the non destructive evaluation of steel rods and cables. *Bulletin des Laboratoires des Ponts et Chaussées*, 239:7–27, 2002.
6. F. Treyssède and L. Laguerre. Numerical and analytical calculation of modal excitability for elastic wave generation in lossy waveguides. *Journal of the Acoustical Society of America*, 133:3827–3837, 2013.

A Fractional Fourier Transform Analysis of the Scattering of Ultrasonic Chirps

Katherine Tant and Anthony. J. Mulholland

Abstract In this paper, a model for the scattering of an ultrasonic chirp in the far-field is derived in the time-frequency domain. The Fractional Fourier transform (FrFT) is applied to an inhomogeneous wave equation where the forcing function is prescribed as a linear chirp, modulated by a Gaussian envelope. Using the assumptions central to the Born approximation, an explicit expression for the scattered pressure wave is obtained. This model can be used to demonstrate the enhanced detection that the use of coded excitation permits and to design optimal chirp parameters for model-based, defect sizing algorithms.

1 Introduction

The use of coded excitations in signal processing has been shown to improve signal to noise ratio (SNR) and lessen trade-offs between sample penetration and image resolution [1] [2]. As the change of frequency with time is inherent to the nature of chirps, it seems natural to explore these signals within the time-frequency domain. This can be achieved through application of the Fractional Fourier transform (FrFT) [3]. Below, the inhomogeneous wave equation with a Gaussian modulated linear chirp forcing function has been solved in time-frequency space. An explicit expression for the resulting scattered wave is then obtained via the Born approximation [4]. By varying the parameter m (the rate at which the frequency increases in the linear chirp), comparisons can be drawn between chirp excitations and gated continuous wave excitations.

Katherine Tant
Department of Mathematics and Statistics, University of Strathclyde, Glasgow, U.K. e-mail: katy.tant@strath.ac.uk

Anthony J. Mulholland
Department of Mathematics and Statistics, University of Strathclyde, Glasgow, U.K. e-mail: anthony.mulholland@strath.ac.uk

2 The Fractional Fourier Transform

A linear chirp which has been modulated with a Gaussian envelope can be written.

$$s(t) = Re\left[\exp(\frac{-t_1^2}{\sigma^2})\exp(i\pi((2fm+\frac{i}{\pi\sigma^2})t^2+2(f-\frac{it_1}{\pi\sigma^2})t))\right]. \quad (1)$$

Here, f is the initial frequency, m is the rate of frequency increase, t_1 is the centre of the Gaussian peak and σ is its standard deviation. Letting $\chi = 2fm + i/\pi\sigma^2$ and $\xi = f - it_1/\pi\sigma^2$, the FrFT of equation (1) in terms of u, the independent variable, is [3]

$$s_a(u) = \exp\left(\frac{i\pi}{4}-\frac{t_1^2}{\sigma^2}\right)\frac{\sqrt{1-i\cot\alpha}}{\sqrt{\chi-\cot\alpha}}\exp\left(\frac{i\pi(u^2(\chi-\tan\alpha)+2u\xi\sec\alpha-\xi^2\tan\alpha)}{1+\chi\tan\alpha}\right) \quad (2)$$

where α dictates where in the time frequency domain u lies. Allowing the Gaussian modulated linear chirp (equation (1)) to be a spatially independent forcing function, the inhomogeneous wave equation is given

$$\frac{\partial^2}{\partial t^2}p(\mathbf{x},t) - c^2\nabla^2 p(\mathbf{x},t) = s(t). \quad (3)$$

From [3], its FrFT can be written

$$(i2\pi)^2u^2\sin^2\alpha\, p_a(\mathbf{x},u) + i4\pi u\sin\alpha\cos\alpha\frac{\partial}{\partial u}p_a(\mathbf{x},u) + \cos^2\alpha\frac{\partial^2}{\partial u^2}p_a(\mathbf{x},u) = c^2\nabla^2 p_a(\mathbf{x},u) + s_a(u). \quad (4)$$

3 Solving the Inhomogeneous Wave Equation in the Time-Frequency Domain

To solve equation (4), set $p_a(\mathbf{x},u) = g(u)h(\mathbf{x})$ and, using separation of variables, the following equations can be derived

$$\cos^2\alpha g''(u) + i4\pi u\sin\alpha\cos\alpha g'(u) - (4\pi^2u^2\sin^2\alpha - b^2)g(u) = 0 \quad (5)$$

and

$$\nabla^2 h(\mathbf{x}) + \frac{b^2}{c^2}h(\mathbf{x}) = \frac{s_a(u)}{c^2 g(u)} = f(u). \quad (6)$$

Here, we have a variable b which, when $\alpha = 0$ and $m = 0$ (a gated continuous wave in the time domain), is equal to the circular frequency ω. However, inherent to a chirp is a continuum of frequencies and so, when $m \neq 0$, b is not constant but a continuous variable related to the frequencies contained within the chirp. Due to its

relationship to the wavenumber, b/c will now be denoted $\hat{K}$. By imposing a radiation condition, the general chirp-like solution to equation (5) is given by

$$g(u) = C_1 \exp(u(-i\pi u \tan\alpha - \sqrt{-b^2 \sec^2\alpha + i2\pi \tan\alpha}). \tag{7}$$

Setting $h(\mathbf{x}) = h^{inc}(\mathbf{x}) + h^{scatt}(\mathbf{x})$, an expression for the scattered pressure at point $\mathbf{y}$ has been derived

$$\begin{aligned} h^{scatt}(\mathbf{y},b) = {} & \frac{\exp(i\hat{K}r_s)}{4\pi r_s} \int_{V_f} (-i\hat{K}\gamma_\rho(\mathbf{e}_s \cdot \nabla h(\mathbf{x}_s,b)) - \hat{K}\gamma_\lambda h(\mathbf{x}_s,b)) \exp(-i\hat{K}\mathbf{x}\cdot\mathbf{e}_s) dV_f \\ & + \frac{\exp(i\hat{K}r_s)}{4\pi r_s} f(u) \int_{V_f} \exp(-i\hat{K}\mathbf{x}\cdot\mathbf{e}_s) dV_f \\ & + \frac{\exp(i\hat{K}r_s)}{4\pi r_s} f(u) \int_{V_1} \exp(-i\hat{K}\mathbf{x}\cdot\mathbf{e}_s) dV_1, \end{aligned} \tag{8}$$

where r_s is the distance of $\mathbf{y}$ from the surface of the scatterer at $\mathbf{x}_s$ (working in the far field it is assumed $|\mathbf{y}| \gg |\mathbf{x}|$), $\gamma_\rho = 1 - \rho_0/\rho_1$ and $\gamma_\lambda = 1 - \lambda_0/\lambda_1$, where ρ_0, ρ_1 are the densities in the host and flaw materials respectively and λ_0, λ_1 represent the bulk moduli. $\mathbf{e}_s$ is the unit vector in the scattered wave direction and V_f denotes the flaw volume whilst V_1 is the region which lies between the flaw and reception points. Applying the central assumption of the Born Approximation (that the host and flaw materials are similar), the pressure field and its derivatives can be obtained from the incident wave only [4]. Since this work is based on transmission and reception in the far field, the spatial component of the incident wave can then be approximated by a plane wave, $h^{inc} = \exp(i\hat{K}\mathbf{e}_i \cdot \mathbf{x})$. Using these assumptions and the relationship

$$h^{scatt}(\mathbf{y},b) = \rho_0 A(\mathbf{e}_i;\mathbf{e}_s) \frac{\exp(i\hat{K}r_s)}{4\pi r_s}, \tag{9}$$

the scattering amplitude $A(\mathbf{e}_i;\mathbf{e}_s)$, with forcing function $f(u)$ incident in direction $\mathbf{e}_i$ and scattered in direction $\mathbf{e}_s$, can be written

$$\begin{aligned} A(\mathbf{e}_i;\mathbf{e}_s) = {} & -a_1a_2a_3 \frac{\gamma_\lambda - \gamma_\rho(\mathbf{e}_i\cdot\mathbf{e}_s)}{|\mathbf{e}_i - \mathbf{e}_s|^2 r_e^2} \left(\frac{\sin(\hat{K}|\mathbf{e}_i - \mathbf{e}_s|r_e) - \hat{K}|\mathbf{e}_i - \mathbf{e}_s|r_e \cos(\hat{K}|\mathbf{e}_i - \mathbf{e}_s|r_e)}{\hat{K}|\mathbf{e}_i - \mathbf{e}_s|r_e} \right) \\ & + \frac{a_1a_2a_3}{\rho_0} \frac{f(u)}{\hat{K}r_e} \left(\frac{\sin(\hat{K}r_e) - \hat{K}r_e\cos(\hat{K}r_e)}{\hat{K}^2 r_e^2} \right) \\ & + \frac{a_1a_2a_3}{\rho_0} \frac{f(u)}{\hat{K}r_e} \left(\frac{\hat{K}r_e\cos(\hat{K}r_e) - \sin(\hat{K}r_e) - \hat{K}r_s\cos(\hat{K}r_s) + \sin(\hat{K}r_s)}{\hat{K}^2 r_e^2} \right), \end{aligned} \tag{10}$$

where the flaw has been modelled as an ellipsoid with dimensions a_1, a_2 and a_3 and r_e is the effective flaw radius. Substituting equation (10) into equation (9) and multiplying by equation (7), an explicit approximation of the time-frequency domain so-

lution, $p_a(\mathbf{x}, u)$, to the wave equation with a Gaussian modulated linear chirp forcing function, is obtained.

4 Conclusions and Future Work

An analytical framework for assessing the use of chirp excitations by ultrasonic arrays in the detection and classification of flaws has been derived. At present the formulation has focussed on the scalar wave equation (shear horizontal waves) and the Born approximation for the scattering terms, but this could easily be extended to the more general Navier equations. This framework also permits an analysis of the effects that the chirp parameters have on the scattering amplitude arising from a defect as received by the ultrasonic array. In addition, it will also allow the inverse problem concerned with recovering defect dimensions, when chirp insonification is used by the arrays, to be implemented.

References

1. M. O'Donnell: Coded Excitation System for Improving the Penetration of Real-Time Phased-Array Imaging Systems, *IEEE TUFFC*, V. 39, p. 341-351, 1992.
2. R.Y. Chiao, X. Hao: Coded Excitation for Diagnostic Ultrasound: A System Developer's Perspective, *IEEE TUFFC*, V. 52, p. 160-170, 2005.
3. H.M. Ozaktas, Z. Zalevsky, M.A. Kutay: The Fractional Fourier Transform with Applications in Optics and Signal Processing, John Wiley & Sons Ltd., Chichester, 2001.
4. L.W.Schmerr: Fundamentals of ultrasonic nondestructive evaluation: A modelling approach, Plenum Press, New York, 1998.

Issues to reduce false calls in Guided Waves Structural Health Monitoring: Survey and discussion

Weina K. Yaacoubi, and S. Yaacoubi

Abstract
Structural health monitoring (SHM) is an emerging technology, which offers the possibility to improve early stage damage sensitivity and so, the performance of mechanical structures. The fact that actuators and sensors leave permanently with these structures renders its interrogations more frequent than in classic Non-Destructive Testing. The basic principle of this technology is: the data acquired, at different periods (or spaces), are used as inputs of algorithms based on baseline subtractions, and this allows consequently being more sensitive to small defects. To ensure the desired reliability of this technology, the data (and so the built data-base) should be acquired in the same conditions such as operational and environmental. However, in real life, temperature, wind, humidity, rain, electronic noise, loadings, etc. are not stable and change stochastically. Moreover, equipment aging (sensors, wires-sensors attachments, cables…) influence also the measurements. This impact significantly this data and generate consequently false-calls. All SHM techniques including ultrasonic guided waves (UGW) are exposed to this kind of problem. Many worldwide researchers are aware by these constraints which can render the promising SHM technology not efficient at all. Signal processing and statistical tools are developed especially the last decay to overcome (or at least reduce the effects of) these serious complications. Works are nowadays numerous. This communication focuses on UGW technique and presents a deep and concise survey of most previous works which are applied or can be applied to make it more reliable. The advantages and limitations of each tool will be discussed.

Weina K. Yaacoubi
Name, Address of Institute, Espace Cormontaigne, 4 Bvd Henri Becquerel, 57970 Yutz, France
w.ke@institutdesoudure.com

Slah Yaacoubi
Institut de Soudure, Espace Cormontaigne, 4 Bvd Henri Becquerel, 57970 Yutz, France
s.yaacoubi@institutdesoudure.com

Finite element computation of leaky modes in straight and helical elastic waveguides

K. L. Nguyen, F. Treyssède, C. Hazard, A.-S. Bonnet-BenDhia

Abstract Elastic guided waves are of interest for inspecting structures due to their ability to propagate over long distances. However, waveguides are often embedded in a large solid domain, considered as unbounded. The waves can attenuate strongly along the guide axis due to the energy leakage into the surrounding medium, which reduces the propagating distance. Searching modes with low attenuation becomes necessary. The goal of this work is to propose a numerical approach to compute modes in embedded elastic waveguides (straight and helical structures), combining the so-called semi-analytical finite element method (SAFE) and a perfectly matched layer (PML) method. The application of this work is the non destructive evaluation of multi-wire strands, which constitute cables in civil structures.

1 Introduction

For embedded structures, the energy leakage into the surrounding medium yields wave attenuation along the guide axis, which limits the application of guided wave technique for non destructive evaluation (NDE). An accurate determination of low leakage modes becomes necessary to maximize the inspecting range. Analytical tools have been developed to model simple geometries (plates and cylinders) [1, 2].

For complex geometries, modeling often relies on numerical approaches. A classical method is the so-called semi-analytical finite element (SAFE) method restricting the computational domain on the discretized waveguide cross-section. Yet, two difficulties are encountered for the numerical simulation of embedded waveguides : the unbounded cross-section and the presence of leaky modes whose amplitudes grow in transverse directions. To circumvent these difficulties, the SAFE method

K. L. Nguyen, F. Treyssède
IFSTTAR; Route de Bouaye, 44344 Bouguenais, France, e-mail: fabien.treyssede@ifsttar.fr

C. Hazard, A.-S. Bonnet-BenDhia
ENSTA Paris Tech; 828, Boulevard des Maréchaux, 91762 Palaiseau, France

has been combined with other techniques such as absorbing layer [3] and boundary element methods [4]. An alternative approach proposed in this paper is the perfectly matched layer (PML) method. A SAFE-PML approach has already been applied to model embedded solid plate waveguides in two dimensions [5].

The goal of this work is to extend this technique to model three-dimensional elastic waveguides buried in a solid matrix. First of all, the modeling of embedded straight waveguides is considered. The next step consists in applying the PML method in transverse twisting coordinates [6] to compute modes in embedded helical structures.

2 Straight waveguides

A PML applied along the Cartesian transverse directions (X,Y) consists in extending the elastodynamic formulation into complex coordinates $(\tilde{X}(X),\tilde{Y}(Y))$ to absorb waves in the surrounding medium: $\tilde{X} = \int_0^X \gamma_X(\xi)d\xi$, $\tilde{Y} = \int_0^Y \gamma_Y(\xi)d\xi$. A change of variable is then performed to transform the formulation back to real coordinates. In addition to the PML technique, the SAFE method is applied, which assumes an e^{ikZ} dependence, where k is the axial wavenumber and Z is the axial direction. The FE dicretization yields the quadratic eigenvalue problem :

$$\{\mathbf{K}_1 - \omega^2\mathbf{M} + ik(\mathbf{K}_2 - \mathbf{K}_2^T) + k^2\mathbf{K}_3\}\mathbf{U} = 0 \tag{1}$$

Numerical results are computed for a steel bar in concrete. The eigenspectrum at a given frequency shows that the PML method not only computes physical modes (leaky) but also non-intrinsic modes (radiation modes) which depend on PML characteristics and resonate mainly in the PML region. In order to eliminate radiation modes, a filtering criterion is applied, defined by the ratio of kinetic energy in the PML over the kinetic energy in the whole domain. As shown in Fig. 1, dispersion curves of leaky modes are well identified after filtering. Numerical results obtained by the SAFE-PML method are in agreement with Refs. [3, 4].

3 Helical waveguides

Helical waveguides must be considered in twisting coordinates (x,y,z) defined as :

$$x = X\cos(\tau Z) + Y\sin(\tau Z),\quad y = -X\sin(\tau Z) + Y\cos(\tau Z),\quad z = Z \tag{2}$$

where τ denotes the torsion of the (x,y) plane around the Z-axis.

The twisted PML method transforms twisted transverse coordinates (x,y) into complex ones $(\tilde{x}(x),\tilde{y}(y))$. Similarly to the previous section, a twisted SAFE-PML approach can then be applied.

3.1 Validation

Since a twisted cylinder remains a cylinder, this test case can be considered to validate the twisted SAFE-PML method.

The comparison between the axial wavenumbers computed in both coordinate systems (with twist and without) shows that the wavenumbers of compressional and torsional modes are unchanged while those of flexural modes are translated by $\pm\tau m$ in the twisting system, where m denotes the circumferential order (details in [6]).

Although the axial wavenumbers are different in twisting and straight coordinates, the physics of cylindrical modes are left unchanged. Figure 1 shows the agreement between the energy velocities in both coordinate systems.

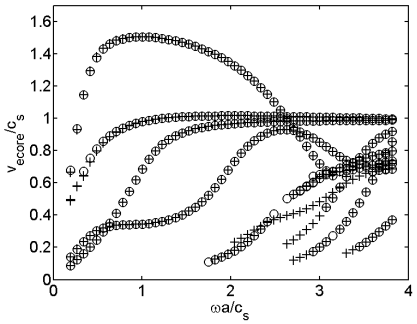

Fig. 1 Energy velocity for an embedded cylindrical bar obtained by SAFE-PML (circles) and twisted SAFE-PML (crosses) methods.

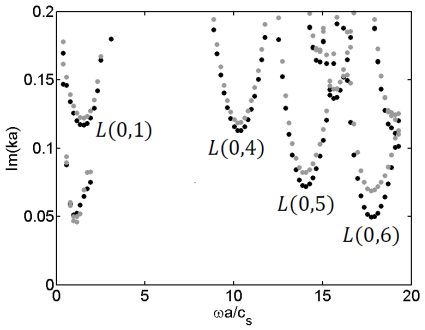

Fig. 2 Attenuation of modes in an embedded helical wire (black) and in an embedded cylindrical bar (gray).

3.2 Examples

Two examples of embedded helical waveguides are now considered : a steel helical wire and a steel seven-wire strand buried in concrete.

Figure 2 compares the axial attenuation of compressional $L(0,n)$ modes in an embedded helical wire with those of an embedded cylindrical bar. This comparison concentrates on compressional modes, which have low attenuations and high energy velocities. Compressional modes are more attenuated in a helical wire than in a straight one. This difference becomes more significant for high order modes. This result shows that the curvature of helical wires reduces the wave propagation distance and can make their NDE more difficult. This phenomenon has been observed for other kinds of curved waveguides [7].

The dispersion curves of energy velocity for a steel seven-wire strand in concrete is given by Fig. 3. The strand consists of one cylindrical bar surrounded by six

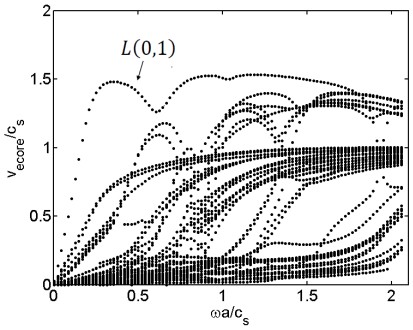

Fig. 3 Energy velocity of an embedded seven-wire strand.

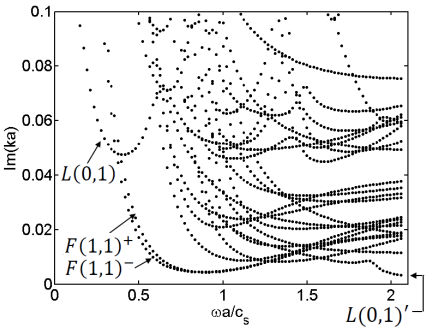

Fig. 4 Attenuation of modes in an embedded seven-wire strand.

helical wires. Comparing with the results of a free strand [6], the modal behaviour is strongly modified due to the introduction of the surrounding medium. The wave attenuation is shown in Fig. 4. $F(1,1)^{\pm}$ and $L(0,1)'$ modes have the lowest attenuations in the frequency range $[0, 1.5]$ and $[1.5, 2]$ respectively, which may be of interest for NDE. In addition to the attenuation due to the energy leakage, the surrounding medium has the other effect to make helical wires almost in contact, which further modifies the dispersion curves.

References

1. M. J. S. Lowe: Plate waves for the NDT of diffusion bonded titanium, *PhD Thesis Mechanical Engineering Department, Imperial College London*, 1992.
2. B. Pavlakovic: Leaky guided ultrasonic waves in NDT, *PhD Thesis Mechanical Engineering Department, Imperial College London*, 1998.
3. M. Castaings, M. Lowe: Finite element model for waves guided along solid systems of arbitrary section coupled to infinite solid media, *Journal of the Acoustical Society of America*, 123(2), 696-708, 2008.
4. M. Mazzotti, I. Bartoli, A. Marzani, E. Viola: A coupled SAFE-2.5D BEM approach for the dispersion analysis of damped leaky guided waves in embedded waveguides of arbitrary cross-section, *Ultrasonics*, 53(7),1227-1241,2013.
5. F. Treyssède, K. L. Nguyen, A. S. Bonnet-BenDhia, C. Hazard: On the use of a SAFE-PML technique for modeling two dimensional open elastic waveguides, *Acoustic*, Nantes France, 667-672, April 23-27, 2012.
6. F. Treyssède, L. Laguerre: Investigation of elastic modes propagating in multi-wire helical waveguides, *Journal of Sound and Vibration*, 329, 1702-1716, 2010.
7. M. D. Beard: Guided wave inspection of embedded cylindrical structures, *PhD Thesis Imperial College of Science, Technology and Medecine, University of London*, 2002.

ESAA Project - Toward an active anechoic room

D. Habault, Ph. Herzog, E. Friot, C. Pinhede

Abstract This is a presentation of some works in active control. Most of them were conducted by members of the LMA. We will show how these previous works have led to the project which is called “Active anechoic room” and is now carried out in the laboratory. The final aim of this project is to develop an active control system in order to increase sound absorption in the LMA anechoic room at low frequencies. Indeed, the characteristics of an anechoic room is to reduce the echoes coming from the walls in a very large frequency range. In the middle and high frequency range, this is very well achieved by covering the walls with absorbing materials. At very low frequencies (below 100Hz for example), this is more difficult but the active control systems are quite efficient at these frequencies and can be used as an additional tool to improve the acoustic performances of the passive system that is the coating on the walls. Apart from its practical applications, the study addresses more general questions related to sound synthesis and representations of sound fields and sources.

1 Introduction

For several tens of years the LMA has been contributing to a large amount of works on active sound control and the most recent studies concern both active control and sound synthesis (see [1, 2, 3] for example). The expertise gathered from these works is now used to carry out a project called “Active anechoic room” described in the abstract. The practical application of this project is to define and realise an experimental set-up in order to study acoustics radiation and propagation problems in a low frequency range and at short distances with a high accuracy. The general idea is therefore to add an active sound system to the existing passive system in the anechoic room.

Habault
LMA, CNRS-UPR7051, Aix-Marseille Univ, Ecole Centrale Marseille, 13402 Marseille Cedex 20, France, e-mail: habault@lma.cnrs-mrs.fr

2 Some LMA previous works in active control

A choice of three examples of works conducted at LMA is presented. The first one, the most classical, consists in minimising the sound field inside a volume. The original sound field is emitted by a source called primary source located outside the volume. The sound reduction is achieved by using secondary sources located at the boundary of the volume. These sources are driven from sound pressure measurements on microphones located inside the volume and by using specific algorithms such as LMS. It is well-known that this kind of system provides good results at low frequencies.

The second example is a sound synthesis example. The aim is to create a sound field with given characteristics in a volume inside a room. The sources are located on the walls of the room and a set of microphones is located on the boundary of the volume. A Green's formula is used to relate the sound pressure measured on the microphones to the sound pressure at any point in the volume. Then the system consists in driving the sources from measurements on the microphones. An experiment was carried out in a 2.7x1.7x2 m^3 room, in the 100-400 Hz frequency band.

In the third example, the aim is to minimise the sound pressure diffracted by an object in a room (see [1] and Fig. 1). The primary source is a loudspeaker located in a corner. The goal is that the sound pressure at the exterior microphones should be as close as possible to the incident pressure, that is the sound pressure that would exist in the room with no object. The total sound pressure is measured by interior microphones located around the object. The secondary sources are driven from the measurements obtained on these interior microphones. An integral equation is used to relate the total pressure on the exterior microphones to the total pressure on the interior microphones. The diffracted pressure is deduced from two series of measurements, with and without the object. An experiment was conducted in an anechoic room with the geometry shown in Fig. 1 at 280 Hz with an object of volume 1.6x0.9x0.5 m^3.

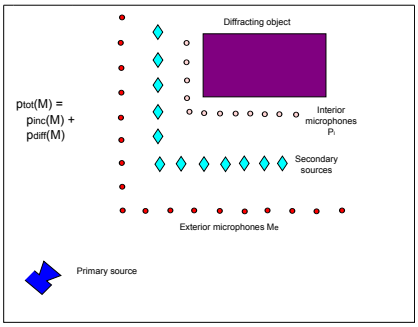

Fig.1 - Active control of the sound pressure diffracted by an object

3 The active anechoic room project

The aim of this project is to minimise the echoes coming from the walls of an anechoic room in order to increase the absorption efficiency of the coating (see Fig. 2) at a low frequency range. The source S is the primary source that we want to characterise accurately. The active control system is based on an array of loudspeakers located along the walls and driven by using pressure measurements on an array of microphones P_i located around the source. This is somewhat similar to the case of diffraction by an object described in the previous section. However, here, there is no direct way to assess the diffracted pressure. Therefore, this problem includes two steps : 1/ to estimate the diffracted pressure at point M ; 2/ to reduce the level of this diffracted pressure. Here, we only consider the first step, that is to develop a method in order to estimate the echoes arriving at point M.

Such a problem is modeled by using integral representations in order to obtain a relation between the total field measured on the microphones $p_{tot}(P_i)$ and the diffracted field at the observation point M $p_{dif}(M)$. At this stage, a monochromatic source is assumed, with an angular frequency ω. By using Green's formulas, it is possible to obtain the following representation :

$$p_{dif}(M) = (\mathscr{H}[p_{tot}])(M) \text{ pour } M \in \Omega \tag{1}$$

where the operator $\mathscr{H}$ is an integral operator over the surface of the array of microphones which represents the exterior boundary of the volume Ω. It can be shown that this operator exists and is uniquely defined but cannot be obtained explicitly, except in very simple cases. It must be remarked that it depends on the point M and the microphones P_i but does not depend on the source. This leads to a two-step method. A first set of sources is used to identify the operator by minimising the expression $|p_{dif} - \mathscr{H} p_{tot}|$. This is done by using a SVD method. Once a numerical approximation of $\mathscr{H}$ is obtained, the relation (1) can be used to compute the diffracted pressure for any other source.

The presentation will show some theoretical and numerical aspects of the study. From a numerical point of view, the effect of various parameters must be studied carefully, such as the number and positions of sources and microphones, the impedance on the walls and the frequency, etc. Because the problem solved is an inverse, ill-posed problem, the quality of the numerical results tightly depends on the way the physical characteristics of the problem and the final objective of sound reduction are taken into account.

4 Two examples of industrial applications

Two kinds of industrial applications of active sound control are finally described. For the first one, an active control system was designed in order to reduce the sound levels emitted by an electrical transformer. This system was first realised three years

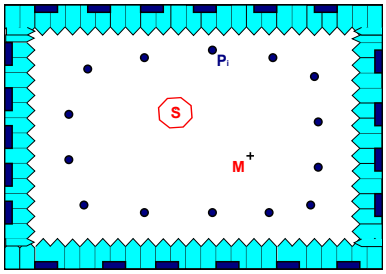

Fig. 2 - Active control of the sound pressure in an anechoic room

ago in an area of a Swiss city for the ATQ company and is still in use. The emitted signals are measured on a continuous time basis at several distances from the transformer. The second example is more similar to a sound synthesis experiment. It was conducted for Thales Alenia Space. The aim was to produce a diffuse sound field in a room used to test satellite responses to severe conditions (see Fig. 3). The sources are loudspeakers located along the walls which are driven at low frequency by an active control system.

Fig. 3 - Sound synthesis in a satellite testing room

References

1. E. Friot, R. Guillermin, M. Winninger : Active control of scattered acoustic radiation : A real-time implementation for a 3D object, *ActaAcustica*, v.92, p. 278-288, 2006.
2. M. Melon, Ph. Herzog, A. Sitel, M.A. Galland : One dimensional study of a module for active/passive control of both absorption and transmission", Applied Acoustics, v. 73(3), p. 234-242, 2012.
3. A.M. Pasqual, Ph. Herzog, J.R. de França Arruda : Theoretical and experimental analysis of the electromechanical behavior of a compact spherical loudspeaker array for directivity control, J. Acoust. Soc. Am, v. 128(6), p. 3478-3488, 2010.

Elastic wave scattering in pre-stressed nonlinear inhomogeneous materials

William J. Parnell, Tom Shearer and I. David Abrahams

Abstract The influence of hydrostatic pressure on the scattered elastodynamic field from a spherical cavity in an almost incompressible neo-Hookean medium is investigated. Small-on-large theory, coupled with matched asymptotics enables the scattering coefficients of the shear and compressible waves to be determined. A variety of interesting effects can occur associated with tuning the scattered response according to the imposed pressure.

1 Introduction

Inhomogeneous media are used extensively in the form of composite materials and arise naturally in various forms. Many such media are capable of large deformation and so there is a requirement to understand how linear acoustic or elastic waves propagate though such media when they are in a pre-stressed state. Predicting such fields is a non-trivial exercise due to the nonlinear deformations that arise being inhomogeneous. Wave propagation problems in pre-stressed hyperelastic media are typically restricted to the case of *homogeneous media* and *homogeneous deformations* so that the incremental wave will propagate through a homogeneous but anisotropic medium. On the other hand, *inhomogeneous* deformation leads the incremental wave to propagate in an anisotropic *and* inhomogeneous medium.

Before trying to understand the rather difficult multiple inhomogeneity problem, it would appear prudent to solve canonical problems associated with scattering from single inhomogeneities in pre-stressed materials. This was done recently for antiplane waves in neo-Hookean materials for two dimensional problems [1] where the rather surprising result that pre-stress does *not* modify the scattered field was deduced. This led to results associated with elastodynamic cloaking [2], [3], [4].

William J. Parnell e-mail: william.parnell@manchester.ac.uk · Tom Shearer e-mail: tom.shearer@manchester.ac.uk · I. David Abrahams e-mail: david.abrahams@manchester.ac.uk
School of Mathematics, University of Manchester, Oxford Road, Manchester, M13 9PL, UK

Mooney-Rivlin materials were subsequently studied in [5] and although the scattered field *is* affected by the pre-stress, its effect is still small.

The relative simplicity of the antiplane problem is assisted by the fact that both the deformation and incremental wave problems are incompressible. The extension to coupled compressional-shear waves in two or three dimensions is made more difficult by the requirement to include compressible effects. Here we shall describe the scattering of shear waves from a spherical cavity in a pre-stressed hyperelastic material and asymptotically exploit the fact that it is close-to-incompressible.

2 Asymptotic methodology

Consider an unbounded hyperelastic material, residing in which is a spherical cavity Ω of radius A. Subject the medium to a hydrostatic pressure p_∞ in the far field so that the cavity deforms radially to a cavity of radius a and an inhomogeneous deformation is generated within its vicinity. We wish to understand the effect that this nonlinear pre-stress has on scattering due to an incident incremental linear elastic shear wave. Wavelengths of the compressional and shear waves are λ_p, λ_s and wavenumbers are k_p, k_s such that $k_p A \ll 1$ but $k_s A = O(1)$. This means that the hyperelastic material is close to incompressible on lengthscales of $O(A)$ so that its ground state bulk modulus $\kappa \gg \mu$, its shear modulus. We consider the inhomogeneity and anisotropy to be restricted to a region that is small compared with the compressional wavelength but of the same order as the shear wavelength, see fig. 1. As such the *inner* region close to the cavity (and subject to inhomogeneous strain) can be treated as *incompressible*. On the other hand the outer region, far from the cavity is treated as *compressible*, homogeneous and isotropic. This enables us to treat the problem in terms of matched asymptotics, matching the incompressible inner solution to the outer, scattered field.

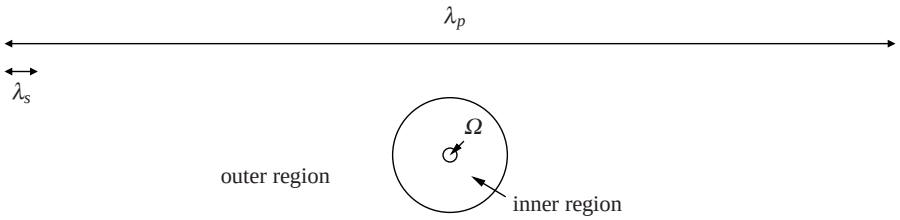

Fig. 1 Schematic diagram of inner and outer regions

3 Outer problem: scattered field

Pre-stress is confined to the inner region so that Navier's equation governs the displacements in the outer region:

$$(\lambda+\mu)\nabla(\nabla\cdot\mathbf{u})+\mu\nabla^2\mathbf{u}+\rho\omega^2\mathbf{u}=0 \tag{1}$$

where $\mathbf{u}$ is the displacement vector, λ and μ are the Lamé coefficients and time harmonic motion of frequency ω has been assumed. The incident wave is a plane shear wave propagating in the z direction and polarised in the x direction.

When the incident wave impinges upon the cavity both shear and compressional waves are scattered and the scattered field is decomposed as $\mathbf{u}_s=\mathbf{u}_{ss}+\mathbf{u}_{sc}$ with

$$\mathbf{u}_{ss}=\sum_{n=1}^{\infty}\frac{(2n+1)i^n}{n(n+1)}(a_n\mathbf{M}^3_{o1n}(\mathbf{r})-ib_n\mathbf{N}^3_{e1n}(\mathbf{r})),\quad \mathbf{u}_{sc}=\sum_{n=1}^{\infty}\frac{(2n+1)i^n}{n(n+1)}d_n\mathbf{L}^3_{e1n}(\mathbf{r}),$$

where a_n, b_n and d_n are the scattering coefficients associated with scattered decoupled shear waves, coupled shear waves and compressional waves respectively. The standard vector spherical harmonics $\mathbf{M}^3_{o1n}$, $\mathbf{N}^3_{e1n}$ and $\mathbf{L}^3_{e1n}$ are defined in [6]. Explicit expressions for scattering coefficients in the case of no pre-stress are given in [6].

4 Inner problem: pre-stress and incremental equations

Waves in the inner field are governed by incremental equations, derived from *small-on-large* theory and as such a nonlinear elasticity problem is first solved. We determine the fields that arise when hydrostatic pressure is imposed in the far field, deforming a spherical cavity inside an incompressible neo-Hookean material. Assume a deformation of the form $R=R(r),\Theta=\theta,\Phi=\phi$ where (R,Θ,Φ) and (r,θ,ϕ) are spherical polar coordinates in the undeformed and deformed configurations respectively. Imposed hydrostatic pressure coupled with incompressibility yields $R=(r^2+A^3-a^3)^{1/3}$ where a is the deformed cavity radius and it transpires that $\alpha=a/A$ is defined via

$$\frac{(4\alpha^3+1)}{2\alpha^4}-\frac{5}{2}=\frac{p_\infty}{\mu}. \tag{2}$$

The incremental equations are $\mathrm{div}\zeta+\rho\omega^2\mathbf{u}=0$ where $\zeta=\mathbf{M}:(\mathrm{grad}\mathbf{u})+q\mathbf{I}-Q\mathrm{grad}\mathbf{u}$ where Q is the known Lagrange multiplier associated with the large deformation and q is its perturbation, which is expanded into spherical harmonics with unspecified coefficients to be determined. For homogeneous deformations $\mathbf{M}$ has constant coefficients. Here, its only non-zero terms are

$$M_{rrrr}=M_{r\theta r\theta}=\frac{(r^3+A^3-a^3)^{4/3}}{r^4}\mu, \tag{3}$$

$$M_{\theta\theta\theta\theta}=M_{\phi\phi\phi\phi}=M_{\theta r\theta r}=M_{\theta\phi\theta\phi}=M_{\phi\theta\phi\theta}=\frac{r^2}{(r^3+A^3-a^3)^{2/3}}\mu \tag{4}$$

and the traction free boundary condition is imposed on $r=a$.

Separable solutions are posed for the displacement components with the same θ and ϕ dependency as the case of no pre-stress and unknown functions of r to be

determined from a set of coupled ODEs. In the inner region $a \leq r \leq b$ where $b \gg a$, the equations are solved numerically and linked at $r = b$ with the solution of incremental equations in $r > b$ (the outer extent of the inner region) which are obtained by removing the inhomogeneity from the ODEs since we are far away from the pre-stress. The solution associated with *homogeneity* in this region can be augmented, asymptotically by higher order corrections associated with effects of inhomogeneity. These mid-region solutions have the required spherical Bessel function form, with the exception of the compressible part which has algebraic decay. This is however sensible since we have assumed incompressibility in the inner problem. Using Van-Dyke's matching principle, we match this leading order inner field to the leading order outer field derived in (2) in order to determine the scattering coefficients. These have dependence on pre-stress by virtue of matching to the inner problem.

5 Results

As an example of the effect of pre-stress in figure 2 we plot the scattering cross-section, a measure of the incident energy scattered by the cavity [6] as a function of the imposed pre-stress for various values of k_sA. Note in particular the shifting of the minimum for each curve as a result of pre-stress.

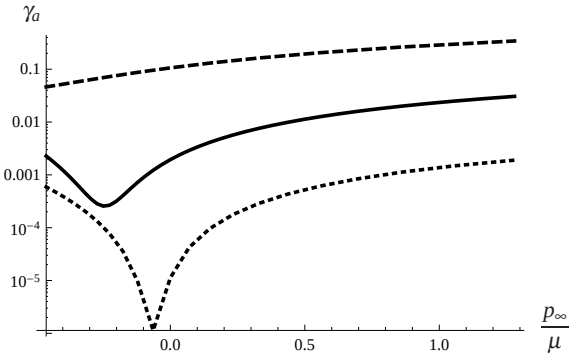

Fig. 2 The scattering cross-section γ_a as a function of p_∞/μ for various values of k_SA. The solid line corresponds to $k_sA = 1$, the dashed line corresponds to $k_sA = 2$ and the dotted line corresponds to $k_sA = 0.5$.

References

1. Parnell, W.J. and Abrahams, I.D. 2012. Antiplane wave scattering from a cylindrical void in a pre-stressed incompressible neo-Hookean material. *Commun. Comp. Phys.* **11**, 678–901.
2. Parnell, W.J. 2012. Nonlinear pre-stress for cloaking from antiplane elastic waves. *Proc. R. Soc. A* **468**, 563–580.
3. Parnell, W.J., Norris, A.N. and Shearer, T. 2012. Employing pre-stress to generate finite cloaks for antiplane elastic waves. *Appl. Phys. Lett.* **100**, 171907.
4. Norris, A.N. and Parnell, W.J. 2012. Hyperelastic cloaking theory: transformation elasticity with pre-stressed solids. *Proc. R. Soc. A* **468**, 2881–2903
5. Parnell, W.J. and Shearer, T. 2013. Antiplane elastic wave cloaking using metamaterials, homogenization and hyperelasticity. *Wave Motion* **50**, 1140–1152.
6. Einspruch, N.G. Witterholt, E.J. and Truell, R. 1960. Scattering of a plane transverse wave by a spherical obstacle in an elastic medium. *J. Appl. Phys.* **31**, 806–818.

The validity of the 3D elastic Kirchhoff approximation for rough crack scattering signals using a finite element approach

Fan Shi[1], Wonjae Choi[1], Elizabeth Skelton[2], Michael J.S. Lowe[1], and Richard Craster[2]

Abstract

The Kirchhoff approximation to calculate the elastic wave scattering from 2D rough cracks is examined by a comparison with a 3D finite element (FE) approach. This approach couples a time domain finite element solver and a hybrid method to compute the scattering signals from rough cracks. 2D random rough surface with Gaussian profiles are used in this paper to study the validity of the Kirchhoff approximation. Simulations are run as a function of incident/scattering angle, roughness, and band width of the input signal. Both the shape and the peak amplitude of the received signal are compared using the two different numerical approaches. Certain restricted ranges for the Kirchhoff approximation are found through the comparison with the FE method.

Fan Shi, Wonjae Choi and Michael J.S. Lowe are with
Department of Mechanical Engineering, Imperial College, London SW7 2 AZ, UK
f.shi12@imperial.ac.uk

Elizabeth Skelton and Richard Craster are with
Department of Mathematics, Imperial College, London SW7 2 AZ, UK

Elastodynamic response of an embedded layered anisotropic plate to a transient localized source

Pierric Mora [a], Eric Ducasse [b] and Marc Deschamps [c]

Abstract We present a method for computationally solving the following problem: given a general stratified medium and a localized transient source, what is the elastodynamic field at any finite time t and position (x,y,z). This work is aimed at modelling composite plates in vacuum, immersed in fluids or embedded in solid half spaces. A Fourier transform on the two in-plane space variables and a Laplace transform on the time variable are used. The 3D wave equation is analytically solved in this dual space. Then, the inverse transformations are performed. Concerning the Laplace variable, we use the well known Bromwich-Mellin formula, which can be computed via a fast Fourier transform. This results in the so-called Exponential Window Method [9, 4, 7]. We illustrate the method with the example of the generation of the S_1 Lamb mode of an aluminum plate immersed in water. Depending on the incidence angle, the group velocity of this mode can be either positive, zero or negative.

1 Statement of the problem

The wave equation in an anisotropic elastic solid, with a causal source term $\underline{\mathbf{f}}$, is:

$$\rho\, \partial_{t^2} \underline{\mathbf{u}} - (\nabla \diamond \nabla)\, \underline{\mathbf{u}} = \underline{\mathbf{f}} \quad . \tag{1}$$

The symbol $\diamond$ stands for a bilinear operator and contains the stiffness coefficients [3]. For the sake of simplicity, the viscoelastic case is not treated. Though, the method would be exactly the same. Equation (1) holds for each layer, and continuity of displacement $\underline{\mathbf{u}}$ and normal stress $\underline{\boldsymbol{\sigma}_z}$ connects the distinct regions.

[a] Univ. Bordeaux, I2M-APy, UMR 5295, F-33400 Talence, France, e-mail: pierric.mora@u-bordeaux.fr
[b] Arts et Métiers ParisTech, I2M-APy, UMR 5295, F-33400 Talence, France, e-mail: eric.ducasse@u-bordeaux.fr
[c] CNRS, I2M-APy, UMR 5295, F-33400 Talence, France, e-mail: marc.deschamps@u-bordeaux.fr

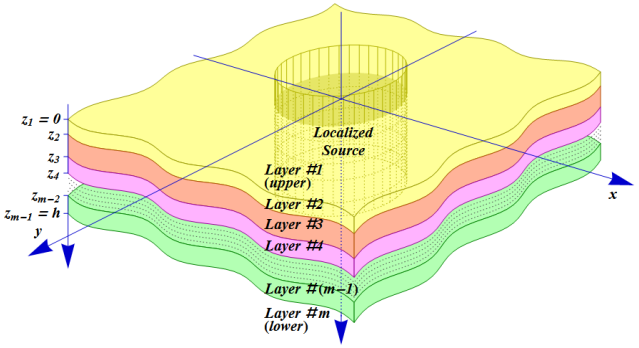

Fig. 1 The medium considered has a finite number m of layers. The first and last ones may be half spaces. Each layer can be a fluid, a solid, isotropic or anisotropic, and is possibly viscoelastic.

2 Analytical resolution in the dual space $(\mathbf{k}, z, s)$

We apply integral transforms on the two in-plane variables and on the time variable:

$\mathbf{x} \rightarrow \mathbf{k}$: Fourier transform,

$t \rightarrow s$: Laplace transform.

In this dual space, (1) is a linear ordinary differential equation on the z variable. The particular solution physically corresponds to the response of the source in an infinite space - which can be easily calculated with the Green tensor - while the complementary solution physically corresponds to the field refracted by the interfaces. The refracted field can be expressed in the basis of the 2x3 body waves, which are the eigensystem of the Stroh matrix [11, 5]. The continuity conditions on the interfaces lead to a "global matrix"-like linear system [6] on the body waves coefficients. The determinant of this system never vanishes as long as we set $Re(s) > 0$.

3 Numerical inverse transforms to the $(\mathbf{x}, z, t)$ domain

$\mathbf{k} \rightarrow \mathbf{x}$: standard use of FFT^{-1},

$s \rightarrow t$: use of the Bromwich-Mellin formula:

$$\begin{pmatrix} \mathbf{u}(t) \\ \boldsymbol{\sigma}_z(t) \end{pmatrix} = \frac{1}{2\,\mathbb{i}\,\pi} \int_{\gamma-\mathbb{i}\infty}^{\gamma+\mathbb{i}\infty} \begin{pmatrix} \mathbf{U}(s) \\ \Sigma_z(s) \end{pmatrix} \exp(st)\, \mathbb{d}s \quad , \tag{2}$$

which can be computed by a FFT^{-1}, the result being multiplicated by $\exp(\gamma t)$. The choice of γ in (2) is a numerical compromise. Indeed, for low values, the integration path can get too close to the singularities (see Fig. 2), the integration over frequencies is truncated too roughly and the temporal signal suffers a severe aliasing. This is particularly critical for waveguides in vacuum with no damping. On the other hand, if a high value of γ is chosen, the $\exp(\gamma t)$ factor rapidly magnifies a numerical noise

due to the spectrum truncation of the source term. This compromise is discussed in Refs. [4, 7]. One should then keep in mind that, according to the needs, any arbitrary precision can be reached, at the possible price of oversizing the temporal window.

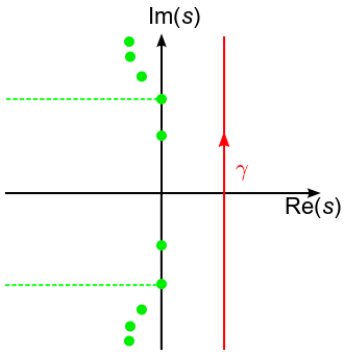

Fig. 2 Integration path in the complex plane for (2). Because of causality and of the stability of the system, all the functions are holomorph in $\mathbb{R}_+^\star + \mathrm{i}\,\mathbb{R}$. All the singularities (poles, branch cuts) are in the left part of the complex plane.

4 Example: S_1 Lamb mode with $c_g > 0$, $c_g = 0$ and $c_g < 0$

As an illustration we take the example of the S_1 Lamb mode of an aluminum plate immersed in water excited by an oblique square transducer sending a narrow band signal (30 cycles with a gaussian envelope). The transducer size is approximately 40 λ_{water} and the incidence angle θ is chosen to select different behaviors of the S_1 Lamb mode. As a complement to Refs. [1, 2] we display in Fig. 3 the displacement field in the time domain.

5 Conclusions

The Exponential Window Method coupled with a 2D space Fourier approach can solve the very general 3D case of localized transient sources radiating to multilayered half spaces. The solution can be obtained at any given precision. Therefore, concerning field calculation, this method is more versatile than a modal approach which would be fraught with difficulties in obtaining the complex radiating modes and working with the incomplete modal basis. Furthermore, the computer code can be highly parallelized, and the calculation speed is far fast enough for being run on a commercial personal computer.

Acknowledgements This work is led in the mark of a PhD. thesis supported by *Region Aquitaine* and *CEA-LIST*, which we acknowledge. We also strongly acknowledge J.L. Charles, P. Gay and R. Bouchouirbat for their advice in computational choices. Computer time for this study was provided by the computing facilities MCIA (Mésocentre de Calcul Intensif Aquitain) of the Université de Bordeaux and of the Université de Pau et des Pays de l'Adour.

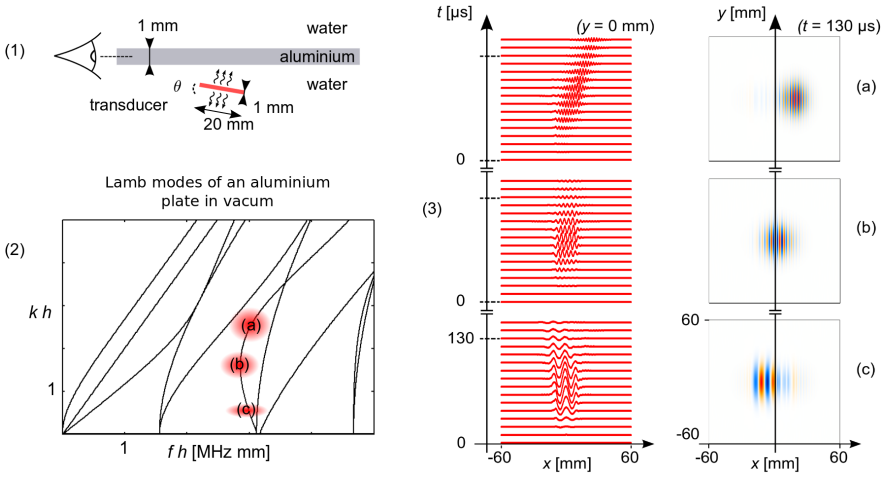

Fig. 3 (1) Side view of the setting. (2) Dispersion curves of the plate in vacuum, as a guideline for chosing the frequency and incidence angle ((a): f=3.0 MHz, $\theta = 12.0°$ (b): f=2.87 MHz, $\theta = 7.7°$ (c): f=3.0 MHz, $\theta = 2.6°$). In this S_1 region, the influence of the fluid loading is low [8, 10]. (3) S_1 Lamb mode with (a) positive, (b) zero, (c) negative group velocity. On the left side, the fields are viewed from the side with time running, on the right side the view is from the top at fixed time. As a result of worse impedance matching the time decay of the (a) case is slower.

References

1. Bedrici N., Vacossin B., Gatignol P., Generations d'ondes modales dans une structure multi-couche plane par l'impact d'un faisceau ultrasonore. *21e CFM*, Bordeaux, France (2013)
2. Clorennec D., Prada C., Royer D., Laser ultrasonic inspection of plates using zero-group velocity lamb modes. *IEEE Transactions on Ultrasonics, Ferroelectrics and Frequency Control* **57(5)**, 1125-1132 (2010).
3. Ducasse E. and Deschamps M., A nonstandard wave decomposition to ensure the convergence of Debye series for modeling wave propagation in an immersed anisotropic elastic plate. *Wave Motion*, **49(8)**, 745-764 (2012).
4. Kausel E. and Rosset J., Frequency Domain Analysis of Undamped Systems. *J. Eng. Mech.*, **118(4)**, 721734 (1992).
5. Lothe J. and Barnett D.M., On the existence of surface-wave solutions for anisotropic elastic half-spaces with free surface, *J. Appl. Phys.* **704(2)**: 428433 (1976).
6. Lowe M.J.S., Matrix Techniques for Modeling Ultrasonic Waves in Multilayered Media, *IEEE Transactions on Ultrasonics, Ferroelectrics and Frequency Control*, **42(4)**, 525-542 (1995).
7. Moreno P. and Ramirez A., Implementation of the numerical laplace transform: a review. *IEEE Trans Power Deliv*, **23(4)**: 25992609 (2008).
8. Nayfeh A.H., *Wave Propagation in Layered Anisotropic Media,* North-Holland, Amsterdam, 1995.
9. Phinney R. A., Theoretical calculation of the spectrum of first arrivals in layered elastic mediums. *J. Geophys. Res.*, **70(20)**, 51075123 (1965).
10. Shuvalov A.L., Poncelet O., Deschamps M., Analysis of the dispersion spectrum of fluid-loaded anisotropic plates: leaky-wave branches. *Journal of Sound and Vibration* **296(3)**, 494-517 (2006).
11. Stroh A.N., Steady state problems in anisotropic elasticity, *J. Math. Phys.* **41**: 77103 (1962).

The Uniform Theory of Diffraction (UTD) for elastic wave scattering from a half-plane

Audrey KAMTA DJAKOU, Michel DARMON and Catherine POTEL

Abstract

The scattering of elastic waves from an obstacle is of great interest in ultrasonic Non Destructive Evaluation (NDE). There exist two main scattering phenomena: specular reflection and diffraction. The Geometrical Theory of Diffraction (GTD) is a classical method used for modelling diffraction from canonical scattering objects. GTD is obtained using asymptotic approximation of the exact solution of a canonical elastic wave scattering problem. This approximation fails when the stationary phase point coalesces with a pole of the integrant i.e. for the observation direction of specular reflection. To relax this drawback, uniform GTD corrections have been developed in electromagnetism: among them, the Uniform Theory of Diffraction (UTD) based on the Pauli-Clemmow approximation. The edge diffracted field provided by UTD owns a discontinuity which compensates that of the geometrical field making the total field spatially uniform. UTD initially developed in electromagnetism has been established in elastodynamics to deal with the elastic wave scattering problem from a half-plane.

Keywords: elastodynamics, scattering, GTD, UTD, half-plane.

Audrey KAMTA DJAKOU
CEA-LIST, Department of Imaging & Simulation for Nondestructive Testing, CEA-Saclay, DIGITEO LABs, bât 565, 91191 Gif-sur-Yvette, France, e-mail: audrey.kamta-djakou@cea.fr

Michel DARMON
CEA-LIST, Department of Imaging & Simulation for Nondestructive Testing, CEA-Saclay, DIGITEO LABs, bât 565, 91191 Gif-sur-Yvette, France, e-mail: michel.darmon@cea.fr

Catherine POTEL
Laboratoire d'Acoustique de l'Université du Maine (LAUM), bât. IAM – UFR Sciences Avenue Olivier Messiaen, 72085 Le Mans Cedex 9, France, e-mail: catherine.potel@univ-lemans.fr

Wave propagation and localised modes in structures with diffuse cracks

Giorgio Carta, Michele Brun and Alexander B. Movchan

Abstract We investigate the propagation of elastic waves and localisation phenomena in diffusively damaged solids. First, we show that the eigenfrequencies of finite elongated solids with equispaced cracks and different lengths lie within the pass-bands of infinite periodic structures. Then, we present a reduced model, represented by a beam with elastic connections that simulate the cracked sections. The rotational and translational stiffnesses of the connections are determined by means of an asymptotic analysis. We show that the beam model is capable of describing accurately the dynamic response of the solid in a finite range of frequencies. We also point out that the limits of the pass-bands coincide with the eigenfrequencies of simple beams with appropriate boundary conditions.

1 Introduction

Cracks and defects in elastic solids generate stop-bands (also known as band-gaps), which are intervals of frequencies for which waves do not propagate. Band-gaps also arise when the structure contains discontinuities. Such discontinuities can be found, for instance, in bridges and pipelines where some cross-sections are reduced in depth for design purposes.

Static problems concerning elongated solids with transverse cracks, subjected to either longitudinal or transverse loads, are examined in [3] and [2], respectively.

Giorgio Carta
Department of Mechanical, Chemical and Materials Engineering, University of Cagliari, Via Marengo 2, 09123 Cagliari, Italy, e-mail: giorgio_carta@unica.it

Michele Brun
Department of Mechanical, Chemical and Materials Engineering, University of Cagliari, Via Marengo 2, 09123 Cagliari, Italy, e-mail: mbrun@unica.it

Alexander B. Movchan
Department of Mathematical Sciences, University of Liverpool, Liverpool, L69 3BX, UK, e-mail: abm@liverpool.ac.uk

In both works, a reduced asymptotic model is introduced to study the condition of decay for the boundary layer located in proximity of the crack.

Here, we apply the approach presented in [2] to dynamic problems. In particular, we analyse the propagation of elastic waves in long solids with equispaced deep cracks. In Sect. 2 we determine numerically the pass-bands and stop-bands of an infinite strip with periodic cracks; in addition, we compute the eigenfrequencies of finite strips of different length and we show that they fall inside the pass-bands of the infinite strip, provided that the associated eigenvectors are not localised. In Sect. 3 we employ the reduced beam model, which is proven to approximate well the dynamic behaviour of the strip; moreover, we observe that the limits of the pass-bands correspond to the eigenfrequencies of simple beams with proper boundary conditions. In Sect. 4 we indicate some practical applications relevant to this work.

2 Strip model

We consider time-harmonic transverse waves travelling in a two-dimensional elastic strip with equispaced deep cracks. First, we assume that the strip is of infinite length and consists of a sequence of elementary cells, as that drawn in Fig. 1. Here, h is the height of the strip, ϱ_ε is the depth of the cracked section, while l is both the distance between cracks and the length of the elementary cell.

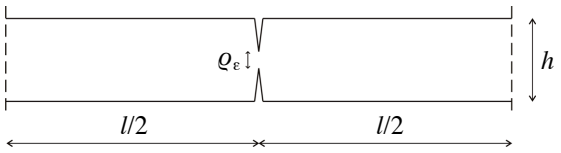

Figure 1: Elementary cell of a two-dimensional elastic strip with cracks located at regular intervals of length l.

The pass-bands of the infinite strip are obtained numerically by imposing Floquet-Bloch conditions at the ends of the elementary cell. The pass-bands are shown in grey colour on the right side of Fig. 2, where ω is the radian frequency.

Next, we consider finite strips made of different numbers of elementary cells. We calculate their eigenfrequencies and eigenmodes by performing finite element computations. The outcomes are reported in Fig. 2, where the eigenvalues corresponding to propagating modes are indicated by black dots, while those relative to localised modes are represented by black crosses. Examples of a propagation mode and of a localised mode are also illustrated in Fig. 2. We point out that all the eigenfrequencies associated to propagating modes lie within the pass-bands of the infinite strip.

3 Beam model

The two-dimensional strip can be studied analytically by using a lower-dimensional model, consisting of a beam with elastic junctions that represent the

cracked sections. The rotational and translational stiffnesses (per unit thickness) are derived from an asymptotic analysis [2] and are given by

$$\bar{K}_{\mathrm{b}} = \frac{K_{\mathrm{b}\varepsilon}}{s} = \frac{\pi E \rho^2}{4(5-2\nu)(1+\nu)} \tag{1}$$

and

$$\bar{K}_{\mathrm{s}} = \frac{K_{\mathrm{s}}}{s} = \frac{\pi E}{4(1-\nu^2)\log(h/\rho_{\varepsilon})}, \tag{2}$$

respectively. In the formulae above, s represents the thickness.

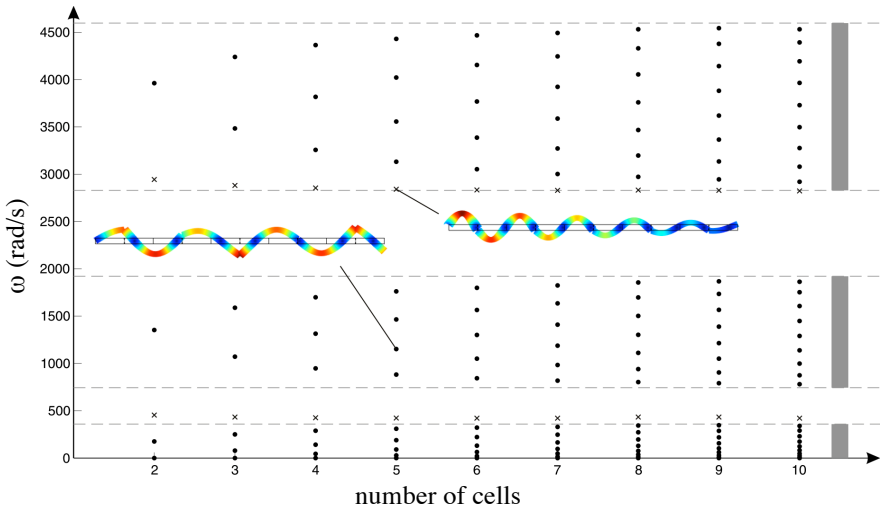

Figure 2: Eigenfrequencies of finite strips of different length associated to propagating modes (black dots) and localised modes (black crosses); pass-bands of the infinite strip (grey lines). These results are obtained by using the finite element software *Comsol Multiphysics (v. 4.3)*. (Young's modulus E = 200 GPa; Poisson's ratio ν = 0.3; mass density ϱ = 7800 kg/m^3; l = 2 m; h = 0.2 m; ϱ_{ε} = 0.04 m.)

We consider an infinite periodic beam. By applying Floquet-Bloch conditions, we obtain the dispersion curves shown in solid line in Fig. 3a. In this figure, k is the wavenumber and □ is a frequency parameter expressed by □ = ($\varrho A\omega^2 l^4/EJ$)^(1/4), where A and J are the area and the second moment of inertia of the beam cross-section. Fig. 3a shows that there is a very good correspondence between the lower three dispersion curves of the beam and the numerical results of the strip model, represented by dots. Furthermore, we notice that the limits of the

pass-bands coincide with the eigenfrequencies of the simple beams sketched in Fig. 3b.

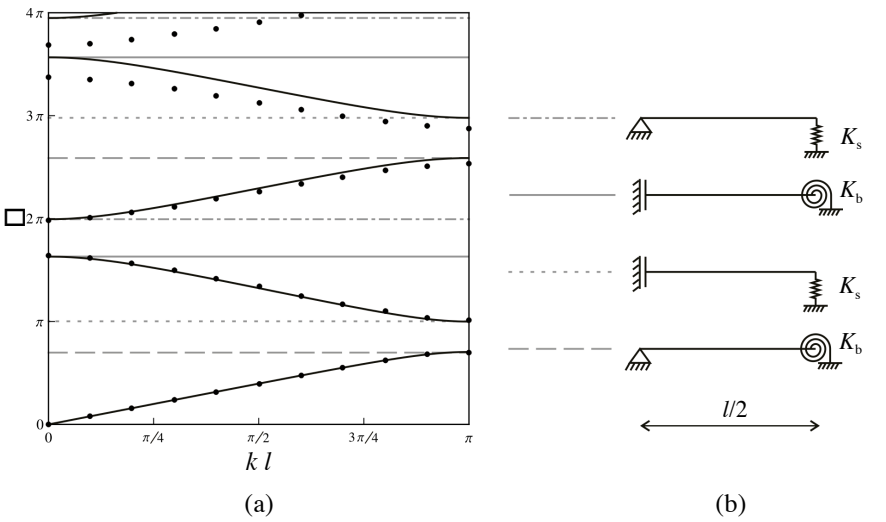

Figure 3: (a) Comparison between the dispersion curves of the infinite periodic beam (solid lines) and the numerical values relative to the infinite strip (dots) (E = 200 GPa; ν = 0.3; ϱ = 7800 kg/m^3; h = 0.2 m; ϱ_ε = 0.04 m); (b) simple beams with different boundary conditions, whose eigenfrequencies coincide with the limits of the pass-bands in (a).

4 Conclusions

The results of this work can be used to detect damages and defects in structures by means of non-destructive techniques. Moreover, they can be valuable to design structures with suitable sections of discontinuity that can filter waves of specific frequencies.

A more detailed discussion and thorough explanations of this work can be found in [1], where additional outcomes are also provided.

References

1. Carta G., Brun M., Movchan A.B. (2014), Dynamic response and localization in strongly damaged waveguides. *Proc. R. Soc. A*, in publication.
2. Gei M., Jones I.S., Movchan A.B. (2009), Junction conditions for cracked elastic thin solids under bending and shear. *Q. J. Mech. Appl. Math.* **62**, 481-493.
3. Zalipaev V.V., Movchan A.B., Jones I.S. (2007), Two-parameter asymptotic approximations in the analysis of a thin solid fixed on a small part of its boundary. *Q. J. Mech. Appl. Math.* **60**, 457-471.

The higher order integral equation method of homogenization: antiplane elasticity

Duncan Joyce, William J. Parnell and I. David Abrahams

Abstract Many techniques have been developed to attempt to model the effective macroscopic quasi-static properties of fibre reinforced composites (FRCs) from knowledge of their microstructure. One such example for periodic fibres is the method of asymptotic homogenization (MAH), which relies on computational evaluation of the cell problem. This work introduces an alternative, new method, based on an integral equation formulation of Naviers equations for low frequency antiplane shear (for ease of illustration) wave propagation. The asymptotic scheme developed enables new explicit analytical formulae, valid at arbitrary volume fraction, to be derived for the effective shear moduli in terms of parameters linked to specific physical phenomena (e.g. cross-sectional shape, phase properties, lattice type) thus providing greater insight than many extant methods. It appears that the scheme is simple to extend to higher dimensions in elasticity, the general transport problem and in some limits, the full elastodynamic problem to predict the onset of band-gaps.

1 Introduction and geometry of the problem

The integral equation method (IEM) was developed by Parnell and Abrahams in [1], where the antiplane (SH) wave problem for fibre reinforced composites (FRCs) was considered at leading order with respect to both the volume fraction of inclusions and the non-dimensional frequency ε. Advantageous features of this method include its validity for non-dilute regimes and the structure of the solution being such that individual terms account for specific physical features of the system such as the fibre

Duncan Joyce
University of Manchester e-mail: duncan.joyce@postgrad.manchester.ac.uk

William J. Parnell
University of Manchester e-mail: william.j.parnell@manchester.ac.uk

I. David Abrahams
University of Manchester e-mail: i.d.abrahams@manchester.ac.uk

cross-section and material properties. This is in contrast to the method of asymptotic homogenisation (MAH) where no such separation of physical phenomena occurs - instead the detail is hidden within the cell problem and the numerical schemes involved in solving it.

However, the method can be extended to obtain an asymptotic system in the volume fraction, and it is the aim of this work to show how that extension is made.

Consider identical isotropic fibres of an arbitrary shape embedded in an isotropic host material where the lattice geometry is restricted such that the effective medium appears at to be, at most, orthotropic on the macroscale (see Figure 1). Antiplane waves are then polarized in the x_3 direction, and propagate in the x_1, x_2 plane.

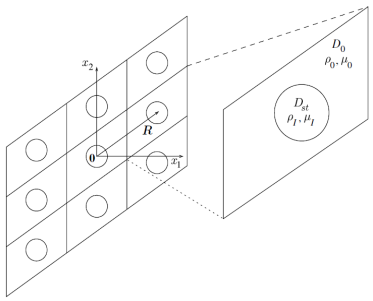

Fig. 1 An illustration of the cell geometry used, x_3 direction coming out of page, in line with fibre direction. μ denotes shear modulus, ρ density. I subscripts refer to the inclusions and 0 the host.

Under this regime, the volume fraction ϕ is defined as being per unit span in x_3 (the proportion of the composite that consists of fibres) and non-dimensional frequency is $\varepsilon = qk_0 \ll 1$, q being the characteristic length scale of the periodic cell and k_0 the wavenumber of the host.

2 Deriving the asymptotic system

Combining the scalar wave equation for dispalcement $w(\boldsymbol{x})$ in the x_3 direction and the governing equation for the Green's function $G(\boldsymbol{x})$, and applying continuity of displacement and normal stress on fibre-host interfaces, where $\boldsymbol{x} = (x_1, x_2)$, we find

$$w(\boldsymbol{x}) = -(1-m) \sum_{\substack{s,t=-\infty \\ s,t\in\mathbb{Z}}}^{\infty} \left(\int_{D_{st}} \nabla_y w(\boldsymbol{y}) \cdot \nabla_y G(\boldsymbol{y}-\boldsymbol{x}) d\boldsymbol{y} \right), \tag{1}$$

where $m = \mu_I/\mu_0$. Consider $\boldsymbol{x} \in D_{ab}$, so we are within the ($a$, b)th fibre with position vector $\boldsymbol{r}$. Differentiating (1) with respect to x_k ($k = 1,2$), Taylor expanding the Green's function about the (s, t)th fibre at $\boldsymbol{y} = \boldsymbol{p}$, then multiplying by $(x_1 - r_1)^{\delta}(x_2 - r_2)^{\xi}/(\delta!\xi!)$, integrating in the $\boldsymbol{x}$ plane over domain D_{ab} and Taylor expanding again about $\boldsymbol{x} = \boldsymbol{r}$ gives

$$W^{(k)}_{\delta\xi}(\boldsymbol{r}) = (1-m)\sum_{\boldsymbol{p}\neq\boldsymbol{r}}\left(\sum_{n=1}^{2}\sum_{i,j,\alpha,\beta=0}^{\infty} W^{(n)}_{ij}(\boldsymbol{p})C_{\delta\xi\alpha\beta}\partial_{p_n}\partial_{p_k}\partial^{i+\alpha}_{p_1}\partial^{j+\beta}_{p_2}G(\boldsymbol{p}-\boldsymbol{r})\right) - (1-m)\mathscr{A}^{(k)}_{\delta\xi}(\boldsymbol{r}), \tag{2}$$

where $C_{\delta\xi\alpha\beta} = O(\phi^{\delta+\xi+\alpha+\beta+2})$ is a fourth order tensor, $\mathscr{A}^{(k)}_{\delta\xi}(\boldsymbol{r}) = O(\phi^{\delta+\xi+2})$ is the shape factor and $W^{(k)}_{\delta\xi}(\boldsymbol{p}) = O(\phi^{\delta+\xi+2})$ is the displacement gradient tensor. $C_{\delta\xi\alpha\beta}$ and the shape factor are integrals within the (a,b)th fibre while $W^{(k)}_{\delta\xi}(\boldsymbol{p})$ is an integral over the (s,t)th fibre. The shape factor is related to the famous P tensor from the work of Eshelby [2].

By seeking wave type solutions which propagate in the x_1 direction of the form

$$W^{(k)}_{ij}(\boldsymbol{r}) = \hat{W}^{k}_{ij}\exp(i\gamma_1 r_1), \quad \mathscr{A}^{(k)}_{ij}(\boldsymbol{r}) = \hat{\mathscr{A}}^{(k)}_{ij}\exp(i\gamma_1 r_1), \tag{3}$$

where $\gamma_1^2 = 1/\mu_1^*$, we can then obtain an equation from (2) that is $O(1)$ with respect to ε. This equation will involve terms known as lattices sums, which depend upon the singular behaviour of $\partial^i_{u_1}\partial^j_{u_2}G(\boldsymbol{u})$ summed over all fibre locations.

By choosing different values of δ and ξ, we then obtain a system of equations involving the effective longitudinal shear modulus μ_1^*. It turns out that the shape factor can be written as a sum of displacement gradient moments, thus our system has the following general form

$$\begin{bmatrix} \mathscr{G}_{00}(\Gamma) & \mathscr{G}_{01} & \mathscr{G}_{02} & \cdots \\ \mathscr{G}_{10}(\Gamma) & \mathscr{G}_{11} & \cdots & \\ \vdots & \vdots & \ddots & \\ \mathscr{H}_{00} & \mathscr{H}_{01} & \cdots & \\ \mathscr{H}_{10} & \cdots & & \\ \vdots & \ddots & & \end{bmatrix} \begin{Bmatrix} \hat{W}^{(1)}_{00} \\ \hat{W}^{(1)}_{10} \\ \vdots \\ \hat{W}^{(2)}_{00} \\ \vdots \end{Bmatrix} = \mathbf{0}, \tag{4}$$

with all matrix coefficients depending on ϕ and the lattice sums and in particular the $\mathscr{G}_{i0}(\Gamma)$ coefficients depend on γ_1 through the function $\Gamma(\gamma_1) = 1/(1-\gamma_1^2)$. This segregation of the effective material properties within the system of equations is part of a rich structure discused in the introduction.

To take into account the contributions at different orders of the volume fraction, pose expansions of the form below and equate coefficients in ϕ.

$$\hat{W}^{(1)}_{\delta\xi} = u^0_{\delta\xi} + u^1_{\delta\xi}\phi + u^2_{\delta\xi}\phi^2 + \ldots \quad \hat{W}^{(2)}_{\delta\xi} = v^0_{\delta\xi} + v^1_{\delta\xi}\phi + v^2_{\delta\xi}\phi^2 + \ldots \tag{5}$$

$$\Gamma(\gamma_1) = \frac{a_{-1}}{\phi} + a_0 + a_1\phi + \ldots. \tag{6}$$

The coefficients in the expansion of $\Gamma(\gamma_1)$ are the most important to consider - after truncating to some order in ϕ, then we can obtain μ_1^* from this expansion and the relation $\gamma_1^2 = 1/\mu_1^*$. One could also obtain μ_2^* by simply rotating the material by $\pi/2$ and using the same wave type again.

With these expansions, (4) becomes similar to solving an eigenvalue problem, with the coefficients of $\hat{W}_{00}^{(1)}$ forming an eigenvector and μ_1^* the eigenvalue.

One may observe at what point to close the system in order to find $\Gamma(\gamma_1)$ to a particular order by observing the terms from the displacement gradient moments that appear at each order of ϕ in the first equation of the system.

3 Results

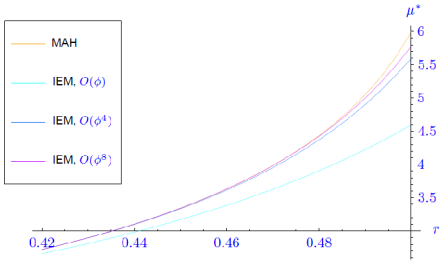

Fig. 2 Plot of effective longitudinal shear modulus versus radius of circular cylindrical fibres for square lattice, m =10, illustrating the convergence of the IEM to the MAH

One finds that for circular cylindrical fibres using a square lattice, μ_j is of the form

$$\mu_j = \frac{1+(S_j-1)\mathscr{M}\phi - \frac{\mathscr{M}^2 C_{4j}^2}{3\pi^2}\phi^4 - \frac{\mathscr{M}^2 C_{8j}^2}{\pi^6}\phi^8 + \ldots}{1+(S_j+1)\mathscr{M}\phi - \frac{\mathscr{M}^2 C_{4j}^2}{3\pi^2}\phi^4 - \frac{\mathscr{M}^2 C_{8j}^2}{\pi^6}\phi^8 + \ldots} \tag{7}$$

where $\mathscr{M} = (1-m)/(1+m)$ and S_j, C_{4j} and C_{8j} are terms that depend upon the second, fourth and eight order lattice sums respectively.

The above graph illustrates how the addition of the higher order terms in ϕ in this quotient help this result converge to previously obtained results obtained by the MAH.

Acknowledgements Joyce is grateful to Thales Underwater Systems Ltd and EPSRC for funding via a CASE studentship.

References

1. W.J. Parnell, I.D. Abrahams: A new integral equation approach to elastodynamic homogenization, *Proc. R. Soc. A*, V 464, 1461-1482, 2008.
2. J.D. Eshelby: The determination of the elastic field of an ellipsoidal inclusion, *Proc. R. Soc. A*, V 241, 376-396, 1957.

Spectral Methods: An alternative to root-finding routines for finding dispersion curves of anisotropic homogeneous media.

F. Hernando, M. Lowe and R. Craster.

Abstract Guided waves are now well established in NDE and there is ongoing research interest in guided waves for many applications so it is important to have reliable and accurate information about the waves and modes that can be propagated in a chosen waveguide structure. Valuable information is provided by the dispersion curves of different modes within various combinations of geometries and materials. However, the approach normally used to find them, root-finding methods, suffers from certain limitations concerning geometry, type of material, ill-conditioning of the matrix used to derive the dispersion relation, the well-known "large-*fd*" problem and incomplete solutions (missing modes).

An alternative to root-finding routines are Spectral Methods. These have been previously and successfully used in simple waveguide cases and show that all the above pitfalls and limitations are overcome. Moreover, the ease of coding and its great generality make this approach a better option in many cases where root-finding routines do not perform well or simply fail to solve the problem.

In this work we extend the Spectral Method to solve more complicated problems of interest for the industry and the field of NDE which, to our knowledge, have not yet been studied. All the cases presented deal with anisotropic homogeneous perfectly elastic materials in flat and cylindrical geometry. In the latter geometry, we

study both axial and annular propagation of Longitudinal and Torsional modes as well as a fairly detailed study of Flexural modes in anisotropic media. We also address the problem of multi-layered systems with both solid and fluid layers and the implementation of a spring model for imperfect boundary conditions between layers.

Flexural waves in structured elastic plates - trapped modes, transmission resonances and Elasto-Dynamically Inhibited Transmission (EDIT)

S G Haslinger

Abstract We consider the two models of scattering and Bloch waves for a structured system of periodic gratings in an infinite plate. The waves represent flexural deflections governed by the fourth-order biharmonic plate equation, placing the work in the relatively new field of platonics. By analogy with photonic and phononic crystals, the two-dimensional structures in thin elastic plates are known as platonic crystals. The emphasis is on the analysis of trapped modes and transmission resonances for different configurations of the grating stack and physical parameters of the flexural waves. In particular we analyse the phenomenon of Elasto-Dynamically Inhibited Transmission (EDIT), where a resonance in transmission is cut in two by a resonant minimum arising from destructive interference.

1 Introduction

We consider thin structured plates that contain an interaction region consisting of a finite number of periodic gratings, and our particular interest is in the localisation of flexural waves within the grating structure. Our model allows for the gratings to consist of cylindrical inclusions whose cross-sections are of arbitrary smooth shape or size. Here we concentrate on circular voids of finite radius with clamped boundaries, and the limiting case of the radius tending to zero, corresponding to a pinned point. We demonstrate that the grating stack supports sharp transmission resonances for low-frequency flexural vibrations. The resonances arise from the interaction with the plane wave, characterised by the angle of incidence θ_i and spectral parameter β.

We show one such configuration in Fig. 1, where the outer pair of the 3-grating system consists of clamped-edge voids with a finite radius a, whilst the central grating contains pinned points. The relative shift of the central grating ξ is crucial for supporting a filtering effect similar to electromagnetically induced transparency (EIT). We term this Elasto-Dynamically Inhibited Transmission (EDIT). This novel phenomenon for elasticity problems was first observed in [2]-[5]. It is characterised by a resonant peak in transmission being cut in two by a resonant dip with an extremely high quality factor.

Furthermore, the grating stack can be considered as a structured waveguide for trapped modes. For a simple case of a stack of rigid pins, a quasi-periodic Green's

S G Haslinger
University of Liverpool, Department of Mathematical Sciences, Mathematical Sciences Building, Peach Street, Liverpool L69 3BX, United Kingdom, e-mail: sgh@liv.ac.uk

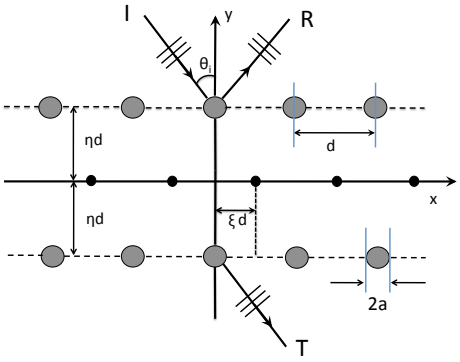

Fig. 1 Stack of gratings consisting of an outer pair of finite nonzero inclusions with radius a and period d, and a central grating of rigid pins. The relative grating separation between consecutive gratings is η, and the relative lateral shift of the central grating is ξ.

function is employed to derive the dispersion equation for Bloch waves in such a waveguide. A connection is established with the transmission problem by identifying parameters of the grating stack and of the incident wave, to generate a transmission resonance linked to a trapped Bloch wave within the structured waveguide.

2 Transmission resonances for gratings stacks

A plane wave representing flexural displacements is incident on a grating system that separates two half-planes in an infinite flexural plate (see Fig. 1). It is shown that a nearly 100 % transmission is achievable for a certain combination of parameters within a narrow frequency range.

2.1 Governing equations

Let the amplitude W be a solution of the scattering problem for the biharmonic operator (see [8]):

$$\Delta^2 W(\mathbf{x}) - \beta^4 W(\mathbf{x}) = 0, \tag{1}$$

where $\beta^2 = \omega\sqrt{\rho h/D}$. Within this expression, $D = Eh^3/(12(1-\nu^2))$ is the flexural rigidity of the plate, h denotes the plate thickness, E is the Young modulus and ν is the Poisson ratio. In addition, ρ is the mass density and ω is the angular frequency.

The field W satisfies the Bloch quasi-periodicity condition along the horizontal x-axis:

$$W(\mathbf{x} + md\mathbf{e}^{(1)}) = W(\mathbf{x})e^{i\alpha_0 md}, \tag{2}$$

where m is an integer, d is the period, and α_0 is the Bloch parameter $\alpha_0 = \beta \sin\theta_i$, where θ_i is the angle of incidence (see Fig. 1).

The boundary conditions on the circular boundaries of the inclusions are Dirichlet clamping conditions:

$$W\Big|_{r=a} = 0, \quad \frac{\partial W}{\partial r}\Big|_{r=a} = 0. \tag{3}$$

We initially consider the limit as $a \to 0$, corresponding to an array of rigid pins constraining the plate. The radius of the inclusions is important for the implementation of the method that we use to solve the problem, as outlined in the papers [2]-[8].

2.2 Method of solution

We consider the scattering of plane waves, either of the Helmholtz type W_H or of the modified Helmholtz type W_M, by a grating of inclusions of radius a. The flexural displacement W is expanded for $y > a$ and $y < -a$ in terms of sums of W_H and W_M. In order to connect these two types of expansions we introduce multipole expressions for W in the region $-a \le y \le a$. The multipole expansion for W_H involves cylindrical waves $J_n(\beta r)e^{in\theta}$ and $H_n^{(1)}(\beta r)e^{in\theta}$ with respective amplitudes A_n and E_n:

$$W_H(\mathbf{x}) = \sum_{n=-\infty}^{\infty} \{A_n J_n(\beta r) + E_n H_n^{(1)}(\beta r)\} e^{in\tau}. \tag{4}$$

The multipole expansion for W_M involves modified Bessel function terms $I_n(\beta r)e^{in\theta}$ and $K_n(\beta r)e^{in\theta}$ with respective amplitudes B_n and F_n:

$$W_M(\mathbf{x}) = \sum_{n=-\infty}^{\infty} \{B_n I_n(\beta r) + F_n K_n(\beta r)\} e^{in\tau}, \tag{5}$$

The amplitudes A_n, B_n, E_n, F_n are the multipole coefficients to be determined, and they are related by the boundary conditions (3).

The combination of the Rayleigh identity and the boundary conditions gives a system of linear equations, which is truncated and solved to evaluate a set of multipole coefficients. These in turn are used to evaluate plane wave amplitude coefficients for the fields above and below the grating. These are assembled into scattering matrices for reflection and transmission that completely characterise the grating's scattering action, and enable us to identify transmission resonances for a finite number of gratings.

Several results illustrating the transmission resonances have been published in the papers [2]-[5]. Here we illustrate the EDIT effect in Fig. 2 for a rigid-pin triplet. For more complicated structures, the required tuning of the grating stack as a scattering system is rather complex, but it becomes an easier task with the knowledge

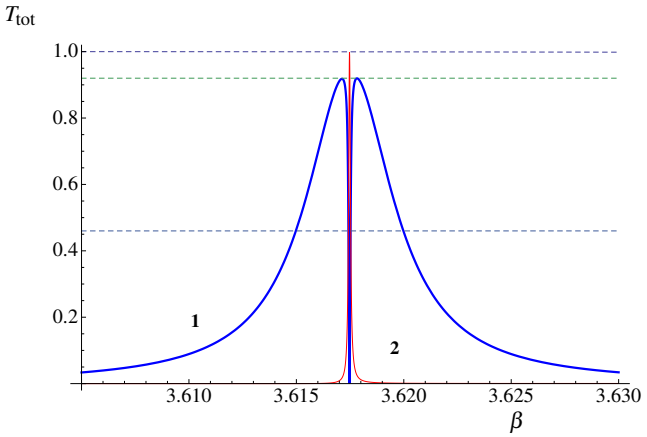

Fig. 2 EDIT effect for a triplet of rigid pin gratings with the central grating shifted by $\xi = 0.25200d$ for the angle of incidence $\theta_i = 30^\circ$. Total transmittance T_{tot} (curve **1**) as a function of β for the triplet. Curve **2** represents the total transmittance for the outer pair of gratings.

of dispersion properties of trapped flexural waves, attainable by treating the system as a waveguide.

3 Structured waveguide

We consider a waveguide consisting of a finite number of platonic gratings, which may be shifted relative to one another. We are primarily interested in a triplet because there are similarities with the scattering problem for which we identify extremely narrow frequency bands that support transmission resonances. The combination of the specific angle of incidence θ_i and its corresponding spectral parameter β means that each transmission peak is defined by a specific value of the Bloch parameter $\alpha_0 = \beta \sin\theta_i$.

3.1 Grating Green's function: plane wave form

We consider a single grating of rigid pins as a line of point forces with constant separation d. Therefore we use a quasi-periodic Green's function $G(x,y;\alpha_0,\beta)$ for the biharmonic operator [1], satisfying the equation

$$(\Delta^2 - \beta^4)G(x,y;\alpha_0,\beta) + \delta(y)\sum_{n=-\infty}^{\infty}\delta(x-nd)\exp\{i\alpha_0 nd\} = 0, \qquad (6)$$

where α_0 is the Bloch parameter and β is the spectral parameter associated with the frequency ω by $\beta^2 = \omega\sqrt{\rho h/D}$. The plane wave form form of the Green's function is

$$G(x,y;\alpha_0,\beta)=\frac{1}{2\beta^2}\left(\frac{1}{2id}\sum_{n=-\infty}^{\infty}\frac{1}{\chi_n}e^{i(\alpha_n x+\chi_n|y|)}+\frac{1}{2d}\sum_{n=-\infty}^{\infty}\frac{1}{\tau_n}e^{i\alpha_n x}e^{-\tau_n|y|}\right), \quad (7)$$

where

$$\alpha_n=\alpha_0+\frac{2\pi n}{d},\ \chi_n=\begin{cases}\sqrt{\beta^2-{\alpha_n}^2}\ , & {\alpha_n}^2\le\beta^2,\\ i\sqrt{{\alpha_n}^2-\beta^2}\ , & {\alpha_n}^2>\beta^2,\end{cases},\ \tau_n=\sqrt{\beta^2+\alpha_n^2}. \quad (8)$$

This quasi-periodic Green's function (7)-(8) is used to derive the dispersion equation for Bloch modes within the rigid-pin system. The modes take the form of complex resonances close to the real axis, and we classify them as even and odd modes. Dispersion curves for the modes are the trajectories along which the eigenvalues are zero (or more precisely, since we have complex entries, have a modulus close to zero). We are primarily interested in the two lowest branches of the waveguide's dispersion curves, illustrated in Fig. 3(a). The crossing of the two dispersion curves

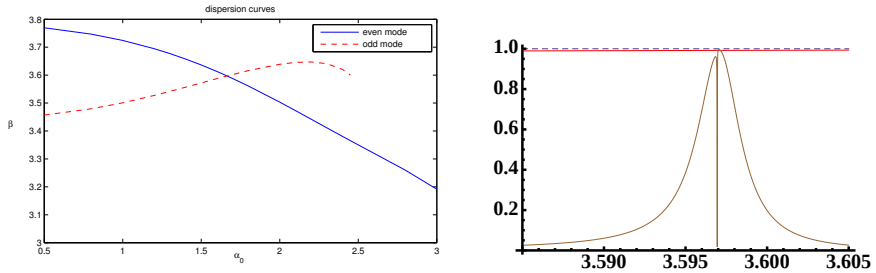

Fig. 3 (a) Dispersion diagram for a waveguide consisting of an unshifted triplet with the horizontal axis representing α_0 in the range $0.5 \le \alpha_0 \le 3$, and β on the vertical axis in the range $3 \le \beta \le 3.8$. The red curve represents the odd modes, and the blue curve, the even modes. (b) Normalised transmitted energy versus spectral parameter β for a triplet of rigid pins with angle of incidence $\theta_i = 0.481273$ and relative shift of the central grating $\xi = 0.012$.

is synonymous with a double eigenvalue case, and is of great interest. In Fig. 3(b), we consider the corresponding transmission resonance example for an angle of incidence in the vicinity of the intersection point, and we observe an EDIT-like effect, when we introduce a small non-zero shift of the central grating $\xi = 0.012$.

3.2 Tuning of the resonance transmission system

The two approaches outlined above present the grating stack as a periodic scatterer and as a waveguide. The results of analysis complement each other in a way that enables us to design a system possessing EDIT. The required tuning of the grating stack becomes a straightforward task with the knowledge of dispersion properties of trapped flexural waves. The intersection point of the dispersion curves corresponds to the frequency in the neighbourhood of EDIT. Further refinement is achieved by the choice of the shift parameter ξ.

References

1. D. V. Evans & R. Porter : Penetration of flexural waves through a periodically constrained thin elastic plate in *vacuo* and floating on water *J. Eng. Maths.* **58** 317-337, 2007.
2. S. G. Haslinger, N. V. Movchan, A. B. Movchan & R. C. McPhedran : Transmission, trapping and filtering of waves in periodically constrained elastic plates. *Proc. R. Soc. A* **468**, 76-93, 2012.
3. S. G. Haslinger, R. C. McPhedran, N. V. Movchan & A. B. Movchan : Localisation near defects and filtering of flexural waves in structured plates. *Int. J. Fract.* doi: 10.1007/s10704-013-9812-9, 2013.
4. S. G. Haslinger, R. C. McPhedran, N. V. Movchan & A. B. Movchan : Structured interfaces for flexural waves - trapped modes and transmission resonances. *Journal of Physics: Conference Series* **451** 012024, 2013.
5. S. G. Haslinger, A. B. Movchan, N. V. Movchan & R. C. McPhedran : Symmetry and resonant modes in platonic grating stacks. *Waves in Random and Complex Media* doi: 10.1080/17455030.2014.884733, 2014.
6. R. C. McPhedran, A. B. Movchan & N. V. Movchan : Platonic crystals: Bloch bands, neutrality and defects, *Mechanics of Materials* **41**, 356-363, 2009. (doi: 10.1016/j.mechmat.2009.01.005)
7. A. B. Movchan, N. V. Movchan & R. C. McPhedran : Bloch-Floquet bending waves in perforated thin plates *Proc. R. Soc. A* **463** 2505-2518, 2007.
8. N. V. Movchan, R. C. McPhedran, A. B. Movchan & C. G. Poulton : Wave scattering by platonic grating stacks. *Proc. R. Soc. A* **465**, 3383 - 3400, 2009. (doi: 10.1098/rspa.2009.0301)

Trapped modes in two dimensional waveguides

Cristina Sargent

Abstract Trapped modes are investigated in infinite, two-dimensional acoustic waveguides with Neumann or Dirichlet walls. A robust and general boundary element scheme for the governing Helmholtz equation is derived. Known results are confirmed and various new modes are identified, both inside and outside the continuous spectrum of propagating modes.
An effective method for distinguishing between genuine trapped modes and spurious eigenvalues induced by the truncation of the domain is presented. This method is also suitable for the detection and study of "nearly trapped modes" which are closely associated with pure trapped modes. These are of great importance in physical systems as they display many features of trapped modes which may be precluded by the imperfect geometry.

1 Introduction

Within the framework of classical wave theory, trapped modes are time-harmonic oscillations at some well-defined frequency, localised to the vicinity of a boundary or trapping structure in unbounded domains. The decay with distance away from the trapping feature is usually exponential although algebraic decay can also occur. Mathematically, a trapped mode corresponds to an eigenfunction of the relevant operator which does not radiate to the far field.

Over the past 60 years the study of trapped modes has intensified and diversified. Depending on the context, trapped modes are known as acoustic resonances, Rayleigh-Bloch waves, edge waves, array guided surface waves, sloshing modes, motion trapped modes and bound states.

Cristina Sargent
Imperial College, London, e-mail: cristina.sargent04@imperial.ac.uk

Jonathan Mestel
Imperial College, London e-mail: ma.dug@ic.ac.uk

Trapped modes are considered here in an acoustic context but a comparison can be made with the associated problems in water-waves and in quantum waveguides [1], [3], [5], [6]. Time-harmonic oscillations, with angular frequency ω, are considered so that the pressure fluctuation in the guide, ϕ, satisfies the Helmholtz equation $\nabla^2\phi + k^2\phi = 0$, subject to appropriate homogeneous boundary conditions. Here $\omega = kc$ where c is the wavespeed. A trapped mode (or acoustic resonance) corresponds to a solution ϕ with finite energy. The positive value of the wavenumber k for which the solution exists is referred to as the trapped mode frequency.

Trapped modes can be classified as embedded or non-embedded, depending on whether their frequency is respectively above or below the first waveguide cut-off. This distinction is important as it determines the stability of the mode. The non-embedded modes are stable in the sense that if a geometric parameter is modified, the mode persists up to some limit, with only a slight variation of the frequency. In contrast, embedded modes may only exist for a specific combination of the geometric parameters and may be destroyed by an infinitesimal perturbation of the configuration. This means that for many configurations, embedded modes may not exist at all, or there may be only a few discrete geometric parameter values which support such a mode. From a computational perspective the distinction is important because embedded trapped modes require higher detection accuracy than non-embedded modes as an eigenvalue in the continuous spectrum disappears under small perturbations.

There is an immense amount of literature on trapped mode problems, covering analytical, numerical and physical aspects to which it is hard to do justice. We mention here a few results and relevant notions, with our list of references being far from exhaustive.

For a specified geometry, uniqueness of the solution to a forcing problem at a particular frequency is equivalent to the non-existence of a trapped mode at that frequency. In 1950 John [7] established uniqueness for a particular class of single, surface-piercing bodies which have the property that any vertical line emanating from the free surface does not intersect the body. Ursell (1950) proved uniqueness for a circular cylinder submerged in fluid of infinite depth [16]. Since then many other partial results have been obtained (see, for example, Simon and Ursell (1984) [15]) but a general proof of uniqueness for all bodies at all frequencies was not found. The reason for the absence of a general uniqueness proof became clear when M. McIver (1996), constructed an explicit example of two surface-piercing bodies for which the potential is non-unique at a specific frequency [11]. Detailed reviews of the literature are provided by Linton & McIver [10] and Kuznetsov *et al.* [9].

Ursell (1951) established the correspondence between the finite energy of a trapped mode and the type of eigenvalue which gives rise to it [17]. If a fluid is bounded by fixed surfaces and by a free surface of infinite extent, the modes of vibration with infinite energy form a continuous spectrum. A trapped mode has finite total energy and corresponds to a discrete eigenvalue embedded in the continuous spectrum. In a subsequent study, Jones (1953) established that semi-infinite domains which are cylindrical at infinity have a continuous spectrum with a discrete embedded spectrum [8]. Jones' work established the Helmholtz equation, with suitable

boundary conditions, as a rich mathematical area for the study of trapped modes which we continue in this work.

Following these initial results establishing their existence, trapped modes were discovered in many contexts, from large physical structures supported by arrays of standing columns to quantum waveguides and nanowire inclusions in metamaterials [14]. Given their wide applicability, from non-destructive testing to, very recently, enhancement of evanescent modes in the nearfield of a 'perfect lens' [12], [13], a systematic and efficient numerical method of detection of trapped modes is required.

Here we present an approach based on the boundary element method (BEM) which we use to reveal the rich structure of trapped modes in two-dimensional waveguides. The scheme was designed to be flexible, computationally efficient and accurate. To ensure the validity of results, the technique was initially applied to the above cases where solutions are either already known or can be calculated analytically. Subsequently it was applied to the study of geometries with one or two discs of identical or different radius, at varying distances from each other. Another class of geometries explored includes waveguides with rectangular, smooth, triangular symmetric and irregular wall cavities and also combinations of cavities and discs. All cases were studied with various combinations of Neumann or Dirichlet boundary conditions.

The method obtains approximate numerical solutions and accurately detects exponentially decaying modes in infinite guides by carrying out computations over a finite portion of the boundary. Estimates of the radiation loss associated with each mode are used to remove the spurious solutions introduced by the truncation of the domain. This novel approach allows the study of general configurations for higher frequency ranges where the presence of propagating modes make other computational methods ineffective. Other procedures have been employed for the numerical detection of trapped modes, including the finite element method combined with the perfectly matched layer (PML), as used by Duan *et al.* [2] for similar problems. PMLs are advantageous in some problems, but we consider our BEM approach more appropriate for trapped mode detection.

Trapped modes for two sound-hard discs, either of equal or different radius, are examined for both Neumann and Dirichlet cases. For non-embedded modes we confirm the findings of Evans & Porter [4] and study the number and type of modes, frequencies and dependence on geometry in detail. The non-embedded trapped mode frequencies for one disc on the centreline, which are in agreement with those of Callan *et al.* [1], were part of a suite of tests carried out to verify the method's precision and validity. Details of additional modes which appear for larger discs are found and provide a complete picture of trapped modes for this geometry and frequency range. Up to four modes can be found for a Neumann guide with either one or both discs such that $0.8 \leq a/d \leq 1$, their appearance being determined by the distance between obstacles. Similar results were obtained for the Dirichlet case with two identical sound-hard discs on the centreline, up to the third cut-off frequency of the guide. The problem of two two-sound hard discs of different radius on the centreline of a soft guide was also investigated. Trapped modes for two-dimensional asymmetric Dirichlet and Neumann waveguides with cavities of rectangular, trian-

gular or smooth shape and with a circular obstacle added to the centreline, aligned with the cavity or removed from the centre are also investigated. The results suggest that at least one symmetry line is an essential condition for the formation of trapped mode type resonances. The addition of a new geometric parameter to a problem which has one embedded trapped mode solution for a specific discrete geometry, leads to the appearance of a continuous set of trapped modes.

Finally, the related and important topic of nearly trapped modes, which are resonances with very small radiation, is discussed. Nearly trapped modes appear consistently throughout the numerical investigations. It was found that in general, the specific set of parameters which corresponds to an embedded trapped mode is a discrete point in a small continuous band of parameters which support nearly trapped modes. As a result, many geometries closely approximating that required for a trapped mode, will give rise to a nearly trapped mode, which in a physical system might be indistinguishable from an exact resonant mode.

References

1. M.A Callan, C.M. Linton, and D.V Evans. Trapped modes in two-dimensional waveguides. *J. Fluid Mech*, 229:51–64, 1991.
2. Y. Duan, W. Koch, C.M. Linton, and M. McIver. Complex resonances and trapped modes in ducted domains. *J. Fluid Mech.*, 571:119–147, 2007.
3. C.M. Linton D.V. Evans and F. Ursell. Trapped mode frequencies embedded in the continuous spectrum. *Q.J. Mech. Appl. Math*, 46(2):253–274, 1993.
4. D.V. Evans and R.Porter. Trapped modes about multiple cylinders in a channel. *J. Fluid Mech.*, 339:331–356, 1997.
5. D.V. Evans and R.Porter. Trapping and near-trapping by arrays of cylinders in waves. *Journal of Engineering Mathematics*, 35:149–179, 1999.
6. P. Exner and P. Seba. Bound states in curved quantum waveguides. *J. Math. Phys*, 30(11):25742580, 1989.
7. F. John. On the motion of floating bodies. *Commun. Pure Appl. Math*, 3:45–10, 1950.
8. D.S. Jones. The eigenvalues of $\nabla^2 u + \lambda u = 0$ when the boundary conditions are given in semi-infinite domains. *Proc. Camb. Phil. Soc*, 49:668–684, 1953.
9. N. Kuznetsov, V. Maz'ya, and B. Vainberg. *Linear Water Waves*. Cambridge University Press, Cambridge, 2002.
10. C.M. Linton and P. McIver. Embedded trapped modes in water waves and acoustics. *Wave Motion*, 45:16–29, 2007.
11. M. McIver. An example of non-uniqueness in the two-dimensional linear water wave problem. *J. Fluid Mechanics*, 315:257–266, 1996.
12. J. B. Pendry. Negative refraction makes a perfect lens. *Phys Rev Lett.*, 85:3966–3969, 2000.
13. J. B. Pendry. Negative refraction. *Contemporary Physics*, 45:191–202, 2004.
14. V.A Podolskiy, A.K. Sarychev, and V.M. Shalaev. Plasmon modes and negative refraction in metal nanowire composites. *Optics Express*, 11(7):735–745, 2003.
15. M. J. Simon and F. Ursell. Uniqueness in linearized two-dimensional water-wave problems. *J. Fluid Mech.*, 148:137–154, 1984.
16. F. Ursell. Surface waves on deep water in the presence of a submerged cylinder. *Proc. Camb. Phil. Soc*, 46:153–158, 1950.
17. F. Ursell. Trapping modes in the theory of surface waves. *Proc. Camb. Phil. Soc*, 47:347–358, 1951.

Development of ultrasonic propagation simulation for acoustic thermometry in liquid sodium

Nicolas MASSACRET, Joseph MOYSAN

Abstract: In the frame of research on Sodium cooled Fast nuclear Reactor (SFR), CEA aims to develop an innovative instrumentation, specific to these reactors. The present work relates to the measurement of the sodium temperature at the outlet of the assemblies of the reactor's core by an ultrasonic method. This instrumentation involves the propagation of ultrasonic waves in liquid sodium, thermally inhomogeneous and turbulent. Environment causes deviations of the acoustic beam that must be understood to predict and quantify to consider ultrasound as a measure means in a core of SFR reactor.

To determine the magnitude of these influences, a code named AcRaLiS (Acoustic Ray in Liquid Sodium) has been implemented. This implementation has been performed to allow rapid simulations of the wave propagation at several megahertz in this particular environment. This code provides ultrasounds deviations and changes in beam intensity.

Two experiments were designed and conducted to verify the code. The first, named UPSilon innovates by replacing sodium by silicone oil in order to have a stable thermal inhomogeneity during the experiment. It allows to determine the validity of the code AcRaLiS with thermal inhomogeneities. The second, called IKHAR allows to study the influence of water turbulence on the propagation of waves, using the Kelvin-Helmholtz instabilities.

Nicolas MASSACRET
Aix-Marseille Université, LMA UPR 7051 CNRS, site LCND, 13625 Aix-en-Provence, France : nicolas.massacret@gmail.com
Joseph MOYSAN
Aix-Marseille Université, LMA UPR 7051 CNRS, site LCND, 13625 Aix-en-Provence, France : joseph.moysan@univ-amu.fr

1 Acoustic thermometry in liquid sodium

Sodium-cooled fast reactors have been chosen by France as the reference option in the framework of the Generation IV international forum. For this kind of reactor, it is necessary to develop a specific instrumentation, compatible with sodium used as coolant, and to achieve the objectives of the Generation IV, particularly in terms of reliability.

Concerning the measurement of the sodium temperature at the outlet of the subassemblies of the reactor's core, an instrumentation being developed by the CEA is to send an acoustic wave reflect on one or more heads of subassemblies. The measurement of time of flight of ultrasound between each of the two edges of the head is used to determine the speed of ultrasound in the liquid sodium. This speed is directly related to the sodium temperature, which allows to measure this parameter.

This method has several advantages in terms of accuracy, speed and reduces the instrumentation volume above the core. However, it involves the propagation of ultrasound between the transducer and the subassembly head: a medium where the sodium temperature and speed fields can cause ultrasonic deviations. Such deviations must be quantified to determine their effect on the temperature measurement.

2 Acoustic ray simulations

In order to solve this problematic, a code has been implemented to simulate the propagation of ultrasound. This code named AcRaLiS (Acoustic Ray in Liquid Sodium) is based on the acoustic ray theory and allows to trace the path of ultrasounds in an environment where the fields of temperatures and speeds are inhomogeneous. In a second part of the code the Gaussian beam summation method is used to determine the energy profile of the wavefront. It will be specified in this section the model and the method of implementation used in this code.

3 Experimental verifications

Two experimental benches were created to verify the results of AcRaLiS code.

The first named UPSilon (Ultrasonic Path in Silicone Oil) is used to measure ultrasonic deviations in inhomogeneous temperatures fields. Experiments were performed in silicone oil, whose high viscosity limits the convection phenomena. Several experimental results are presented in this section.

The second device named IKHAR (Kelvin-Helmholtz Instabilities of Acoustics for Researches), is used to measure ultrasonic deviations in inhomogeneous speeds fields. This device implements eddies, named Kelvin-Helmholtz instabilities, in a water flow. Regular frequency and well-known speed field of these instabilities allows to know precisely the environment in which propagates ultrasound. As the experiments are still in progress, only the principle of operation of the device will be presented in this section.

4 Numerical simulations for acoustic thermometry in reactor

The use of this numerical tool for acoustic thermometry in reactor allows to determine how geometric features of the heart will cause acoustic disturbances. This code also allows to quickly determine the effectiveness of different measurement configurations. Several simulation results are presented in this section.

Tunable elastodynamic band-gaps

Ellis Barnwell, William J. Parnell and I. David Abrahams

Abstract We discuss tuning the antiplane elastic material properties of a 2D periodic elastic (phononic) material by applying a nonlinear prestress. The material in question is a series of annular cylinders embedded in a uniform host material. Wave propagation in the pre-stressed configuration is modelled by using the theory of small-on-large. Once the incremental wave equation is determined, the plane wave expansion method is used to find the band diagram for a neo-Hookean material. It is shown that stop bands can be switched on and off by application of the prestress.

1 Introduction

Complex metamaterials are at the heart of modern day engineering and technology. A vast number of such materials possess an intricate microstructure that supplies macroscopic behaviour which is non existent in naturally occurring materials. It is desirable to create macroscopic properties that can be tuned in real time. Predicting how the microstructure affects the macroscopic properties on a static and dynamic level is pivotal to the design and tuning of these materials. In this paper we will illustrate that the dynamic properties of a phononic material can be tuned by employing nonlinear elastomeric materials.

In the field of elastodynamics, there has been significant recent interest in the tunability of periodic structures. For example, Goffaux and Vigneron [1] introduce tunability of a composite by rotating square cylinders inside a fluid. Early work on

Ellis Barnwell
University of Manchester, Oxford Rd, M13 9PL e-mail: Ellis.Barnwell@gmail.com

William J. Parnell
University of Manchester, Oxford Rd, M13 9PL e-mail: william.parnell@manchester.ac.uk

I. David Abrahams
University of Manchester, Oxford Rd, M13 9PL e-mail: david.abrahams@manchester.ac.uk

the effect of a finite deformation on the incremental wave propagation through a material was carried out in 1D by Rogerson and Sandiford [4] and expanded upon later by Parnell [2]. In the latter of these papers, the stop and pass band structure is investigated for a range of prestress parameters. By making use of simulations, Wang and Bertoldi [6] have investigated the tunability of 3D structures. This paper makes use of the finite element method to find the band gap structure.

In this paper we will discuss the propagation of antiplane elastic waves through a prestressed hyperelastic material. The material in question is two dimensional and is made up of a periodic array of annular cylinders embedded in a homogeneous elastic host. Each cylinder may be inflated by changing its internal pressure. The theory of small on-large is used to determine the equation governing incremental antiplane waves propagating through the prestressed medium. Subsequently the plane wave expansion method [5] is used to efficiently determine the band structure. The effect of the prestress on this structure is investigated and it is shown that stop bands can be switched on and off by inflating or deflating the cavities.

2 Cavity inflation

The basic phononic crystal structure will be a periodic array of hyperelastic annular cylinders embedded in a homogenous host material. We restrict ourselves to the propagation of out of plane elastic shear waves that are polarised along the axes of the cylinders. We consider a prestress that has been induced by the inflation of the cylinders along with an axial stretch. The host material outside of the cylinder remains unstressed. The configuration is illustrated in figure 1 where the prestressed annular region is located in $r_0 < r < r_1$. The outer radius $R_1 = r_1$ remains unchanged during the deformation.

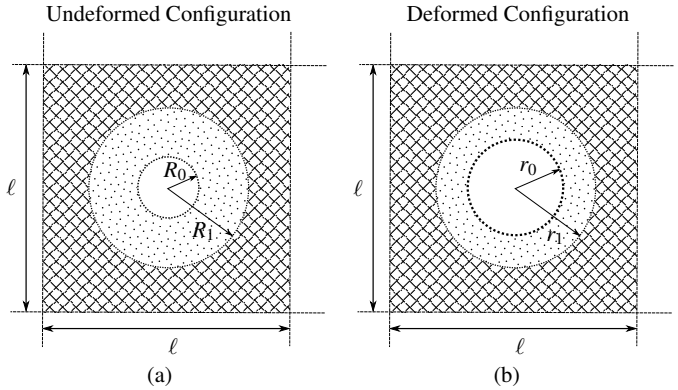

Fig. 1 Illustration of the unit cell for (a) the undeformed configuration and (b) the deformed configuration. The cylindrical annulus is embedded in an unstressed, homogeneous medium with the hatched pattern.

Working in cylindrical polar coordinates r, θ, z and assuming that the pre-stress induces only radially varying deformation, the incremental equation governing the time-harmonic (with frequency ω) antiplane wave amplitudes $w(\mathbf{x}) = w(x,y)$ in the prestressed cylinder has been derived in [3] and is given by

$$\frac{1}{r}\frac{\partial}{\partial r}\left(r\mu_r(r)\frac{\partial w}{\partial r}\right) + \frac{1}{r^2}\frac{\partial}{\partial \theta}\left(\mu_\theta(r)\frac{\partial w}{\partial \theta}\right) + \rho(r)\omega^2 w = 0 \tag{1}$$

where $\mu_r(r)$ and $\mu_\theta(r)$ are the incremental shear moduli and ρ is the mass density. For an incompressible neo-Hookean material the incremental moduli in the prestressed region are given by

$$\mu_r(r) = \frac{\mu_1^2}{\mu_\theta(r)L^2} = \frac{\mu_1}{L}\left(\frac{r^2+M}{r^2}\right) \tag{2}$$

where μ_1 is the shear modulus in the annulus and L is the stretch along the axis. The parameter M characterises the deformation and is given by $M = R_1^2(L^{-1}-1)$. The mass density is unchanged by the deformation.

3 Plane wave expansion

Since the structure of the material is periodic in Cartesian coordinates, in order to apply the plane wave expansion (PWE) method, convert equation (1) into Cartesians x, y, z, i.e.

$$\begin{aligned}
&\left(x^2\mu_r + y^2\mu_\theta\right)\frac{\partial^2 w}{\partial x^2} + \left(y^2\mu_r + x^2\mu_\theta\right)\frac{\partial^2 w}{\partial y^2} + \left(2xy\,\mu_r - 2xy\,\mu_\theta\right)\frac{\partial^2 w}{\partial x \partial y} \\
&+ \left(x^2\frac{\partial \mu_r}{\partial x} + x\mu_r + xy\frac{\partial \mu_r}{\partial y} - x\mu_\theta\right)\frac{\partial w}{\partial x} + \left(y^2\frac{\partial \mu_r}{\partial y} + y\mu_r + xy\frac{\partial \mu_r}{\partial x} - y\mu_\theta\right)\frac{\partial w}{\partial y} \\
&+ (x^2+y^2)\rho\,\omega^2 w = 0
\end{aligned} \tag{3}$$

The PWE is then employed, expanding each of the coefficients of the derivatives as Fourier series. We also assume that $w(x,y)$ has a Bloch-Floquet form, where the periodic part is also given as a Fourier series. By doing this, we obtain a generalised eigenvalue problem given by

$$\begin{aligned}
\sum_{\mathbf{G}}\Big[&a_{\mathbf{G}'-\mathbf{G}}(K_x+G_x)^2 + b_{\mathbf{G}'-\mathbf{G}}(K_y+G_y)^2 + c_{\mathbf{G}'-\mathbf{G}}(K_x+G_x)(K_y+G_y) \\
&- id_{\mathbf{G}'-\mathbf{G}}(K_x+G_x) - ie_{\mathbf{G}'-\mathbf{G}}(K_y+G_y) - \rho_{\mathbf{G}'-\mathbf{G}}\,\omega^2\Big] w_{\mathbf{G}} = 0.
\end{aligned} \tag{4}$$

To find the band structure, we impose a Bloch wavenumber, K_x, K_y, and determine the associated eigenvalues, ω, scanning around the edge of the Brillouin zone.

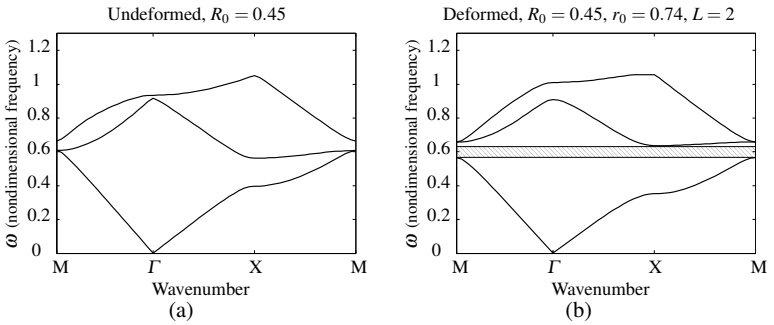

Fig. 2 The first three modes for an undeformed cylinder of initial radius of $R_0 = 0.45$. Figure (b) shows the band diagram of the deformed configuration corresponding to an axial stretch of $L = 2$ and deformed cavity radius $r_0 = 0.74$. A stop band is shown by the shaded region.

In figure 2 we illustrate how a stop band can be switched on by applying an internal pressure (or equivalently, applying an axial stretch) and increasing the inner radius. The first three modes are plotted for an initial inner radius of $R_0 = 0.45$ in the undeformed configuration and the prestressed configuration corresponding to $L = 2$.

4 Conclusion

In this paper we have utilised the plane wave expansion method to determine the band structure associated with antiplane wave propagation in a prestressed 2D nonlinear composite. The incremental wave equation was found using the small-on-large technique for a finite deformation of the hyperelastic medium. This method has allowed us to efficiently find the band gap structure and it has been shown that it is possible to switch on and switch off stop bands by employing a prestress.

References

1. C Goffaux and J P Vigneron. Theoretical study of a tunable phononic band gap system. *Phsyics revew B*, 2001.
2. W J Parnell. Effective wave propagation in a prestressed nonlinear elastic composite bar. *Journal of applied maths*, 2007.
3. W J Parnell. Nonlinear pre-stress for cloaking from antiplane elastic waves. *Proceedings of the royal society A: mathematica, physical and engineering science*, 2012.
4. G A Rogerson and K J Sandiford. The effect of finite primary deformations on harmonic waves in layered elastic media. *International journal of solids and structures*, 2000.
5. Kushwaha M S, Halevi P, and Martinez G. Theory of acoustic band structure of periodic elastic composites. *Physical review B*, 1994.
6. L Wang and K Bertoldi. Mechanically tunable phononic band gaps in three-dimensional periodic elastomer structures. *International journal of solids and structures*, 2012.

Cloaking of Finite Inclusions for Flexural Waves in Thin Kirchhoff Plates Using Active Control Sources

J. O'Neill, Ö. Selsil, R.C. McPhedran, A.B. Movchan, N.V. Movchan

Abstract We present a new analytical method to create an active cloak for an inclusion in a thin Kirchhoff plate. In order to cloak the inclusion, we place control sources outside of the inclusion and choose their intensities to eliminate propagating components of the scattered wave, thus reconstructing the incident wave.

1 Introduction

Since the beginning of 2007 there has been a vast number of publications on cloaking; more than 200 articles mention cloaking in their titles, with articles in the thousands having been stimulated by some ground-breaking papers by Leonhardt [1] and Pendry *et al.* [2]. We note that the initial subject of cloaking visible light has been broadened, with cloaking techniques being developed for a whole range of wave types, such as microwaves, surface plasmons, water waves, acoustic and elastodynamic waves, seismic waves and flexural waves.

We distinguish three broad classes of cloaking systems. The initial systems of Leonhardt and Pendry achieved scattering reduction by surrounding the object by a well-designed coating, which we term interior cloaking. Another method achieves scattering reduction in a region outside the system: external cloaking (see Nicorovici *et al.* [3]). The topic of our interest here is that of active cloaking, which relies on locating a number of active sources outside the object. For early work on this method we refer to Miller [4] and subsequently to Guevara Vasquez *et al.* [5] and

J. O'Neill, Ö. Selsil, A. B. Movchan, N. V. Movchan
Department of Mathematical Sciences, University of Liverpool, Liverpool L69 7ZL, UK.
e-mail: J.O'Neill@liv.ac.uk, oselsil@liv.ac.uk, abm@liv.ac.uk, nvm@liv.ac.uk

R. C. McPhedran
Department of Mathematical Sciences, University of Liverpool, Liverpool L69 7ZL, UK and
CUDOS ARC Centre of Excellence, School of Physics, University of Sydney, Sydney, Australia.
e-mail: ross@physics.usyd.edu.au

Zheng *et al.* [6]. Norris *et al.* [7] developed a method to evaluate the amplitudes of active source terms that made direct use of the results of Guevara Vasquez *et al.* [8], which was later extended to elastodynamic cloaking (Norris *et al.* (2014) [9]). Transformation elastodynamics, as well as active exterior acoustic cloaking, are the topics presented in great detail in the comprehensive article by Guevara Vasquez *et al.* [10]. Our work here was stimulated by the work of the Milton group (see for example Guevara Vasquez *et al.* [11], [12]).

We build our study on previous investigations of the interaction of flexural waves with structured systems of scatterers (Norris & Vemula [13], Evans & Porter [14], Movchan *et al.* [15], McPhedran *et al.* [16] and Movchan *et al.* [17]).

2 Scattering of Flexural Waves by an Inclusion in the Presence of Control Sources Present - Reduction of the Shadow Region

We consider propagation of flexural waves in a thin Kirchhoff plate containing an arbitrarily shaped inclusion with a smooth boundary. Our ultimate aim is to successfully cloak this inclusion in the presence of an incident wave, using active control sources (point sources) located in the exterior of the inclusion. We then choose the source intensities to eliminate propagating components of the scattered wave, thus reconstructing the incident wave.

Initially we study the problem of a clamped (rigid) inclusion, that is, we pose zero displacement and zero normal derivative of the displacement on the boundary of the inclusion. We emphasise that our proposed method is suitable for an arbitrarily shaped inclusion. We then discuss, in detail, the canonical case of a circular cylinder which allows for an analytical solution.

We exemplify our results in a number of illustrative cases: (a) The results for the problem for which the incident wave is represented by the Greens function corresponding to a remote point source is shown in Fig. 1. The inclusion is assumed to be of circular shape in this particular case. (b) The results for the problem for which the incident wave is a plane wave is shown in Fig. 2. The inclusion is assumed to be of arbitrary shape with a smooth boundary in this particular case.

For all the details we refer the reader to O'Neill *et al.* [18].

If time permits, we will also discuss the case when the cylindrical inclusion is coated with another material, whose properties differ from the inclusion itself and its surrounding matrix. We will surround the coating with active control sources as described above.

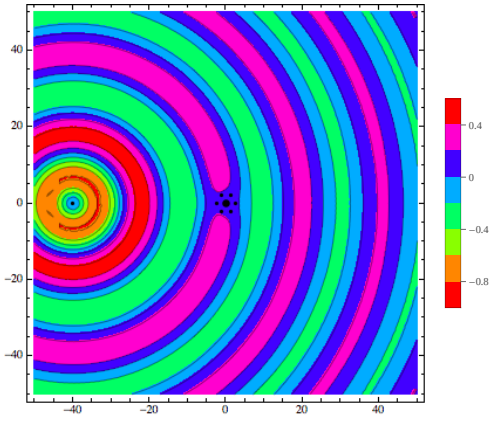

Fig. 1: The large black dot depicts the position of the cylinder, the small dot on the far left the position of the point source emitting the incident wave and the six small dots around the cylinder the control sources, respectively. Effectively perfect cloaking achieved by the use of six control sources.

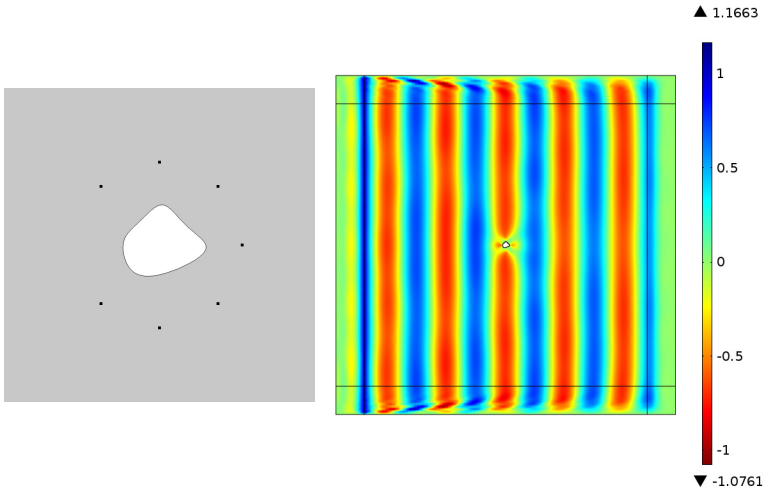

Fig. 2: Left: Enlarged view of the scatterer and the locations of the control sources. Right: Effectively perfect cloaking achieved by the use of seven control sources.

3 Conclusion

We have obtained an effectively perfect active cloak of an inclusion for flexural waves in an infinite thin plate, suppressing the shadow region behind the inclusion.

The method we will present is generic and extends to other types of boundary conditions as well as arrays of defects rather than a single scatterer.

Acknowledgements J. O'Neill would like to greatly acknowledge the support from the EPSRC through the grant EP/L50518/1. R.C. McPhedran and N.V. Movchan acknowledge the financial support of the European Community's Seven Framework Programme under the contract number PIAPP-GA-284544-PARM-2. R.C. McPhedran also acknowledges support from the Australian Research Council through its Discovery Grants Scheme. We would like to also thank Dr. D.J. Colquitt for his invaluable help with COMSOL.

References

1. Leonhardt, U. 2006. Optical conformal mapping. *Science*, **312**, 1777-1780.
2. Pendry, J. B., Schurig, D. & Smith, D. R. 2006. Controlling Electromagnetic Fields. *Science*, **312**, 1780-1782.
3. Nicorovici, N-A.P., Milton, G.W., McPhedran, R.C. & Botten, L.C. 2007. Quasistatic cloaking of two-dimensional polarizable discrete systems by anomalous resonance. *Opt. Express*, **15**, 6314-6323.
4. Miller, D.A.B. 2006. On perfect cloaking. *Opt. Express*, **14**, 12457-12466.
5. Guevara Vasquez, F., Milton, G.W. & Onofrei, D. 2009. Active exterior cloaking for the 2D Laplace and Helmholtz equations. *Phys. Rev. Lett.*, **103**, 073901.
6. Zheng, H.H., Xiao, J.J., Lai, Y. & Chan, C.T. 2010. Exterior optical cloaking and illusions by using active sources: A boundary element perspective. *Phys, Rev. B*, **81**, 195116.
7. Norris, A.N., Amirkulova, F.A. & Parnell, W.J. 2012. Source amplitudes for active exterior cloaking. *Inverse Problems*, **28**, 105002.
8. Guevara Vasquez, F., Milton, G.W. & Onofrei, D. 2011. Exterior cloaking with active sources in two dimensional acoustics. *Wave Motion*, **48**, 515-524.
9. Norris, A.N., Amirkulova, F.A. & Parnell, W.J. 2014 (to appear). Active elastodynamic cloaking. *Math. Mech. Solids*, accepted for publications.
10. Guevara Vasquez, F., Milton, G.W., Onofrei, D. & Seppecher, P. 2013. Transformation Elastodynamics and Active Exterior Acoustic Cloaking. *Acoustic Metamaterials*, Springer Series in Materials Science 166, Craster, R.V., Guenneau, S. (eds.)
11. Guevara Vasquez, F., Milton, G.W. & Onofrei, D. 2009. Broadband exterior cloaking. *Optics Express*, **17**, 14800-14805.
12. Guevara Vasquez, F., Milton, G.W. & Onofrei, D. 2011. Mathematical analysis of the two dimensional active exterior cloaking in the quasistatic regime. *arxiv.org/abs/1109.3526v1*.
13. Norris, A.N. & Vemula, C. 1995. Scattering of flexural waves on thin plates. *Journal of Sound and Vibration*, **181**, 115125.
14. Evans, D.V. & Porter, R. 2007. Penetration of flexural waves through a periodically constrained thin elastic plate floating on water. *J. Eng. Math.*, **58**, 317-337.
15. Movchan, A.B., Movchan, N.V. & McPhedran, R.C. 2007. Bloch-Floquet bending waves in perforated thin plates. *Proc. R. Soc. A*, **463**, 2505-2518.
16. McPhedran, R.C., Movchan, A.B. & Movchan, N.V. 2009. Platonic crystals: Bloch bands, neutrality and defects. *Mech. Mater.*, **41**, 356-363.
17. Movchan, N.V., McPhedran, R.C., Movchan, A.B. & Poulton, C.G. 2009. Wave scattering by platonic grating stacks. *Proc. R. Soc. A*, **465**, 3383-3400.
18. O'Neill, J., Selsil, Ö., McPhedran, R.C., Movchan, A.B. & Movchan, N.V. Active cloaking of finite defects for flexural waves in elastic plates. *http://arxiv.org/abs/1403.0816*.

Transformation platonics and cloaking

D.J. Colquitt, M. Brun, M. Gei, A.B. Movchan, N.V. Movchan, and I.S. Jones

Abstract This paper addresses the important issue of transformation elastodynamics as applied to thin plates. The fourth-order partial differential equation governing the motion of flexural waves in thin plates is not invariant with respect to arbitrary changes in coordinate system, but maps to a more general partial differential equation. Nevertheless, as demonstrated in this paper, it is possible to give a physical interpretation to the transformed equation within the framework of the linear theory of pre-stressed plates. This paper provides a formal framework for transformation elastodynamics as applied to thin elastic plates.

1 Introduction

Following the publication of two seminal papers in 2006 [1, 2], there has been very considerable interest in transformation optics, particularly as applied to the design of invisibility cloaks. The foundation of transformation optics is the invariance of Maxwell's equations with respect to coordinate system. In simple terms, an invisibility cloak can be created by deforming a region of space such that a disc is mapped to an annulus. Any objects placed inside the inner radius of the annulus is said to be invisible in the sense that waves will propagate around the annulus as if it were a disc. Unfortunately, the partial differential equations governing other physical systems are not generally invariant under an arbitrary coordinate mapping. In particular Navier's equations, which govern waves in elastic solids, are not invariant under a general change of coordinates [3, 4]. However, it has been shown that a more general constitutive model remains invariant [3]. More recently, it has been shown that approximate elastodynamic cloaking can be obtained by the application of a finite pre-strain [5, 6] or pre-stress [7].

D.J. Colquitt
Department of Mathematics, Imperial College London, South Kensington, London, SW7 2AZ, UK, e-mail: d.colquitt@imperial.ac.uk

Despite the lack of invariance of the equations governing the motion of flexural waves in thin plates, transformation elastodynamics has been used in the design of invisibility cloaks for flexural waves in thin elastic plates [8–10]. The present paper is concerned with the construction of a rigorous transformation theory for the dynamic equations of flexural waves in Kirchhoff-Love plates. In contrast to the elastodynamic case [3–5, 11] and previous work on plates [8, 9], it is shown that it is possible to construct an invisibility cloak for flexural waves in thin plates without recourse to non-symmetric stresses, tensorial densities, or non-linear theories. In particular, it is shown that by the application of appropriate in-plane forces it is possible to construct an exact invisibility cloak for flexural waves within the framework of linear Kirchhoff-Love plate theory. This result could lead to a refinement of the implementation of invisibility cloaks for flexural waves yielding an improvement of the experimental results reported in [10].

2 Transformation platonics

The time-harmonic flexural deformation of an isotropic homogeneous Kirchhoff-Love plate under pure bending is governed by [12]

$$\left(\nabla^4_{\mathbf{X}} - \omega^2 \frac{\mathrm{P}h}{D^{(0)}}\right) w(\mathbf{X}) = 0, \quad \mathbf{X} \in \chi \subseteq \mathbb{R}^2, \tag{1}$$

where ω, P, h, $D^{(0)}$ is the angular frequency, density, plate thickness, and flexural rigidity respectively. Here, $\nabla_{\mathbf{X}}$ denotes the gradient with respect to the original untransformed coordinates. In what follows it is convenient to work in Cartesian coordinates and use Einstein summation convention. The differentiation in the equations below is applied with respect to the vector variable $\mathbf{x}$ in the transformed domain. Consider an invertible transformation $\mathscr{F} : \chi \mapsto \Omega$ and $\mathbf{x} = \mathscr{F}(\mathbf{X})$. In new coordinates equation (1) may be expressed as

$$\begin{aligned} &JG_{ij}G_{k\ell}\,w_{,ijkl} + 2\left(JG_{ij}G_{k\ell}\right)_{,i} w_{,jk\ell} \\ &\quad + \left[G_{ij}(JG_{k\ell})_{,ij} + 2G_{jk}\left(JG_{i\ell,i}\right)_{,j} + G_{ij,i}(JG_{k\ell})_{,j} + JG_{ik,i}G_{j\ell,j}\right] w_{,k\ell} \\ &\quad + \left[G_{ij,i}\left(JG_{k\ell,k}\right)_{,j} + G_{ij}\left(JG_{k\ell,k}\right)_{,ij}\right] w_{,\ell} - \frac{\mathrm{P}h}{JD^{(0)}}\omega^2 w = 0, \end{aligned} \tag{2}$$

where the symmetric tensor $G_{ij} = J^{-1}F_{ip}F_{jp}$ has been introduced, together with the deformation gradient $F_{ij} = \partial x_i/\partial X_j$ and the Jacobian $J = \det\mathbf{F}$. It is clear from equations (1) and (2) that the governing equation is not invariant under arbitrary spatial transformation. Moreover, equation (2) cannot be identified with that governing flexural waves in an anisotropic inhomogeneous Kirchhoff-Love plate, namely: $D_{ijk\ell}w_{,ijk\ell} + 2D_{ijk\ell,i}w_{,jk\ell} + D_{ijk\ell,ij}w_{,k\ell} - h\rho\omega^2 w = 0$. Although the first two terms have the same form as (2), the discrepancy arises in the remaining terms involving

first and second-order derivatives. This discrepancy is irreconcilable, regardless of the choice of material constants in the transformed domain.

Nevertheless, a physically meaningful interpretation may be attributed to the transformed equation (2) by means of an appropriate combination of pre-stress and body forces. In the presence of in-plane forces, the time-harmonic flexural deformation of an inhomogeneous anisotropic Kirchhoff-Love plate is governed by (see, for example, [12])

$$D_{ijk\ell}w_{,ijk\ell} + 2D_{ijk\ell,i}w_{,jk\ell} + \left(D_{ijk\ell,ij} - N_{k\ell}\right)w_{,k\ell} + S_\ell w_{,\ell} = h\rho\omega^2 w, \tag{3}$$

where $D_{ijk\ell}$ are the flexural rigidities, N_{ij} are the membrane forces and S_i are the in-plane body forces. Additionally, the membrane and in-plane body forces are constrained to satisfy the equilibrium equation $N_{ij,j} + S_i = 0$. Using equation (3), the terms in the transformed equation (2) may be identified with physically meaningful quantities. In particular, the flexural rigidities, body forces, and density of the transformed plate are immediately identified

$$D_{ijk\ell} = D^{(0)}JG_{ij}G_{k\ell}, \quad S_\ell = D^{(0)}\left[G_{jk}\left(JG_{il,i}\right)_{,j}\right]_{,k}, \quad \rho = \frac{P}{J}. \tag{4a}$$

The desired symmetry for the membrane forces is obtained by taking $N_{k\ell}$ in the form

$$N_{k\ell} = D^{(0)}\left[\left(JG_{kl}G_{ij,i} - JG_{j\ell}G_{ik,i}\right)_{,j} - G_{jk}\left(JG_{il,i}\right)_{,j}\right]. \tag{4b}$$

It is now straightforward to verify that the membrane and body forces satisfy the in-plane equilibrium equation.

It has thus been demonstrated that, under a general coordinate mapping, the equation governing time-harmonic flexural vibrations of a linear isotropic homogeneous Kirchhoff-Love plate transforms to an equation corresponding to a linear anisotropic inhomogeneous Kirchhoff-Love plate in the presence of in-plane loads. It is emphasised that these loads depend only on the coordinate mapping and are not functions of displacement nor time. In this sense, the membrane forces $N_{k\ell}$ can be interpreted as a pre-stress together with appropriate body forces S_ℓ to ensure equilibrium. This formalism represents a general framework in which transformation elastodynamics for Kirchhoff-Love plates can be investigated. The reader is referred to [13] for further details. The distinguishing feature of this interpretation is that, although a generalised plate model is introduced, the framework is entirely linear and all terms are identified with well understood physical quantities. A further notable feature of the new framework, as above, is that it ensures that the stiffnesses have both major and minor symmetries, the stresses are symmetric and the transformed density is scalar. This is in contrast to the case of cloaks for vector three- and two-dimensional elasticity [4] where there is either a non-symmetric stress [11] or tensorial mass density and dependence of stress on velocity [3].

As a brief example, figure 1 shows the flexural displacement, generated by a point source, for a cloaked and uncloaked void in a Kirchhoff-Love plate. In this case, the cloak is based on a non-singular square push-out transformation previ-

ously introduced in [14]. The corresponding material and geometrical parameters and forces are obtained from the general formalism (4) and can be found in [13], but are omitted for brevity.

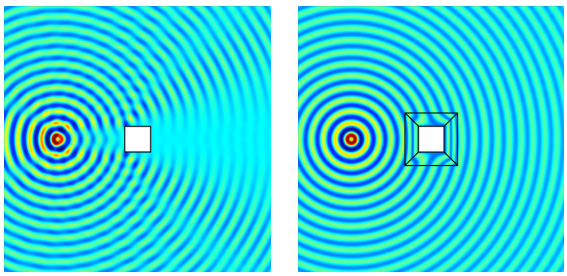

Fig. 1 The flexural displacement generated by a point source in the presence of an uncloaked (left) and cloaked (right) void. The non-dimensional radian frequency $\omega = 200$.

Acknowledgements D.J.C., M.G., A.B.M. & N.V.M. acknowledge the financial support of the European Community's Seven Framework Programme under contract number PIAP-GA-2011-286110-INTERCER2. M.B. acknowledges the financial support of the European Community's Seven Framework Programme under contract number PIEF-GA-2011-302357-DYNAMETA and of Regione Autonoma della Sardegna (LR7 2010, grant 'M4' CRP-27585). D.J.C. also acknowledges the financial support of EPSRC in the form of a Doctoral Prize Fellowship and grant EP/J009636/1.

References

1. Leonhardt U. 2006 Optical conformal mapping. *Science* **312**, 1777–1780.
2. Pendry JB, Schurig D, Smith DR. 2006 Controlling electromagnetic fields. *Science* **312**, 1780–1782.
3. Milton GW, Briane M, Willis JR. 2006 On cloaking for elasticity and physical equations with a transformation invariant form. *New J. Phys.* **8**, 248.
4. Norris A, Shuvalov A. 2011 Elastic cloaking theory. *Wave Motion* **48**, 525–538.
5. Norris A, Parnell W. 2012 Hyperelastic cloaking theory: transformation elasticity with pre-stressed solids. *Proc. R. Soc. A* **468**, 2881–2903.
6. Parnell WJ, Norris AN, Shearer T. 2012 Employing pre-stress to generate finite cloaks for antiplane elastic waves. *Appl. Phys. Lett.* **100**, 171907.
7. Parnell WJ. 2012 Nonlinear pre-stress for cloaking from antiplane elastic waves. *Proc. R. Soc. A* **468**, 563–580.
8. Farhat M, Guenneau S, Enoch S. 2009 Ultrabroadband elastic cloaking in thin plates. *Phys. Rev. Lett.* **103**, 024301.
9. Farhat M, Guenneau S, Enoch S, Movchan AB. 2009 Cloaking bending waves propagating in thin elastic plates. *Phys. Rev. B* **79**, 033102.
10. Stenger N, Wilhelm M, Wegener M. 2012 Experiments on elastic cloaking in thin plates. *Phys. Rev. Lett.* **108**, 014301.
11. Brun M, Guenneau S, Movchan AB. 2009 Achieving control of in-plane elastic waves. *Appl. Phys. Lett.* **94**, 061903.
12. Lekhnitskii S, Tsai S, Cheron T. 1968 *Anistropic Plates*. New York: Gordon and Breach.
13. Colquitt DJ, Brun M, Gei M, Movchan AB, Movchan NV, Jones IS. 2014 Transformation elastodynamics and cloaking for flexural waves. *arXiv* **1401.7579**.
14. Colquitt DJ, Jones IS, Movchan NV, Movchan AB, Brun M, McPhedran RC. 2013 Making waves round a structured cloak: lattices, negative refraction and fringes. *Proc. R. Soc. A* **469**, 20130218.

Bloch wave excitation

Ian Thompson

Abstract The excitation of Bloch waves due to scattering at the edge of a periodic structure is investigated, using a novel approach based on multipole expansions and the z transform. Results showing the proportion of energy reflected back from the edge are presented. Our method can be applied problems involving a variety of different boundary conditions; in particular we do not assume that individual lattice elements scatter waves isotropically.

1 Introduction

During the 1920s, wave propagation through periodic media was used by Felix Bloch as a means of describing the behaviour of electrons in conducting crystals. More recently, a desire to control and direct wave propagation in order to design waveguides, filters and optical fibres has led to applications of Bloch's ideas in several physical contexts, including elastodynamics of composite materials and thin plates, acoustics and photonic crystals [1, 2, 3, 4]. Much of the existing literature is concerned with solving the *propagation* problem, in which modes that may propagate through a given periodic structure are determined. Here, we are concerned with the *excitation* of Bloch waves, and in particular with energy losses due to reflection at an edge. This is motivated by the fact that periodic media are often used as filters, exploiting the fact that Bloch wave propagation is restricted to certain frequency ranges. Clearly the efficiency of such a filter is dependent upon the proportion of incident wave energy that is converted into Bloch waves, and the proportion that is lost due to reflection. These quantities cannot be determined from the wave bearing properties of the medium alone; the excitation problem must be considered.

Ian Thompson
Mathematical Sciences, University of Liverpool, e-mail: ian.thompson@liv.ac.uk

2 Band diagrams and the irreducible Brillouin zone

The standard means of describing the parameter ranges in which waves can propagation through periodic media is the *band diagram*. Suppose that a lattice is formed from objects centred at the points with position vectors

$$\mathbf{R}_{jp} = j\mathbf{s}_1 + p\mathbf{s}_2, \quad j,p \in \mathbb{Z}, \tag{1}$$

where the two-dimensional vectors $\mathbf{s}_1$ and $\mathbf{s}_2$ are not parallel to each other, though they need not be mutually orthogonal. A Bloch wave that propagates through this structure must possess the discrete translational symmetry

$$u(\mathbf{r}+\mathbf{R}_{jp}) = \mathrm{e}^{\mathrm{i}\mathbf{R}_{jp}\cdot\beta}u(\mathbf{r}), \tag{2}$$

for some Bloch wave vector β and all $j,p \in \mathbb{Z}$. Clearly, there is redundancy in allowing β to range over $\mathbb{R}^2$ due to periodicity and symmetry. For example, for the hexagonal lattice with

$$\mathbf{s}_1 = \big[1,0\big] \quad \text{and} \quad \mathbf{s}_2 = \tfrac{1}{2}\big[1,\sqrt{3}\big], \tag{3}$$

nothing is gained by considering vectors β that lie outside the triangle with vertices

$$\Gamma = \big(0,0\big), \quad M = \big(0,\tfrac{2\pi}{\sqrt{3}}\big) \quad \text{and} \quad K = \tfrac{2\pi}{3}\big(1,\sqrt{3}\big), \tag{4}$$

which is called the irreducible Brillouin zone. In many cases of interest (though not all; see [5]), the minimum and maximum frequencies in each band occur when β lies on the boundary of the irreducible Brillouin zone [4, pp. 68–69]. A typical band diagram is shown in fig. 1(a). The basis vectors are given by (3), and the objects forming the lattice are circular cylinders of radius $a = 0.25$. The Helmholtz equation

$$\big(\nabla^2 + k^2\big)u(\mathbf{r}) = 0, \tag{5}$$

applies outside the cylinders, where the wavenumber k is defined as the ratio of frequency to wavespeed, i.e. ω/c. On the surfaces the sound-soft (Dirichlet) boundary condition $u = 0$ is enforced. The frequencies at which propagation is possible can be read off from the band diagram. For the case in fig. 1(a), no modes may propagate for $k \lesssim 4.8$, but there is propagation for $4.8 \lesssim k \lesssim 7.6$. A second stop band occupies $7.6 \lesssim k \lesssim 8.2$, and propagation is again possible for $k \gtrsim 8.2$.

3 Bloch wave excitation

We now consider a semi-infinite lattice, formed from objects centred at the points

$$\mathbf{R}_{jp} = j\mathbf{s}_1 + p\mathbf{s}_2, \quad j \in \mathbb{Z}, \quad p = 0,1,\ldots \tag{6}$$

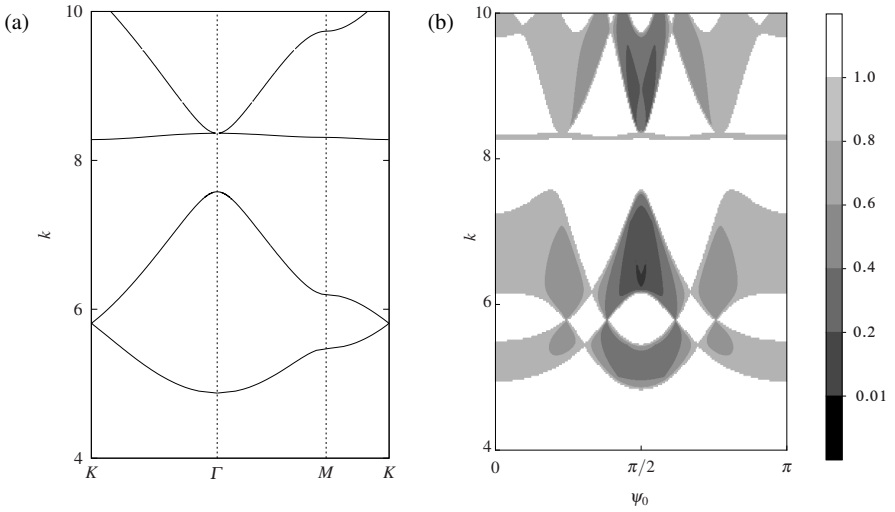

Fig. 1 (a) A typical band diagram. (b) Proportion of incident energy reflected back from the lattice.

so that the region where $y < -a/2$ is empty. This is illuminated by the plane wave

$$u^{\mathrm{i}}(\mathbf{r}) = \mathrm{e}^{\mathrm{i}k(x\cos\psi_0 + y\sin\psi_0)}. \tag{7}$$

The scattered field inherits the one-dimensional quasiperiodicity property

$$u^{\mathrm{s}}(\mathbf{r} + j\mathbf{s}_1) = \mathrm{e}^{\mathrm{i}jks_1\cos\psi_0} u^{\mathrm{s}}(\mathbf{r}) \tag{8}$$

from the incident wave; therefore it has a multipole expansion [6, ch. 4] of the form

$$u^{\mathrm{s}}(\mathbf{r}) = \sum_{n=-\infty}^{\infty} \sum_{p=0}^{\infty} \sum_{j=-\infty}^{\infty} A_n^p \mathrm{e}^{\mathrm{i}jks_1\cos\psi_0} \mathscr{H}_n(\mathbf{r} - \mathbf{R}_{jp}). \tag{9}$$

Here, the outgoing wavefunction is defined as $\mathscr{H}_n(\mathbf{r}) = \mathrm{H}_n^{(1)}(k|\mathbf{r}|)\mathrm{e}^{\mathrm{i}n\theta}$, where $\mathrm{H}_n^{(1)}$ is a Hankel function of the first kind and θ is the anticlockwise angle between the positive x axis and the vector $\mathbf{r} = [x, y]$. The main obstacle to obtaining u^{s} is the lack of quasiperiodicity in the direction parallel to $\mathbf{s}_2$. To overcome this, we represent the unknown amplitude coefficient as a z transform; thus

$$A_n^p = \frac{1}{2\pi\mathrm{i}} \int_{\Omega} A_n^+(z) z^{-p-1} \,\mathrm{d}z, \tag{10}$$

where Ω is a simple closed contour that encircles the origin. The superscript '+' indicates that the functions $A_n^+(z)$ are analytic inside Ω, so the integral evaluates to zero for negative integers p. Applying the boundary conditions on the cylinder surfaces using Graf's addition theorem [6, thm. 2.12] then leads to a Wiener–Hopf equation, which can be solved for $A_n^+(z)$. Ultimately, we are able to determine the

amplitude coefficients in the grating mode expansion for the reflected field, that is

$$u^{\mathrm{s}}(\mathbf{r}) = \sum_{j=-\infty}^{\infty} c_j^- \mathrm{e}^{\mathrm{i}k(x\cos\psi_j - y\sin\psi_j)}, \quad y < 0. \tag{11}$$

where $\cos\psi_j = \cos\psi_0 + 2j\pi/(k|\mathbf{s}_1|)$, and $\sin\psi_j = (1-\cos^2\psi_j)^{1/2}$. Conservation of energy then requires that $E_R + E_T = 1$, where

$$E_R = \frac{1}{\sin\psi_0} \sum_{|\sin\psi_j|\in\mathbb{R}} \left|c_j^-\right|^2 \sin\psi_j. \tag{12}$$

Here, E_R and E_T are the proportions of energy reflected back from and transmitted into the lattice, respectively. A contour plot showing E_R for the structure described in §2 is shown in fig. 1(b). The band structure is clearly consistent with fig. 1(a). However, fig. 1(b) contains information about the behaviour of the field in the pass bands that cannot be deduced from the band diagram. For example, a filter based on this structure will screen out modes with $k \lesssim 4.8$ and $7.6 \lesssim k \lesssim 8.2$, but it will not function well except in a narrow band at near head-on incidence with $k \approx 6.3$, because a large proportion of the incident energy will be lost due to reflection.

4 Conclusions

We have developed a technique for calculating the proportion of incident energy reflected back from the surface of a periodic structure. This has implications for the design of efficient components that exploit the wave-bearing properties of periodic media. Full details of our method, along with additional results, are given in [7].

References

1. M. Sigalas and E. N. Economou. Band structure of elastic waves in two dimensional systems. *Solid State Commun.*, 86(3):141–143, 1993.
2. A. B. Movchan, N. V. Movchan, and R. C. McPhedran. Bloch–Floquet bending waves in perforated thin plates. *Proc. Roy. Soc. Lond., A*, 463:2505–2518, 2007.
3. P. Russell. Photonic crystal fibers. *Science*, 299:358–362, 2003.
4. J. D. Joannopoulos, S. G. Johnson, J. N. Winn, and R. D. Meade. *Photonic crystals. Molding the Flow of Light*. Princeton University Press, 2nd edition, 2008.
5. R. V. Craster, T. Antonakakis, M. Makwana, and S Guenneau. Dangers of using the edges of the Brillouin zone. *Phys. Rev. B*, 86:6 pages, 2012.
6. P. A. Martin. *Multiple Scattering. Interaction of Time-Harmonic Waves with N Obstacles*. Cambridge University Press, 2006.
7. N. Tymis and I. Thompson. Scattering by a semi-infinite lattice of cylinders and the excitation of Bloch waves. Submitted to Q. J. Mech. Appl. Math. in October 2013 (31 pages)[1]

[1] `http://research-archive.liv.ac.uk/13973`

Electric control of ultrasonic propagation in a Phononic Crystal using piezoelectric materials

Sid Ali Mansoura[(1)], Pierre Maréchal[(1)], Bruno Morvan[(1)], Bertrand Dubus[(2)].

(1) LOMC, UMR 6294 CNRS, Université du Havre, 75 rue Bellot, 76600 Le Havre.
(2) IEMN, UMR 8520 CNRS, ISEN, 41 Boulevard Vauban, 59800 Lille.

Phononic crystals (PC) are periodic structures composed of periodic arrangement of unit cells in one or several directions. The propagation of ultrasound in these structures is determined by the presence of bandgaps which leads to strong attenuation frequency bands. In this study we propose to include piezoelectric materials in PC in order to achieve an active control of the propagation of ultrasonic waves.

The control is obtained by connecting an external electric circuit to the electrodes of the piezoelectric inclusions. The nature of the electric circuit (capacitance, inductance,...etc) affects the ultrasonic transmission through the PC and is mainly governed by the electro-mechanical coupling factor of the piezoelectric material. In this study, we are interested in the propagation of ultrasound into a one dimensional PC. Two cases are considered depending on whether the PC is made of an alternance of piezoelectric and passive plates or exclusively made of piezoelectric layers.

Using the basic piezoelectric equation governing the wave propagation along the thickness of the layer and applying the Bloch-Floquet conditions on the unitary cell of the PC, we obtain the dispersion curves of the waves. We study the effect of the electric boundary condition on the band structure for various connected electrical circuits. Experimental measurements are also performed which demonstrate the possibility to create or shift bandgaps with an external electric control.

Low frequency ultrasound propagation in layered media

David Gunn, Simon Holyoake and Ben Dashwood

Abstract: Long duration, low frequency modulated ultrasound is used for characterising systems comprising layers of highly attenuating media. Maxima (notches) in the transmission (reflection) spectra relate to half-wavelength resonance across the target thickness. The resolution of the spectral thickness measurement can be improved by reducing the increment of the frequency bins. Estimation of attenuation is achieved via fitting the reflected and transmitted spectra to a forward propagating wave using a transfer matrix.

1 Introduction

Ultrasound spectroscopy involves the analysis of the spectral characteristics of echos and invariably uses fast rise, broadband pulses of MHz frequencies or above [1]. While ultrasound spectroscopy is widely used for material property and structural inspection, the use of high frequencies can be limited in materials with very high attenuation. Because of its greater penetration, low frequency ultrasound (20 kHz-200 kHz) offers an alternative inspection approach in materials where MHz frequencies are highly scattered [2]. In layered sequences under normal incidence, wave propagation within the bound layers is partially transmitted and reflected at the bounding interfaces, where the internally reflected partial energy returns to the near face to be partially transmitted and reflected again. Transmissivity and reflectivity functions of layered systems have characteristic spectral notch signatures that vary not only to changes in layer thicknesses but also with the introduction of small water gaps between the solid media. Hence, while the use of long duration, low frequency modulated ultrasound is a shift away from routine ultrasonic spectroscopy, it presents a potentially viable technological basis for inspecting the condition of challenging layered systems that can be found in many medical, NDT and engineering disciplines.

2 Signals for delivery of broadband ultrasonic energy

The sensitivity-bandwidth of the transmitting and receiving ultrasonic probes limit the signal frequency band that can be delivered for insonifying targets. The

David Gunn: dgu@bgs.ac.uk; Simon Holyoake: simho@bgs.ac.uk; Ben Dashwood: bendas@bgs.ac.uk
British Geological Survey, Keyworth, Nottingham, UK.

probes used in this study were considered to have a usable energy-bandwidth of at least 50 kHz to 180 kHz. To incorporate this frequency band, stationary and non-stationary test signals were designed to begin at a maximum frequency of 40 kHz and end at a minimum frequency of 200 kHz. Good results were obtained with non-stationary signals where frequency modulation throughout the signal duration was controlled by linear, quadratic and cosine functions.

3 Experimental Facility

The experimental test facility comprised a water tank (1.65 m × 1.43 m × 0.90 m) and infrastructure for the mounting and positioning of transducers and target materials within the tank. Transducers comprised piezoelectric-composite active main elements that were high in sensitivity and had a -3 dB fractional bandwidth approaching 80 % around 100 kHz (Alba Ultrasound Ltd.). The positioning system facilitates X, Y, Z and rotational positioning of the transducers with a positioning reproducibility of ± 116 μm. The test signals were generated and acquired using a high-specification modular system containing: a ZT530PXI (Ztec Instruments Inc.) 16-bit arbitrary waveform generator (AWG) and a ZT410PXI 16-bit digital storage oscilloscope (DSO). A computer program written in the C++ language has been developed in-house to automate the signal transmission and reception procedure. The experimental set-up is shown in Figure 1, where ultrasonic signals are propagated from the transmitting transducer (Tx) to the receiving transducer (Rx), either through water (Set-up 1), or through a target system (Set-up 2); a reflected signal is also detected on the Tx and acquired when a target is in place. The targets used in this study include single and 3-layer media, nominally of 298 × 210 mm face size. (Although this published abstract only presents results from the single layer tests.) The target was approximately centred between transducers that were set approximately 1 m apart. Signals were propagated with the target present and also with the target absent in order to acquire a reference signal through water, where required. During the experiments, the mean temperature of the water was nominally 19.0 ° C.

4 Results

Examples of time domain linear FM signals received after reflection from, and transmission through single layer targets are shown in Figures 2a, b. Examples of these reflected and transmitted signals transformed into the spectral domain and normalised (via spectral division) using the transducer Tx-Rx function through water are shown in Figure 3. The spectral responses show periodic features related to the half wavelength resonance across the thickness of the targets, which is dependent upon the ultrasound phase velocity through the target material. The first maximum in the transmission spectrum (or minimum in the reflection spectrum) occurs at the fundamental frequency, where the thickness equals half the wave-

length; subsequent maxima/minima occur at multiples of the fundamental frequency [2,3]. The spectral shape is indicative of the mechanical Q factor, which is related to attenuation coefficient, α by $\alpha = \pi f/Qv$, where $Q = f_0/(f_1 - f_2)$, where f_0 is the mechanical resonance frequency, f_1 and f_2 are the frequencies where energy is half that at resonance, and v is the velocity.

A transfer matrix approach was used to model the propagation of a forward travelling wave incident upon the front face of an arbitrary front layer through an arbitrary number of layers. Attenuation coefficients were calculated using,

$$\alpha (f) = a.f + b.f^2 \qquad 1$$

where the parameters, a and b were found by curve fitting the modelled data to the experimental data. These parameters are then used to produce modelled data for differing thicknesses of the same material. Figure 3 compares the modelled and experimental spectra for polypropylene. Table 1 summarises the velocity and attenuation values determined from the experimental and modelling programme.

5 Conclusions

A new method is described that enables ultrasonic material characterisation to be performed in the 40–200 kHz range. The study shows material discrimination is possible based on both temporal and spectral results. Transformation into the spectral domain and using small increments between frequency bins enables a thickness resolution of a far smaller length than the wavelengths of the propagating sound. This approach has potential applications in areas such as NDT & E, medical physics, and geophysics, where improved resolution is sought using lower frequencies to overcome the problem of highly attenuating media.

References

1. Hedrick, WR, Hykes, DL & Sarchman, DE (2005). Ultrasound physics and instrumentation, 4th Ed. Elsevier Mosby.
2. Hopper, C., Assous, S., Gunn, D.A., Jackson, P.D., Wilkinson, P.B., Rees, J.R., O'Leary, R.L.& Lovell, M.A. (2012). Bio-inspired low frequency material characterisation. Advances in Acoustics and Vibration. Research Article 927903.
3. Mikeska EE and Behrens JA. Evaluation of transducer window materials. J Acous. Soc. Am. 1976; 59(6): 1294-9

Acknowledgements

This paper is published with the permission of the Executive Director of the British Geological Survey (NERC).

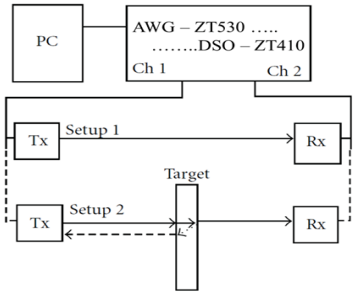

Figure 1: Experimental set-up showing the testing layout and instrumentation-transducer connections.

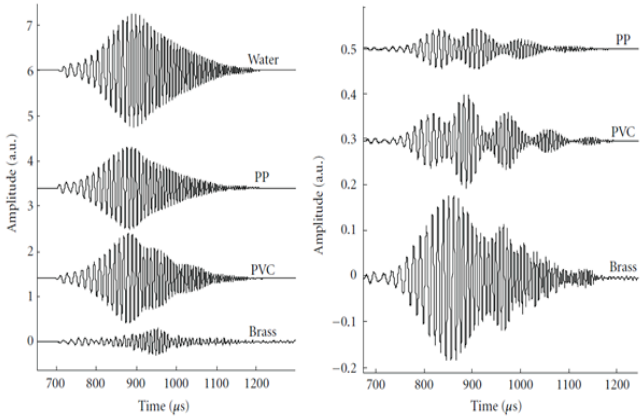

a. Transmission signals. b. Reflection signals.

Figure 2: Temporal linear FM signals with frequency band 40 – 200 kHz. a. Transmitted through water with no target [Water]; through water with 40 mm thick targets of polypropylene [PP], polyvinylchloride [PVC] and brass [Brass]. b. Echo reflection signals from PP, PVC and brass targets.

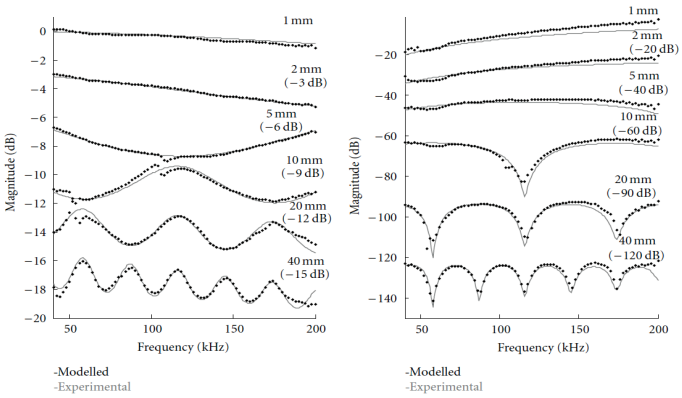

a. Transmission signals. b. Reflection signals.

Figure 3: Experimental (black diamonds) and modelled (grey lines) spectra for polypropylene targets of various thicknesses, obtained using the linear FM chirp; traces are offset by the values shown in brackets.

Material	Sound velocity (ms^{-1})	Attenuation coefficients ($Npm^{-1}Hz^{-1}$)	
		a	b
PP	2520 ± 20	$(82 \pm 3) \times 10^{-6}$	$(-73 \pm 7) \times 10^{-6}$
PVC	2320 ± 20	$(30 \pm 3) \times 10^{-6}$	$(15 \pm 7) \times 10^{-6}$
Brass	4560 ± 20	$(6 \pm 3) \times 10^{-6}$	$(68 \pm 7) \times 10^{-6}$

Table 1: Ultrasonic velocities and attenuation coefficients determined for single layer materials.

A multi-frequency, model based method for sizing cracks in an elastic solid.

Laura Cunningham and Anthony J. Mulholland

Abstract In this paper a model based method is presented for sizing cracks within an elastic solid. This method is derived from the Kirchhoff model which is a high frequency approximation to the scattering of a linear elastic wave from an ellipsoid within a homogeneous medium. This multi-frequency method provides a formula which relates the crack size to the maximum eigenvalue of the associated scattering matrix as extracted from the model. To illustrate the method, scattering matrices are extracted from finite element simulated data recorded by an ultrasonic array from a homogeneous medium which contains a crack.

1 Introduction

Ultrasonic arrays are used extensively to inspect safety critical infrastructures for defects, such as cracks [2]. There are several image processing techniques [1]-[4] which can be used to detect and charactise defects within elastic solids, however these methods are subjective when estimating the crack size (often relying on an empirical thresholding of a point spread function). In this paper a mathematical model is used to present an objective method for sizing cracks within an elastic solid.

2 Kirchhoff model and scattering matrices

The Kirchhoff model [5] is used here to provide a high frequency approximation to the scattering of an elastic wave from an object in a homogeneous medium. The signals scattered from a crack in the host material are then represented in the frequency domain by scattering matrices, which are a function of the incident and scattered waves. The Kirchhoff model is derived using a full aperture, circular array; however

Laura Cunningham
University of Strathclyde, 26 Richmond Street, Glasgow, UK, G1 1XH e-mail: l.cunningham@strath.ac.uk

Dr Anthony Mulholland
University of Strathclyde, 26 Richmond Street, Glasgow, UK, G1 1XH e-mail: anthony.mulholland@strath.ac.uk

in this work an approximation to a linear, limited aperture array is used. From observations on the nature of the scattering matrices that arise from ellipsoidal cracks and limited aperture transmit/receive directions the scattering matrix can be approximated as a symmetric Toeplitz matrix. Here the row where the maximum of a scattering matrix occurs will be used to create a Toeplitz approximation A_T, which is given by

$$A_T(y_p) = \frac{2\sqrt{1-\triangle y^2/4}(L+2\mu(1-y_p^2))}{\rho c^2(2y_p-\triangle y)} J_1\left(2\pi\hat{a}\left(y_p - \frac{\triangle y}{2}\right)\right), \qquad (1)$$

where $\hat{a} = a/\lambda$ is crack radius over wavelength, c is the wavespeed in the host material, ρ is the host material density, J_1 is a Bessel function of the first kind, y_p is the **j**-axis component of the unit vector associated with array element with index p, $\triangle y$ is the pitch between array elements and L, μ are the Lamé coefficients. We then derive an approximation to the maximum eigenvalue σ_{max} of this Toeplitz approximation to the scattering matrix. This maximum eigenvalue is approximated using an upper bound [6], σ_B, which is given by

$$\sigma_B = (A_T)_1 \cdot \mathbf{w} \qquad (2)$$

where $(A_T)_1 = ((A_T)_{1,1}, |(A_T)_{1,2}|, ..., |(A_T)_{1,N}|)$, $\mathbf{w} = (1, w_2, ...w_n)$ and

$$w_j(N) = 2\cos\left(\frac{\pi}{\lfloor \frac{N-1}{j-1} \rfloor + 2}\right) \qquad (3)$$

where N is the number of array elements. Approximations are made to the Bessel function within $(A_T)_1$ from equation (1), followed by Taylor series approximations in order to extract the parameter $\hat{a}$ from equation (2) to obtain an explicit expression relating $\hat{a}$ to the maximum eigenvalue from the scattering matrix. The final approximation to σ_B is

$$\begin{aligned}\sigma_B(\hat{a}) = &(\hat{A}+\hat{S}_1)\hat{a} + \hat{S}_2\hat{a}^3 + Q(\hat{a})\cos(p(\hat{a}) - \phi(\hat{a})) \\ &+ \mathscr{O}(\max\{e_2, e_3, e_4, e_5\} + \max\{e_1, e_6\})\end{aligned} \qquad (4)$$

where $\hat{A}, \hat{S}_1, \hat{S}_2, Q, p$ and ϕ are functions of the depth of the crack, d, the length of the ultrasonic array, l and the number of elements in the array, N.

3 Results from simulated data

In this section, the method outlined in Section 2 is applied to finite element simulated data which simulates the scattering from a crack of length 5mm ($a = 2.5$mm) within a homogeneous medium. The maximum eigenvalues associated with each scattering matrix from the simulated data across a range of frequencies are com-

pared with those calculated directly from the Kirchhoff model. The scattering matrices from the simulated data and from the model are normalised with respect to the l^2-norm to allow the signatures of each to be compared as crack radius, a, and frequency, f are varied. Let $\sigma_S(f)$ denote the maximum eigenvalue from the simulated data associated with the normalised scattering matrix at a fixed frequency, f, and let $\sigma_K(a,f)$ denote the maximum eigenvalue from the Kirchhoff model at a frequency f and for a crack of radius a. Figure 1 (a) shows the plot of σ_S (blue line) across the bandwidth of the ultrasound transducer array ($0.75-2.25$MHz) and compares this with σ_K from the model for different values of crack radii, a. This plot shows that $\sigma_S(f)$ compares well with $\sigma_K(a,f)$ for crack radii between 2mm and 2.5mm. The difference between the model and the simulated data can then be quantified via

$$D(a) = ||\sigma_S(f) - \sigma_K(a,f)||_2. \tag{5}$$

Figure 1 (b) plots $D(a)$, as the crack radius, a, is varied within the model and shows

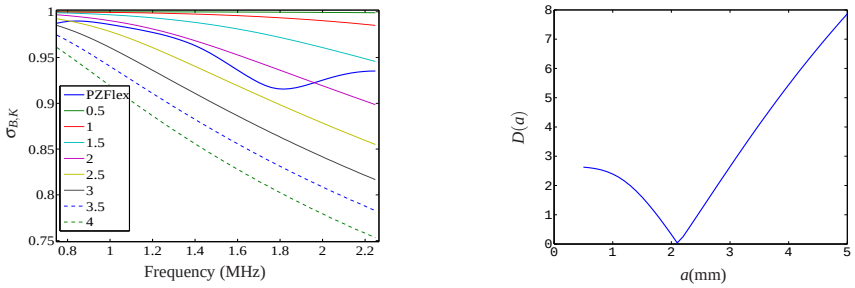

Fig. 1: Figure (a) shows the maximum eigenvalue, $\sigma_S(f)$, from the scattering matrices extracted from the simulated data (thick blue line) as a function of frequency and compares this with the maximum eigenvalue, $\sigma_K(a,f)$ from the scattering matrices determined using the Kirchhoff model for different crack radii. Figure (b) quantifies this difference via $D(a)$ in equation (5).

a clear minimum for $a = 2.2$mm.

4 Sensitivity Analysis

The expression given by $\partial\sigma_B/\partial\hat{a} \times \hat{a}/\sigma_B$ provides a relative measure of how sensitive σ_B is to changes in the crack size over the wavelength $\hat{a}$. This provides a guide as to how useful this method will be in practice in recovering the crack size from a given maximum eigenvalue (the so called inverse problem).

Figure 2 shows this relative error as $\hat{a}$ is varied and shows that for $\hat{a} < 0.6$ the relative derivative is close to one which illustrates that changes in σ_B are sensitive

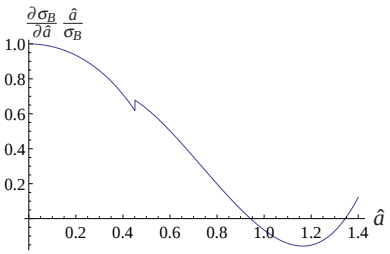

Fig. 2 The relative derivative of the maximum eigenvalue, σ_B, with respect to $\hat{a}$ as a function of $\hat{a}$, all other parameters fixed at N=64, l=128mm and d=50mm in each respective case.

to changes in $\hat{a}$. This is encouraging as it indicates that this crack sizing method is sensitive to changes in σ_B for subwavelength cracks.

5 Conclusion

A multi-frequency, model-based crack sizing method has been developed which relates the radius of a crack within an elastic solid to the maximum eigenvalue from a scattering matrix. An analytical expression has been derived relating the crack radius to this maximum eigenvalue which allows the ability of the crack sizing method to be assessed. The method was successfully applied to finite element simulated data from a homogeneous medium with a crack inclusion.

References

1. L. Borcea, G. Papanicolaou and C. Tsogka, Coherent interferometric imaging in clutter, *Geophysics*, V. 71, No 4, p. 165-175, 2006.
2. A. Velichko and P D Wilcox, An analytical comparison of ultrasonic array imaging algorithms, *JASA*, V. 127, No 4, p. 2378-2384, 2010.
3. A. Aubry and A. Derode: Detection and imaging in a random medium: A matrix method to overcome multiple scattering and aberration, *J. Appl. Phys.*, V.106, No 4,2009.
4. C. Prada, S. Manneville, D. Spoliansky, and M. Fink: Decomposition of the time reversal operator: Detection and selective focusing on two scatterers, *JASA*, V. 99, No 4, p. 2067-2076, 1996.
5. L. W. Schmerr: Fundamentals of ultrasonic non-destructive evaluation: A modelling approach, *Plenum Press*, 1998.
6. D. Hertz: Simple bounds on the extreme eigenvalues of Toeplitz matrices, *IEEE Trans. Inform. Theory.*,V. 38, No 1, p. 175-175, 1992.

Array imaging of austenitic welds by measuring weld material map

Michael Lowe and Zheng Fan

Abstract

It is difficult to inspect for defects in austenitic welds ultrasonically due to complicated material properties inside the weld. Weld microstructures typically lead to weld stiffnesses that are both anisotropic and inhomogeneous, so that ultrasonic waves tend to deviate and scatter. A weld performance map is commonly used to describe how the material properties vary throughout the weld, and this idea has been applied to wave propagation models. In this work, we have developed a non-destructive method to measure this map using ultrasonic arrays. A material model (previously published by others) with a small number of parameters has been applied to describe the weld performance map. It uses the information of the welding procedure and rules for crystalline growth to predict the orientations, therefore it has a good physical foundation. An inverse model has then been developed to measure the weld performance map based on the matching of predictions by the ray tracing method to selected experimental array measurements. The process is validated by both finite element models and experiments. The results have been applied to correct array images to compensate for deviations of the ultrasonic rays.

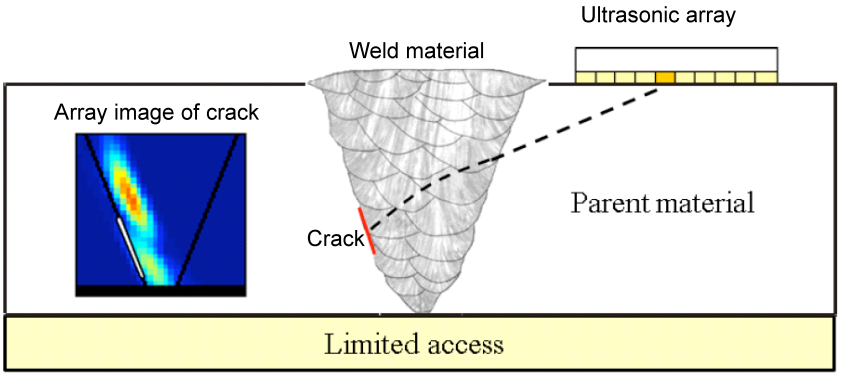

Figure 1. Illustration of error in ultrasonic array imaging when the imaging is performed through inhomogeneous weld material.

Michael Lowe
Dept Mech Eng, Imperial College, UK, e-mail: m.lowe@imperial.ac.uk

Zheng Fan
Mech & Aero Eng, Nanyang Tech University, Singapore 639798, e-mail: zfan@ ntu.edu.sg

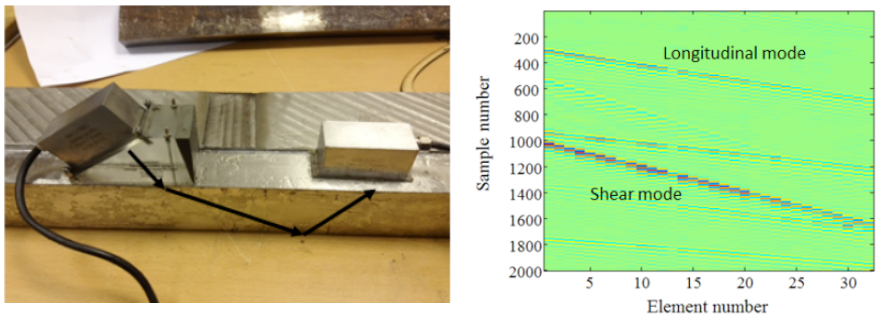

Figure 2. Experimental measurements to obtain data for the inversion calculation to find the weld material map.

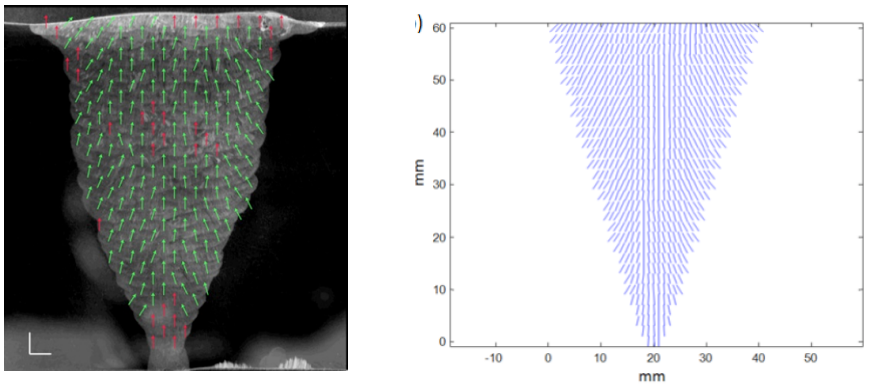

Figure 3. Confirmation of inversion methodology: macrograph of weld (left) and weld map obtained by inversion of ultrasonic measurements (right). NB this step is only performed for the validation of the research; destructive examination is not required in the deployment of the method.

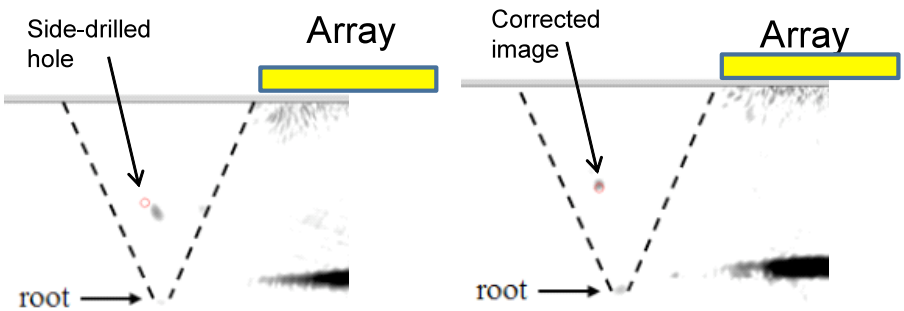

Figure 4. Example of deployment of the method. Image on left obtained using normal array imaging, showing incorrect location of a side-drilled hole. Image on right shows the correction of the location to its true position by the new method.

Spatially resolved acoustic spectroscopy: a laser ultrasonic technique for materials characterisation

Wenqi Li, Steve Sharples

Abstract Material characteristics such as strength, stiffness and fracture resistance are strongly related to the underlying microstructure. In order to predict the mechanical behaviour of industrial materials such as titanium, nickel and their alloys, detailed knowledge about their texture is required. A robust measurement tool is introduced which can be used to determine the crystallographic orientation of a material. This is achieved by using a laser ultrasonic technique spatially resolved acoustic spectroscopy (SRAS) combined with a numerical surface acoustic wave (SAW) velocity model. The SRAS technique can be used to obtain SAW velocity information on the local area where the waves are generated. There are two ways to implement the technique; in both methods the SAW excitation pattern is generated by projecting a grating pattern of laser light. By varying the frequency by using a broadband laser in combination with a fixed grating, the local velocity v can be calculated, through v = f where f is the frequency and is the grating period. The model predicts the SAW velocity from the material's elastic constants; a search algorithm termed the overlap function is used to compare the SRAS data to the model to determine the crystallographic orientation. We examined a range of materials commonly used for industry. Comparisons between SRAS and electron backscattered diffraction are presented. This is an innovative and all-purpose NDT technique for materials manufacture monitoring and quality control.

Wenqi Li
University of Nottingham, University Park, Nottingam, UK, NG7 2RD, e-mail: Wenqi.Li@nottingham.ac.uk

Steve Sharples
University of Nottingham, University Park, Nottingam, UK, NG7 2RD, e-mail: Steve.Sharples@nottingham.ac.uk

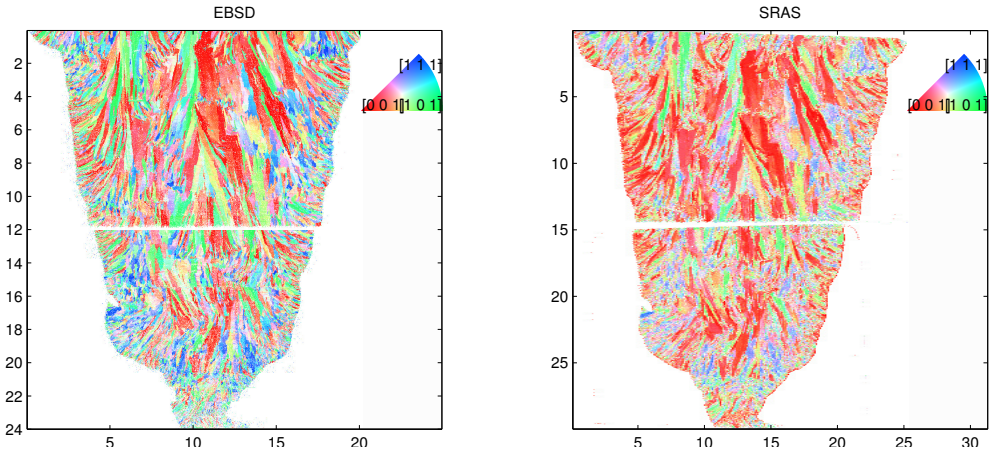

Fig. 1 Comparison between EBSD (left) and SRAS (right) of an Inconel sample.

Ultrasonic Characterisation of Crack-Like Defects from Scattering Matrices

Long Bai, Alexander Velichko and Bruce W. Drinkwater

Abstract A novel approach for the characterisation of cracks with subwavelength dimensions has been proposed. The crack length and orientation angle are determined by measuring the similarity of the scattering matrix of the target defect and those of reference cracks. The similarity is calculated in terms of the Pearson correlation coefficient, and when there are multiple peaks in the correlation image, structural similarity index is used to distinguish between them. In addition, scattering matrix with high level of measurement noise can be correctly characterised by the application of the principal component analysis to the noisy data.

1 Introduction

Crack-like defects form an important type of target defects in non-destructive evaluation [1], and accurate characterisation of them remains a challenge at the moment, particularly for small cracks and inclined cracks. Previous work on the characterisation of small cracks includes vector-TFM (VTFM) [2] and sizing algorithms based on the scattering matrix [3, 4]. However, sizing was not considered in VTFM, and scattering-matrix-based algorithms could only work when specular reflection is included in the scattering matrix.

Due to the finite aperture of ultrasonic array, the incident and scattering angles are limited in the extracted scattering matrix. Figure 1 shows the geometry of measurement configuration for the extraction of scattering matrix from simulated array

Long Bai · Alexander Velichko · Bruce W. Drinkwater
Department of Mechanical Engineering, University Walk, University of Bristol, Bristol BS8 1TR, UK, e-mail: lb13340@bristol.ac.uk

Alexander Velichko
e-mail: a.velichko@bristol.ac.uk

Bruce W. Drinkwater
e-mail: b.drinkwater@bristol.ac.uk

data. The angular coverage of the defect is determined by array aperture size and defect location. Figure 2(a) and (b) show the magnitude of scattering matrices (at 5MHz) of 1.00mm (0.79λ), 0°, and 1.20mm (0.95λ), -70° (measured anticlockwise) cracks, respectively, which are contaminated by 20% random zero-mean Gaussian measurement noise. The relative noise level, n_σ is defined with respect to the peak magnitude A_P, of the scattering matrix of 1.00mm, 0° crack:

$$n_\sigma = \frac{W_\sigma}{A_P} \times 100\%, \tag{1}$$

where W_σ represents the standard deviation of the random noise. In this paper, crack-like defect characterisation based on the scattering matrices as shown in Fig. 2 is studied.

2 Methodology and preliminary results

The first step of the proposed approach is to form the database which consists of scattering matrices of the reference cracks. The reference cracks have lengths ranging from 0.2mm (0.16λ) to 2mm (1.6λ) (in 0.05mm interval), and orientation angles of -85° to 90° (in 5° interval). Before measuring the similarity of the scattering matrices, principal component analysis (PCA) [5] is applied to the noise data as the de-noising procedure, where the reference cracks serve as the training set [5]. Figure 3(a) and (b) show the de-noised scattering matrices that are shown in Fig. 2(a) and (b), respectively.

Pearson correlation coefficient [6] is calculated as the similarity measure. Figure 4(a) and (b) are the correlation images, which show the correlation coefficients calculated between the de-noised scattering matrices and those of the reference cracks. The peak in Fig. 4(a) represents the found match, and the length and orientation angle of the crack have been precisely determined by the correlation coefficient metric.

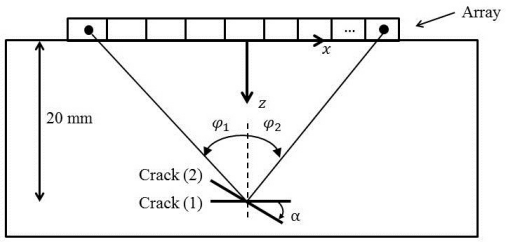

Fig. 1 Geometry of scattering matrix measurement

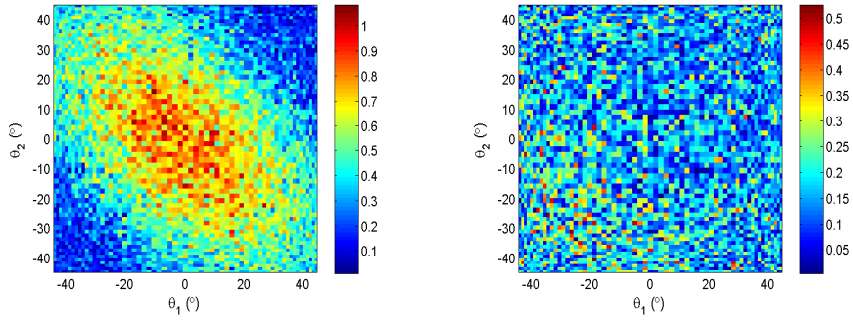

(a) 1.00mm (0.79λ), 0° crack **(b)** 1.20mm (0.95λ), -70° crack

Fig. 2 Scattering matrices with noise

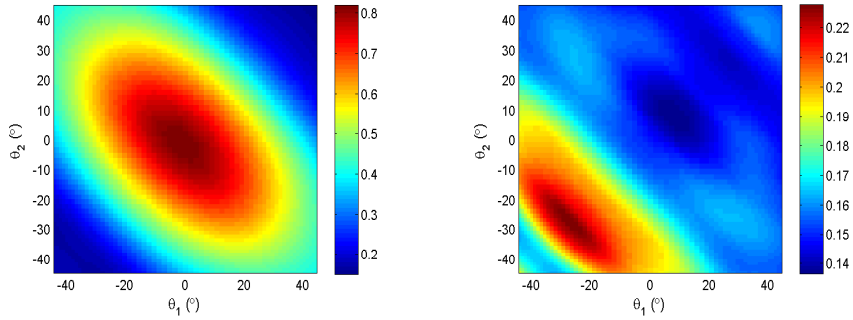

(a) 1.00mm (0.79λ), 0° crack **(b)** 1.20mm (0.95λ), -70° crack

Fig. 3 Scattering matrices (de-noised)

For the correlation image shown in Fig. 4(b), there are three peaks that are at different locations and have similar values. To distinguish between these peaks, mean structural similarity index (MSSIM) [7] can be calculated and used as the second similarity metric. The correlation coefficient and MSSIM associated with peaks 1-3 are specified in Table 1. It can be seen that although the three peaks have similar values in terms of correlation coefficient , peak 2 is the best match because of its largest MSSIM value.

In conclusion, if there is only one peak in the correlation image, it is found as the final match. If there are more than one peaks, they should be distinguished by MSSIM, and the found match is assigned to the peak having the maximum MSSIM among the candidates. This algorithm has been validated by various simulation and experimental cases, and more details will be reported in the final paper.

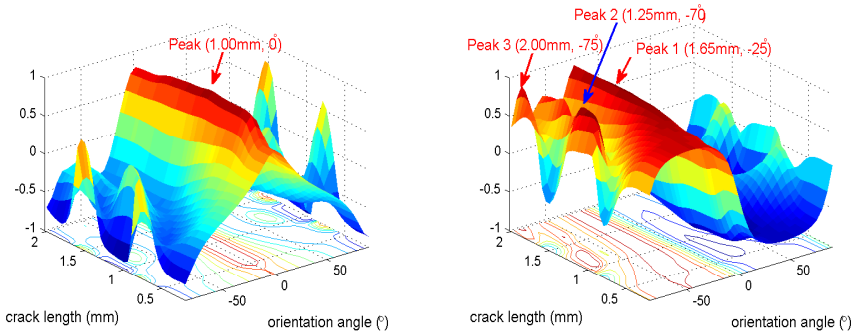

(a) 1.00mm (0.79λ), 0° crack **(b)** 1.20mm (0.95λ), -70° crack

Fig. 4 Correlation images calculated for de-noised scattering matrices

Table 1 Correlation coefficient and MSSIM of peaks 1-3 in Fig. 4(b)

Reference crack	correlation coefficient	MSSIM
peak 1 (1.65mm, -25°)	0.9384	0.3150
peak 2 (1.25mm, -70°)	0.9366	0.4550
peak 3 (2.00mm, -75°)	0.8691	0.3164

References

1. J. D. Achenbach: Quantitative Nondestructive Evaluation, *Int. J. Solids Struct*, V. 37, p. 13-27, 2000.
2. P. D. Wilcox, C. Holmes and B. W. Drinkwater: Advanced Reflector Characterization with Ultrasonic Phased Arrays in NDE Applications, *IEEE Trans. Ultrason., Ferroelectr., Freq. Control*, V. 54, p. 1541-1550, 2007.
3. J. Zhang, B. W. Drinkwater and P. D. Wilcox: Defect Characterization Using an Ultrasonic Array to Measure the Scattering Coefficient Matrix, *IEEE Trans. Ultrason., Ferroelectr., Freq. Control*, V. 55, p. 2254-2265, 2008.
4. J. Zhang, B. W. Drinkwater and P. D. Wilcox: The Use of Ultrasonic Arrays to Characterise Crack-Like Defecsts, *J Nondestruct Eval*, V. 29, p. 222-232, 2010.
5. M. Turk and A. Pentland: Eigenfaces for Recognition, *J. Cognitive Neurosci.*, V. 3, p. 71-86, 1991.
6. K. Pearson: Contributions to The Mathematical Theory of Evolution, III, Regression, Heredity, and Panmixia, *Philos. Trans. R. Soc. Lond. Ser. A*, V. 187, p. 253-318, 1896.
7. Z. Wang, A. C. Bovik, H. R. Sheikh and E. P. Simoncelli: Image Quality Assessment: From Visibility to Structural Similarity, *IEEE Trans Image Process.*, V. 13, p. 600-612, 2004.

The Aeroacoustics of the Owl

Nigel Peake, DAMTP, University of Cambridge

Many (but not all) species of owl can hunt in acoustic stealth. This requires virtually silent flight in the frequency ranges over which both its prey's and its own auditory systems are most sensitive (to avoid alerting the prey to the owl's approach, and so that the owl can detect the prey audibly above its own self noise, respectively). The question of precisely how the owl actually manages to fly so quietly has remained open, but it has long been appreciated that owls which need to hunt silently possess two unique features, which are not found on any other bird, and indeed are not even found on owls which do not need to hunt silently (e.g small owls which feed on insects, or Fish Owls). First, the microstructure of the feathers on the upper wing surface is exceedingly complex, with an array of hairs and barbs which form a thick canopy just above the nominal wing surface. Second, the wing trailing edge possesses a small flexible and porous fringe which does not seem to have an obvious aerodynamic function.

The research I am going to describe in this talk is part of an ongoing theoretical (at Cambridge, Lehigh University and Florida Atlantic University) and experimental (at Virginia Tech.) program, with the aims of first attempting to understand how the two unique owl features described above actually work to control the noise, and then second of designing an owl-inspired treatment which can be used to significantly reduce aerodynamic noise generation in an engineering context. The application we have in mind initially is to noise generation by onshore wind turbines. The progam is funded by the US Office of Naval Research.

When considering possible noise sources for a bird in flight, or a wind turbine, one immediately thinks of the noise produced by the turbulent boundary layer flowing over the wing trailing edge: this noise scales with the flow Mach number to the power 5, which is louder than the power 6 scaling of rough-surface noise, or the power 8 scaling of turbulence in free space. Our hypothesis is that the owl has been able to eliminate this trailing-edge noise, using a combination of the feather canopy and the trailing-edge fringe.

Turning to specifics, I will describe mathematical analysis of the following problems: (i) noise generation by turbulence close to a semi-infinite elastic and porous trailing edge, using scalar Wiener-Hopf; (ii) the effects of finite geometry on this noise generation, using matrix Wiener-Hopf; (iii) the possible role of

Name of First Author
Name, Address of Institute, e-mail: name@email.address

Name of Second Author
Name, Address of Institute e-mail: name@email.address

shear sheltering on reducing the level of surface pressure fluctuations. I will also describe results from the experiments.

The material in this talk is joint work of NP & Conor Daly (Cambridge), Justin Jaworski (Lehigh), Stewart Glegg (Florida Atlantic), and Ian Clark, Nathan Alexander & William Devenport (Virigina Tech.).

Remarks for non destructive testing in a bi-material based on Love waves

Philippe Destuynder and Caroline Fabre

Abstract Let us consider an infinite strip made of two different materials. The background problem considered, consists in detecting the presence of a crack at the interface between the two media using Love waves [1]. First of all, an energetical invariant in the wave equation is derived from domain derivative methods. It gives indications on the existence of a crack between two transverse observation lines. The localisation is more difficult and could be deduced from an optimal control strategy which requires a mathematical model for simulating the Love waves which propagate along the strip. The main advantage would be to explore longer domains compared to the standard ultrasonic method which requires to move step by step an actuator transversally to the boundary between the two media. A mathematical model is therefore introduced. In order to restrict the simulation to a finite domain, one can use transparent boundary conditions on two transverse lines to the interface between the two media. Even in the case of simple Love waves (compared to Lamb's waves [5]), a new difficulty appears because of a singularity which is not physical and which pollutes the evaluation of the energetical invariant. The goal of this presentation is to examine the different aspects of this strategy for non destructive testing which has been suggested by several authors [2] [3], [4]. The model which is used in this presentation is very much simplified compared to reality, but it enables to point out the possibilities and the difficulties of the non destructive testing method based on Love waves.

Philippe Destuynder
Laboratoire de modélisation mathématique et numérique, CNAM, 292, rue saint Martin 75003 Paris, France, e-mail: philippe.destuynder@cnam.fr

Caroline Fabre
Laboratoire de Mathématiques d'Orsay UMR 8628
Université Paris-Sud Bâtiment 425
91405 Orsay Cedex, France e-mail: caroline.fabre@psud.fr

1 Introduction

The domain that we consider in this simple example, is represented on figure 1 where several notations are specified. The propagation of antiplan waves is modelled by the following system of equations where the antiplan displacement u is the unknown ($\Omega = \Omega_+ \cup \Gamma_i \cup \Omega_-$):

$$\begin{cases} \dfrac{\partial^2 u}{\partial t^2} - \mathrm{div}(c^2 \nabla u) = f, \ \text{ in } \ \Omega \times]0,T[, \\ \dfrac{\partial u}{\partial \nu} = 0 \ \text{ on } \{\Gamma_+ \cup \Gamma_- \cup \Gamma_{i+} \cup \Gamma_{i-}\} \times]0,T[, \\ \dfrac{\partial u}{\partial t} + c\dfrac{\partial u}{\partial \nu} = 0 \ \text{ on } \ \{\Gamma_e \cup \Gamma_s\} \times]0,T[, \\ u(x,0) = u_0(x) \ \textit{ and } \ \dfrac{\partial u}{\partial t}(x,0) = u_1(x) \ \text{ in } \ \Omega. \end{cases} \tag{1}$$

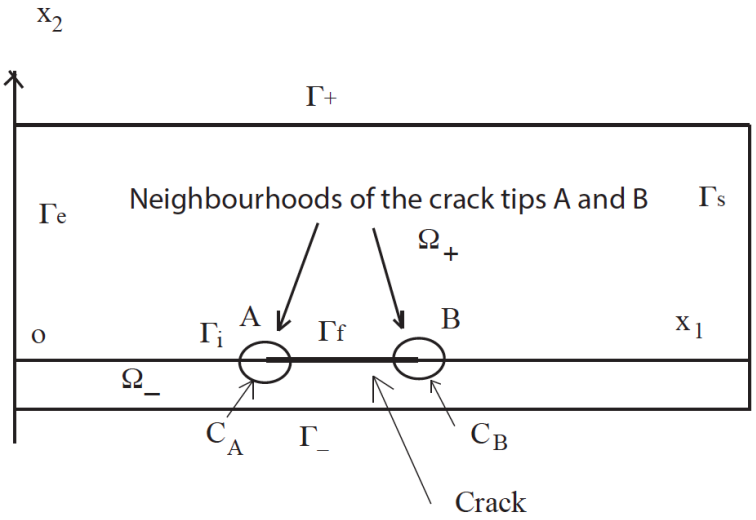

Fig. 1 The domain on which the antiplane model is set

The existence, uniqueness and time regularity of a solution are almost standard assuming that the initial conditions and the right hand side are smooth enough [6].

The space regularity is not true for two reasons. One is the presence of the crack tips (points A and B); the second one is the artificial singularities which appear on the two boundaries Γ_e and Γ_s at the intersection with the separation line (say Γ_i on figure 1). The last phenomenon should be eliminated from the solution because it has no physical meaning and pollutes the crack detection criterion suggested in this paper.

The use of Love waves [1] (by selecting them from the initial conditions or from the right hand side of the model) has three advantages described in the caption of figure 2.

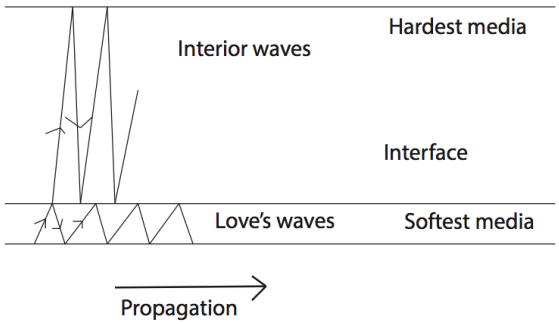

Fig. 2 Propagation phenomenon of Love waves. • They propagate far without a loss of energy. • Their energy is mainly localized in the weak part of the structure and therefore their influence is mainly measured in the corresponding part of Γ_e and Γ_s. • They propagate quite fast (for a slim strip), following a broken trajectory (see figure 2) in the weak media detecting therefore the presence of the crack.

2 The detection criterion

Using an energetical invariant deduced from domain derivative technics, one can prove the following result which leads to the definition of a crack detection criterion and even of a localisation strategy.

Theorem 1. *Let us consider the Fourier transform $\hat{u}$ of u. Let K_A and K_B the two stress intensity factors for the two crack tips and let us assume for instance that the function f is*

$$f(x,t) = \frac{2(\sin(\omega_2 t) - \sin(\omega_1 t)}{t})\eta(x)$$

where η is a smooth function with support in Ω_- or Ω_+. Thus one has:

$$\frac{1}{2}\int_{\Gamma_e \cup \Gamma_s} [-2\omega^2|\hat{u}|^2 + c^2|\frac{\partial \hat{u}}{\partial x_2}|^2]\nu_1 + \int_S \frac{\partial \eta}{\partial x_1}\hat{u}_R = \frac{\pi}{8}(c_+^2 + c_-^2)(|\hat{K}_A|^2 + |\hat{K}_B|^2) \overbrace{=}^{def} G(\omega, a, b)$$

Hence, if $G > 0$, $\forall \omega \in \omega_2 - \omega_1$, the existence of a crack is equivalent to $G > 0$. Finally the following optimal control problem is suggested in order to localize the crack (assuming that there is only one, and that ω_1 and ω_2 are correctly chosen):

$$\min_{l_1, l_2} \int_{\omega_1}^{\omega_2} G(\omega, l_1, l_2) d\omega + \frac{\varepsilon}{2}[l_1^2 + (l_2 - l_1)^2] \tag{2}$$

3 The artificial singularity due to the change of wave velocities

The boundary condition which should be satisfied by u near the point O (interface between Ω_+ and Ω_- on Γ_e) are: A local computation enables one to prove that the

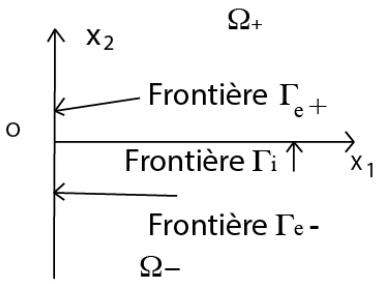

Fig. 3 On Γ_e one has: $\frac{1}{c}\frac{\partial u}{\partial t}$ which is discontinuous and thus $\frac{\partial u}{\partial \nu}$ is also discontinuous. This implies that u can't have the same regularity as inside the domain Ω.

singularity is a Dilog one. This strange phenomenon should be controled because it doesn't correspond to a physical one. Because it is known, and it can be introduced in the numerical scheme and a filttering process is used (projection of u on the orthogonal space to the singularity) in order to cancel it.

4 Description of the talk

The goal of this presentation would be to describe in more details the strategy described here and few numerical simulations will illustrate the foundation of the method. After a brief discussion on the Love waves, the invariant of the wave equation which is at the origin of the detection criterion will be analyzed. The optimal control model is handled through a gradient algorithm and it rests on the definition of an adjoint state variable. The non-physical singularities which appear on the two extrem boundaries will be discussed and their numerical effect shown on examples. Finally the numerical model and therefore the non destructive testing strategy will be explained.

References

1. A. E. H. Love , : Some Problems of Geodynamics, *Cambridge University Press, Cambridge*, 1911.
2. G. Diot, A. Kouadri-David, L. Dubourg, J. Flifla, S. Guegan and E. Ragneau, : Mesures de défauts par ultrasons laser dans des soudures d'alliage d'aluminium, *Internal report from Institut Maupertuis and INSA de Rennes*, 2013.
3. J. O. Kim, : Love waves in layered medium, *J. Acoust. Soc. Am.*, V. 91, p. 3099-3103, 1992.
4. X. P. Li, : Attenuation dispersion of Love waves in a two layered half space, *Wave Motion*, V. 22, p. 349, 1995.
5. D. Royer and E. Dieulesaint, : Ondes elastiques dans solides t. 1, *Masson*, 1996.
6. Ph. Destuynder and C. Fabre: Singularities and transparent boundary conditions for bimaterials, *Preprint*, 2014.

Exact transparent boundary conditions for diffraction problems in some anisotropic plates

V. Baronian[2], A.S. Bonnet-Ben Dhia[1], S. Fliss[1], A. Tonnoir[1,*]

Abstract In this paper, we propose an original method for constructing transparent boundary conditions in some anisotropic plates for the time-harmonic diffraction problem by a lineic defect. We suppose that the anisotropy enables to decouple the computation of the *SH* and the *P-SV modes* in the safe part of the plate. Then, we construct adapted impedance operators from which we derive original transparent conditions on artificial boundaries.

1 Introduction

The use of guided waves in non destructive testing (see [2]) presents many advantages that motivate their study. For instance, guided waves allow to control structures on wide distances and in inaccessible areas. However, the complexity of the experimental results requires accurate simulation tools to interpret them. The usual configuration is to consider an infinite and perfectly uniform waveguide except in a bounded area that contains a defect and we want to compute the diffraction of an incident wave by this localized defect.

More specifically, we are interested in the time-harmonic diffraction problem in an anisotropic elastic plate of an incident mode by an invariant (in one direction) defect (see figure 1). This particular problem has been studied in [5] and can be formulated as a 2D problem, for a vectorial unknown with 3 components. The technique developed consists in computing the modes thanks to the SAFE method (see [1, 3]) and derive from them transparent conditions (denoted by *TBC*) that enable to restrict the computational domain to a bounded area around the cross-section of the defect. The drawback of this method is that, for general anisotropy, there is no bi-orthogonality relation between the outgoing modes as the Fraser's relation for orthotropic media (see [1]). Therefore, the projection of the solution on the family of modes, which is required to compute the *TBC*, is not obvious and implies the inversion of a (possibly ill-conditioned) Gram matrix associated to the modes.

In our work, we propose to focus on particular cases of anisotropic plates for which we can decouple the calculations (in the uniform part) of the modes polarized in the (x_1, x_3) plane (denoted by *P-SV modes*), and of the shear modes polarized in x_2 (denoted by *SH modes*). The *SH modes* can be analytically obtained and verify an

[1] POEMS (UMR 7231 CNRS-ENSTA-INRIA)
· *Email: antoine.tonnoir@ensta.fr
· [2] CEA, LIST, Gif-sur-Yvette, France

original orthogonality relation on oblique boundaries. Besides, we need to use the SAFE method to numerically compute the *P-SV modes*. Classically, these modes verify a bi-orthogonality relation with the adjoint basis but this relation involves the stress components of the modes. To get rid of this difficulty, we propose to construct *TBC* on separate boundaries so that we can eliminate the stress parts.

2 Decoupling of *SH* and *P-SV waves*

We consider a homogeneous anisotropic elastic plate with free boundary conditions occupying the domain $\Omega = R^2 \times [-h,h]$. In time harmonic regime of pulsation ω, the displacement field $\mathbf{u}$ verifies the following classical equations:

$$\left| \begin{array}{ll} div\ \sigma(\mathbf{u}) + \omega^2 \rho \mathbf{u} = 0 & in \quad \Omega, \\ \sigma(\mathbf{u}).\nu = 0 & on\ \partial\Omega, \end{array} \right. \tag{1}$$

where ν denotes the outgoing normal. The stress $\sigma(\mathbf{u})$ is related to the displacement field by Hooke's law $\sigma(\mathbf{u}) = \mathbf{C}\varepsilon(\mathbf{u})$, where ε and $\mathbf{C}$ are the classical strain and elasticity tensors. Classically, if we consider solutions $\mathbf{u} = \mathbf{u}(x_1, x_3)$ independent of x_2, the problem (1) reduces to a $2D$ problem with 3 components. Thanks to the invariance, we prove by direct calculations that the components $\mathbf{u}_2$ and $(\mathbf{u}_1, \mathbf{u}_3)$ are decoupled (corresponding respectively to the *SH* and *P-SV waves*), providing that the elasticity tensor has the following form:

$$\mathbf{C} = \begin{pmatrix} C_{11} & C_{12} & C_{13} & \mathbf{0} & C_{15} & \mathbf{0} \\ C_{12} & C_{22} & C_{23} & C_{24} & C_{25} & C_{26} \\ C_{13} & C_{23} & C_{33} & \mathbf{0} & C_{35} & \mathbf{0} \\ \mathbf{0} & C_{24} & \mathbf{0} & C_{44} & \mathbf{0} & C_{46} \\ C_{15} & C_{25} & C_{35} & \mathbf{0} & C_{55} & \mathbf{0} \\ \mathbf{0} & C_{26} & \mathbf{0} & C_{46} & \mathbf{0} & C_{66} \end{pmatrix}. \tag{2}$$

We consider the diffraction by a defect which is invariant in the direction x_2 of an incident mode propagating in the direction x_1 normal to the defect. The final diffraction problem is still a $2D$ problem with 3 components, which may be coupled in the perturbed area corresponding to the cross-section of the defect.

3 Modes and *TBC* for *SH waves*

In that particular case of anisotropy (2), the transverse component $\mathbf{u}_2(x_1, x_3)$ verifies:

$$\left| \begin{array}{ll} \nabla^t(S_2 \nabla \mathbf{u}_2) + \omega^2 \mathbf{u}_2 = 0, & in \quad R \times [-h,h], \\ S_2 \nabla \mathbf{u}_2.\nu = 0 & on\ R \times \{x_3 = \pm h\}, \end{array} \right. \quad with \quad S_2 = \begin{pmatrix} C_{66}\ C_{46} \\ C_{46}\ C_{44} \end{pmatrix}, \tag{3}$$

where $\nabla = (\partial_{x_1}, \partial_{x_3})^t$. Looking directly for the modes $\mathbf{u}_2(x_1,x_3) = \phi(x_3)e^{i\beta x_1}$ leads to a quadratic eigenvalue problem for the eigenvalue β. A better approach consists in using the change of variables $(X_1,X_3) = (x_1 + \alpha x_3, x_3)$, where $\alpha = -\frac{C_{46}}{C_{44}}$. Then, the equations (3) become:

$$C^{'}\frac{\partial^2 \mathbf{u}_2}{\partial X_1^2} + C_{44}\frac{\partial^2 \mathbf{u}_2}{\partial X_3^2} + \omega^2 \mathbf{u}_2 = 0, \; in \quad R \times [-h,h], \tag{4}$$

where $C^{'} = C_{66} + 2\alpha C_{46} + \alpha^2 C_{44}$ and the boundary conditions simply reduce to $\partial_\nu \mathbf{u}_2 = 0$. Let us emphasize that the geometry is preserved by this change of variables. The calculation of modes is then classical and the two families of rightgoing and leftgoing modes (denoted with $+$ and $-$) are given by the following formulas:

$$SH_k^{\pm}(x_1,x_3) = e^{\pm i\beta_k(x_1+\alpha x_3)} cos(\gamma_k(x_3+h)), \quad with \quad \left| \begin{array}{c} \gamma_k = \frac{k\pi}{2h}, \\ \\ \beta_k = \sqrt{\frac{\omega^2 - C_{44}\gamma_k}{C^{'}}}. \end{array} \right. \tag{5}$$

An important property is that the two families of modes verify an **orthogonality relation** on oblique boundaries $\Sigma_a = \{x_1 + \alpha x_3 = a\}$ for any real a. So, knowing the traces of $\mathbf{u}_2|_{\Sigma_{\pm a}}$ on $\Sigma_{\pm a}$, the outgoing solutions in $\{\pm(x_1+\alpha x_3) \geq a\}$ are simply given by

$$\mathbf{u}_2 = \sum_{k\geq 0} SH_k^{\pm}\left(\mathbf{u}_2|_{\Sigma_{\pm a}}, SH_k^{+}\right)_{\Sigma_{\pm a}}. \tag{6}$$

From these analytical representations of the solution, we deduce the impedance operators $T_2^{\pm}$ that map the trace $\mathbf{u}_2|_{\Sigma_{\pm a}}$ to the normal trace $\partial_\nu \mathbf{u}_2|_{\Sigma_{\pm a}}$ on $\Sigma_{\pm a}$:

$$T_2^{\pm}(\mathbf{u}_2|_{\Sigma_{\pm a}}) = \sum_{k\geq 0} i\beta_k \left(\mathbf{u}_2|_{\Sigma_{\pm a}}, SH_k^{\pm}\right)_{\Sigma_{\pm a}} SH_k^{\pm}|_{\Sigma_{\pm a}},$$

and we can derive the *TBC*: $\partial_\nu \mathbf{u}_2 = T_2^{\pm}(\mathbf{u}_2|_{\Sigma_{\pm a}})$ on $\Sigma_{\pm a}$.

4 Modes and *TBC* for *P-SV waves*

The calculation of the *P-SV modes* requires to solve a coupled problem in $\mathbf{u}_1$ and $\mathbf{u}_3$. Using the ideas developed in [1, 4], this coupled problem can be formulated as an evolution problem in x_1:

$$\frac{\partial}{\partial x_1}(\mathbf{u}_1,\, \mathbf{u}_3,\, \mathbf{t}_1,\, \mathbf{t}_3)^t = \mathscr{A}(\mathbf{u}_1,\, \mathbf{u}_3,\, \mathbf{t}_1,\, \mathbf{t}_3)^t \tag{7}$$

where $\mathbf{t} = \sigma(\mathbf{u}) \cdot n$, $n = (1,0)^t$, and $\mathscr{A}$ is a differential operator in x_3. We are led to solve the linear eigenvalues problem $i\beta p = \mathscr{A} p$ in β, where $P(x_1,x_3) = e^{i\beta x_1} p(x_3)$ and $P = (\mathbf{u}_1,\, \mathbf{u}_3,\, \mathbf{t}_1,\, \mathbf{t}_3)^t$.

For general anisotropy, we do not have a bi-orthogonality relation between the outgoing modes $(P_k^{\pm})_k$ as in orthotropic media (see [1]). Therefore, we propose to use the adjoint modes $(P_k^*)_k$ which are the eigenfunctions of the adjoint operator $\mathscr{A}^*$, and which verify the classical bi-orthogonality relation $(P_k^{\pm}, P_l^*) = \delta_{k,l}$ on vertical boundaries $\Gamma_a = \{x_1 = a\}$. Then, knowing the traces and the normal stresses on $\Gamma_{\pm a}$, the solutions in $\{\pm x_1 \geq a\}$ can be expanded as

$$(\mathbf{u},\, \mathbf{t}) = \sum_{k\geq 0} P_k^{\pm} \left(P|_{\Gamma_{\pm a}}, P_k^*\right)_{\Gamma_{\pm a}} = \sum_{k\geq 0} P_k^{\pm} \left[\left(\mathbf{u}|_{\Gamma_{\pm a}}, \mathscr{U}_k^*\right)_{\Gamma_{\pm a}} + \left(\mathbf{t}|_{\Gamma_{\pm a}}, \mathscr{T}_k^*\right)_{\Gamma_{\pm a}} \right],$$

where $\mathscr{U}_k^*$ and $\mathscr{T}_k^*$ denote respectively the displacement and the stress parts of P_k^*. To derive *TBC* from these formulas, the idea is to replace the knowledge of the normal stress $\mathbf{t}$ on $\Gamma_{\pm a}$ by the knowledge of $\mathbf{u}$ in the boxes $B_l^{\pm}$ delimited by the boundaries $\Gamma_{\pm a}$ and $\Gamma_{\pm b}$, where $l = b - a$. Indeed, using the Green's formula inside $B_l^{\pm}$ and a lifting in $B_l^{\pm}$ of P_k^*, denoted by $\mathscr{L}(P_k^*)$, that vanishes on $\Gamma_{\pm b}$, we get

$$(\mathbf{t}|_{\Gamma_a}, \mathscr{T}_k^*)_{\Gamma_{\pm a}} = \int_{B_l^{\pm}} -\omega^2 \mathbf{u} \cdot \mathscr{L}(P_k^*) + \boldsymbol{\sigma}(\mathbf{u}) : \boldsymbol{\varepsilon}(\mathscr{L}(P_k^*)), \tag{8}$$

where we recall that $div\, \boldsymbol{\sigma}(\mathbf{u}) = -\omega^2 \mathbf{u}$, due to the equations verified by $\mathbf{u}$. Therefore, we can get the impedance operators $T_{1,3}^{\pm}$ that map $\mathbf{u}$ in $B_l^{\pm}$ to the normal stresses $\mathbf{t}$ on the boundaries $\Gamma_{\pm b}$ and derive the *TBC*.

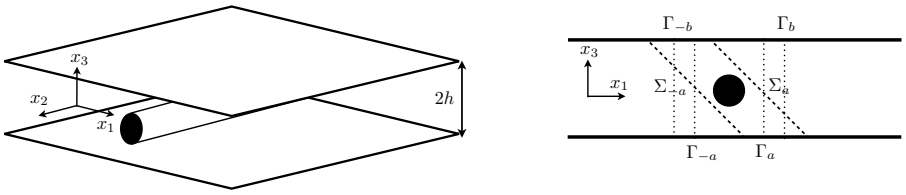

Fig. 1 Geometry of a typical configuration and notations.

References

1. Baronian V., Bonnet-Ben Dhia A.-S. and Lunéville E. 2010. *Transparent boundary conditions for the harmonic diffraction problem in an elastic waveguide*. J. Comput. Appl. Math., 234(6):1945–1952.
2. Lowe M.J.S. and Cawley P. 2006, *Long Range Guided Wave Inspection Usage Current Commercial Capabilities and Research Directions*, Int. Report, Imperial College London.
3. Liu G. R., Achenbach J. D., 1994 *A strip element method for stress analysis of anisotropic linearly elastic solids.* J. Appl. Mech. 62, pp. 607-613.
4. Pagneux V. and Maurel A. 2002. *Lamb wave propagation in inhomogeneous elastic waveguides. Proceedings of the Royal Society of London. Series A: Mathematical, Physical and Engineering Sciences*, 458(2024):1913–1930.
5. Taupin L. 2011. *Modélisation des méthodes ultrasonores de surveillance de structures aéronautiques instrumentées en vue de leur optimisation*. PhD thesis, Ecole Polytechnique.

Nonsmooth modal analysis of vibratory systems undergoing purely elastic impacts

Stéphane JUNCA and Mathias LEGRAND

Abstract The framework of nonlinear normal modes (NNM) [3, 4] is extremely powerful to investigate the nonlinear vibrations of mechanical systems. An autonomous thin vibrating rod in contact against a frictionless rigid foundation [5] is investigated in the form of a N-dof harmonic oscillator subjected to a purely elastic impact rule which preserves the total energy. We show that this system features a continuous set of periodic orbits supported by non-smooth sub-manifolds in the phase portrait.

1 Introduction

This work explores the free vibration of a one-dimensional oscillating rod undergoing rigid unilateral contact conditions. This is approximated through a N-dof spring-mass formulation together with a purely elastic impact rule. The corresponding free periodic solutions are targeted from the *modal analysis* standpoint: we study mathematically their existence as well as their stability, and compute them numerically. This topic has many applications in Mechanical Engineering where unilateral contact occurrences between mechanical components are becoming common due to the design of more flexible and lighter structures together with tighter operating clearances [5].

The mathematical theory behind initial value problems involving unilateral contact condition is sophisticated [9, 11, 1, 2]. Focusing on periodic solutions with one impact per period simplifies the formulation and a 2-dof system is investigated in [7] where NNM are explicitly calculated. Pilipchuck studied a N-dof system with symmetric barriers [8] through an ingenious and nonsmooth change of variables. Instead, we

Stéphane JUNCA, Université de Nice Sophia-Antipolis & INRIA, Labo. JAD (UMR CNRS 6621) & Team COFFEE, Parc Valrose, 06108 Nice, France. e-mail: junca@unice.fr

Mathias LEGRAND, McGill University, Department of Mechanical Engineering, 817 Sherbrooke Street West, Montréal, Québec H3A 0C3, Canada. e-mail: mathias.legrand@mcgill.ca

make use of a return map [7] and prove the existence of NNM near grazing contact [8]. The nonsmooth invariant manifolds supporting these NNM are also computed.

2 Models

2.1 One-dimensional continuous formulation

The system of interest is depicted in Fig. 1: it is a thin rode of length L and cross-sectional area A subjected to Signorini unilateral contact conditions at $x = L$. The main unknown is the displacement $u(x,t)$. It is governed by an initial-boundary value

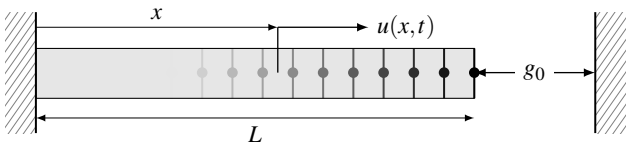

Fig. 1 Thin rode in contact against a rigid foundation and its discretization in space

formulation which takes the following form:

$$\rho\,\partial_{tt}u - E\,\partial_{xx}u = 0, \quad \forall x \in]0,L[\tag{1}$$

$$u(0,t) = 0 \tag{2}$$

$$u(L,t) \leq g_0 \quad ; \quad (u(L,t) - g_0)\cdot\sigma(L,t) = 0 \quad ; \quad \sigma(L,t) \leq 0 \tag{3}$$

where $\sigma(L,t) = EA\partial_x u(L,t)$; E is Young's modulus from linear elasticity considerations. This problem is mathematically studied in [10] and numerically approximated in [6]. The total energy [10] is preserved:

$$E(t) = \frac{1}{2}\int_0^L \left[\rho(\partial_t u)^2 + E(\partial_x u)^2\right] \mathrm{d}x = E(0) \tag{4}$$

Nonlinear normal modes are defined by continuous families of periodic solutions for which initial data are replaced by periodicity conditions in time [5]. In the present work, a simplified discrete version of the problem above is explored where the Signorini conditions are advantageously replaced by a purely elastic impact law.

2.2 Spring-mass discretization

The rod is approximated in space by a N-dof spring-mass system and the governing equations become

$$\mathbf{M}\ddot{\mathbf{u}}(t) + \mathbf{K}\mathbf{u}(t) = \mathbf{B}^{\top}\lambda(t) \tag{5}$$

$$u_N(t) \leq d \quad ; \quad \lambda \leq 0 \quad ; \quad (d - u_N(t))\lambda(t) = 0 \tag{6}$$

We study solutions where conditions (6) and the conservation of the total energy are simplified by the impact reflexion rule:

$$u_N(t) = d \quad \Longrightarrow \quad \dot{u}_N^+(t) = -\dot{u}_N^-(t) \tag{7}$$

3 Nonsmooth invariant manifold

Near the gazing contact, we can compute *periodic solutions with increasing energy*: figure 2 displays the second mode of vibration of a 3-dof spring-mass system reflecting the rod's dynamics. When unilateral contact is not activated, *ie* for small modal

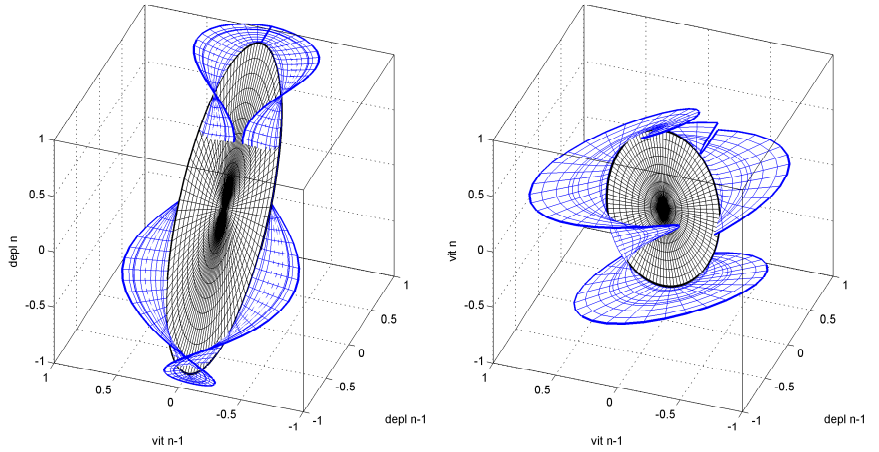

Fig. 2 Cross-section in the phase portrait of the invariant manifold supporting the second mode of vibration of a 3-dof spring-mass system undergoing one impact per period. Left: $(u_2, \dot{u}_2, u_3)$; right: $(u_2, \dot{u}_2, \dot{u}_3)$. Black shows the linear behavior while blue shows the nonlinear behavior. Grazing occurs at the boundary separating the two behaviors.

amplitudes, the system behaves linearly and the sub-manifold is flat (black portion in figure 2). On the contrary, when modal amplitudes are sufficiently large to activate unilateral contact, the sub-manifold becomes non-differentiable in displacement and even discontinuous in velocity (blue portion in figure 2). Other periodic solutions are expected with more than one impact per period, for instance.

References

1. P. Ballard: The dynamics of discrete mechanical systems with perfect unilateral constraints, *Archive for Rational Mechanics and Analysis*, Vol. 154, p. 199–274, 2000.
2. J. Bastien; F. Bernardin; C.-H. Larmarque: Non Smooth Deterministic or Stochastic Discrete Dynamical Systems: Applications to Models with Friction or Impact. *Mechanical Engineering and Solid Mechanics Series, Wiley*, 2013.
3. D. Jiang; C. Pierre; S.W. Shaw: Large-amplitude non-linear normal mode of piecewise linear systems, *Journal of Sound and Vibration*, Vol. 272, p. 869-891, 2004.
4. G. Kerschen; M. Peeters; J.C. Golinval; A.F. Vakakis: Nonlinear normal modes, Part I: A useful framework for the structural dynamics, *Mechanical Systems and Signal Processing*, Vol. 23, p. 170-194, 2009.
5. D. Laxalde; M. Legrand: Nonlinear modal analysis of mechanical systems with frictionless contact interfaces. *Computational Mechanics*, Vol. 47, p. 469–478, 2011.
6. L. Paoli; M. Schatzman: Numerical simulation of the dynamics of an impacting bar, *Computer Methods in Applied Mechanics and Engineering*, Vol. 196, p. 2839–2851, 2007.
7. M. Pascal: Dynamics and stability of a 2 dof oscillator with an elastic stop, *Journal of Computational and Nonlinear Dynamics*, 2006.
8. V. N. Pilipchuck: Impact modes in discrete vibrating systems with rigid barriers. *International Journal of Non-Linear Mechanics*, Vol. 36, p. 999-1012, 2001.
9. M. Schatzman: A Class of Nonlinear Differential Equations of Second Order in Time, *Nonlinear Analysis, Theory, Methods & Applications*, Vol. 2, p. 355–373, 1978.
10. M. Schatzman: Un problème hyperbolique du 2ème ordre avec contrainte unilatérale: la corde vibrante avec obstacle ponctuel, *Journal of Differential Equations*, Vol. 36, p. 295–334, 1980.
11. M. Schatzman: Uniqueness and continuous dependence on data for one dimensional impact problems, *Mathematical and Computational Modelling*, Vol. 28, p. 1–18, 1998.

Nonlinear elasticity and slow dynamics: physical and numerical modeling

N. Favrie and B. Lombard and C. Payan

Abstract Longitudinal vibrations in bar sedimentary rocks or damaged materials are examined. These materials exhibit time-dependent properties where two processes coexist: a fast process at the frequency of the excitation, governed by nonlinear elasticity; a slow process, governed by the evolution of defects. A ”soft-ratchet” model is proposed to describe the experimental observations. The properties of this model are analysed. A time-domain numerical modeling is also developed.

1 Introduction

Longitudinal vibrational experiments in sedimentary rocks or in concrete reveal that two radically-different dynamics coexist [1, 2, 7]. First, a ”fast” elastic dynamics occurs with a time scale ruled by the frequency of the excitation. Second, a ”slow” dynamics governs the relaxation of physical parameters, such as the Young's modulus. Some phenomenological models have been proposed to describe such hysteretic behaviors, for instance the Preisach-Mayergoyz model, but without any physical foundation [4].

Here, we present a ”soft-ratchet” model initially introduced in [8] and physically meaningfull. The softening/recovering of elastic modulus is related to the concentration of defects that evolves dynamically with the applied stress. This relaxation mechanisms is coupled to a law of nonlinear elasticity, for instance the widely-used

Nicolas Favrie
IUSTI, UMR CNRS 7343, 5 rue Enrico Fermi, 13453 Marseille, e-mail: nicolas.favrie@univ-amu.fr

Bruno Lombard
LMA, 31 chemin Joseph Aiguier, 13402 Marseille, e-mail: lombard@lma.cnrs-mrs.fr

Cédric Payan
LMA, 31 chemin Joseph Aiguier, 13402 Marseille, e-mail: cedric.payan@univ-amu.fr

Landau's model [3]. Lastly, viscoelasticity is introduced in the model. Our contribution is two-fold:

- improvement of the physical model. A non-physical feature of the soft-ratchet model [8] is fixed. Moreover, the generalized Zener model introduced in this paper is more realistic than the Stokes model in [8], and also better suited to numerical resolution;
- construction of a numerical scheme. Analytical tools used in [8] were unable to solve the full coupled system. On the contrary, we develop here a numerical strategy that enables to solve the whole equations, in the time-domain.

The sketch of the paper is as follows. First, we introduce the physical model and its basic features: evolution of defects, nonlinear elasticity, and attenuation. Second, the evolution equations are written as a first-order system of partial differential equations, whose properties are stated. Third, the numerical method is introduced, based on a splitting strategy. The hyperbolic step is solved by a Godunov scheme, whereas the relaxation step is solved exactly. Fourth and last, numerical experiments show that the experimental observations performed by Dynamic Acousto-Elastic Testing are qualitatively recovered [5, 6].

References

1. R.A. Guyer, P.A. Johnson, Nonlinear mesoscopic elasticity: Evidence for a new class of materials, *Physics Today* 52 (1999), 30-35.
2. P.A. Johnson, B. Zinszner, P.N.J. Rasolofosaon, Resonance and elastic nonlinear phenomena in rock, *J. Geophys. Res.*, 101 (1996), 11553-11564.
3. L. Landau, E. Lifchitz, Thorie de l'lasticit, Editions Mir (1967).
4. C. Pecorari, D.A. Mendelsohn, Forced nonlinear vibrations of a one-dimensional bar with arbitrary distributions of hysteretic damage to appear in *J*. Nondestruct. Eval. (2014).
5. G. Renaud, P.Y. Le Bas, P.A. Johnson, Revealing highly complex elastic nonlinear (anelastic) behavior of Earth materials applying a new probe: Dynamic acoustoelastic testing, *J*. Geophys. Res., 117, B06202 (2012).
6. J. Riviere, G. Renaud, R.A. Guyer, P.A. Johnson, Pump and probe waves in dynamic acoustoelasticity: Comprehensive description and comparison with nonlinear elastic theories, *J*. Appl. Phys., 114, 054905 (2013).
7. J.A. Ten Cate, T.J. Shankland, Slow dynamics in the nonlinear elastic response of Berea sandstone, *G*eophys. Res. Lett., 23-21 (1996), 3019-3022.
8. O.O. Vakhnenko, V.O. Vakhnenko, T.J Shankland, Soft-ratchet modeling of end-point memory in the nonlinear resonant response of sedimentary rocks, *P*hysical Review B71 (2005), 174103.

Reflection and transmission at the junction between two sections of circular cylindrical shell

Ryan M Pullen and Jane B Lawrie

1 Introduction

Acoustic propagation in circular cylindrical shells has been extensively studied. A wide range of model problems have been addressed including those involving shells with ribs, bulk-heads or other stiffeners, the radiation of sound by finite shells and scattering in coated pipes. A number of solution methods have been employed including asymptotic methods, modal methods, the Wiener-Hopf technique and numerical mode-matching. With the exception of the numerical approach, these methods are not easily extended to deal with problems involving closed waveguides with an abrupt change in radius. For the two-dimensional case there is a well established theory underpinning the existence and application of generalised orthogonality relations. This has recently been extended to three-dimensional problems involving ducts of rectangular cross-section, enabling mode-matching methods to be developed for ducting systems with flexible boundaries [1].

In this paper a prototype problem involving acoustic scattering in a circular cylindrical waveguide with abrupt change in radius is considered. The interior region of the structure contains a compressible fluid of sound speed c and density ρ whilst the exterior region is in-vacuo. Harmonic time dependence, $e^{-i\omega t}$, is assumed with $\omega = ck$, where k is the fluid wavenumber, and the boundary value problem is non-dimensionalised using k^{-1}, ω^{-1} as typical length and time scales. (Note: henceforth an overbar indicates a dimensional quantity, so $a = k\bar{a}$ etc.) A generalised orthogonality relation (OR) for the eigenmodes is presented and used to reduce the problem to a system of equations which is truncated and solved numerically.

Ryan M Pullen
Department of Mathematics, Brunel University, Uxbridge, UB8 3PH, e-mail: ryan.pullen@brunel.ac.uk

Jane B Lawrie
Department of Mathematics, Brunel University, Uxbridge, UB8 3PH e-mail: jane.lawrie@brunel.ac.uk

2 The boundary value problem and its solution

The model geometry comprises two semi-infinite sections of thin, flexible shell which occupy the regions $r = a$, $z < 0$ and $r = b$, $z > 0$ respectively of a cylindrical polar co-ordinate system (r, θ, z). The waveguide is closed by a rigid-plate which occupies $z = 0$, $a \le r \le b$. An axi-symmetric fluid-structure coupled mode propagates in the positive z direction towards $z = 0$. It is appropriate to define velocity potentials: $\phi_1(r,z)$ for $z < 0$, $0 \le r \le a$ and $\phi_2(r,z)$ for $z > 0$, $0 \le r \le b$. Both satisfy the non-dimensionalised Helmholtz's equation. The motion of the "left hand" cylindrical shell is governed by the axi-symmetric Donnell-Mushtari equations [2]:

$$\partial_{zz}^2 u_1 + (i\nu/a)\partial_{rz}^2 \phi_1 + \beta^2 u_1 = 0, \qquad r = a,\ z < 0 \tag{1}$$

$$-i\tau_1 \nu a\, \partial_z u_1 + \partial_{rzzzz}^5 \phi_1 - \mu_1^4 \partial_r \phi_1 + \tau_1 a^2 \beta^2 \rho/(\rho_s h k)\phi_1 = 0,\ \ r = a,\ z < 0 \tag{2}$$

where $u_1(z)$ is the longitudinal component of the shell displacement, $\bar{h}$ is the shell thickness and $\beta = c/c_s$, $\tau_1 = 12/(\bar{h}^2 k^2 a^2)$, $\mu_1^4 = \tau_1(a^2\beta^2 - 1)$. Here ν is Poisson's ratio, ρ_s is the shell density and $c_s = \{E/[\rho_s(1-\nu^2)]\}^{1/2}$ (E is Young's modulus) is the sound speed within the shell wall. The boundary conditions for the shell lying in $z > 0$ are obtained by replacing a, τ_1, u_1 and ϕ_1 with b, τ_2, u_2 and ϕ_2.

At the junction between the two sections of duct, the non-dimensional pressure is continuous, ie. $\phi_1 = \phi_2$, $z = 0$, $0 \le r \le a$. Further, the normal component of velocity is continuous within the fluid and zero on the rigid plate. It is assumed the edges of the shell are clamped to the rigid plate at $z = 0$. Thus, $w_j = w_{jz} = u_j = 0$, where the conditions are applied at $z = 0$, $r = a$ for $j = 1$ and $z = 0$, $r = b$ for $j = 2$.

The velocity potential $\phi_1(r,z)$ can be expressed as an eigenfunction expansion:

$$\phi_1(r,z) = F_\ell J_0(\gamma_\ell r) e^{i\eta_\ell z} + \sum_{n=0}^{\infty} A_n J_0(\gamma_n r) e^{-i\eta_n z},\ \ 0 \le r \le a,\ \ z < 0 \tag{3}$$

where $J_0(\cdot)$ denotes the Bessel function of the first kind, $\gamma_n = (1-\eta_n^2)^{1/2}$, $F_\ell = [\alpha/(a\eta_\ell C_\ell)]^{1/2}$ is the amplitude of the incident mode (chosen such that the incident power is unity) and A_n, $n = 0, 1, 2, \ldots$ are the reflection coefficients. Similarly:

$$\phi_2(r,z) = \sum_{n=0}^{\infty} B_n J_0(\kappa_n r) e^{is_n z},\ \ 0 \le r \le b,\ \ z > 0 \tag{4}$$

where $\kappa_n = (1-s_n^2)^{1/2}$ and B_n, $n = 0, 1, 2, \ldots$ are the transmission coefficients.

The quantities η_n, $n = 0, 1, 2 \ldots$ of (3) are the roots of $K_1(\eta) = 0$ where

$$K_1(\eta) = \tau_1 \nu^2 \eta^2 + (\eta^2 - \beta^2)\left\{\eta^4 - \mu^4 - \alpha J_0(\gamma a)/[\gamma J_1(\gamma a)]\right\}, \tag{5}$$

with $\gamma = (1-\eta^2)^{1/2}$ and $\alpha = 12\beta^2\rho/(\rho_s h^3 k^3)$. Positive roots, $+\eta_n$, are either positive real or have a positive imaginary part. They are ordered sequentially, real roots first and then by increasing imaginary part. Hence, η_0 is the largest real root. It is assumed that no root is repeated. The quantities s_n, $n = 0, 1, 2 \ldots$ of equation (4) are

the roots of $K_2(s)=0$ where $K_2(s)$ is obtained from (5) on replacing η, γ, a, τ_1 with s, κ, b, τ_2.

The generalised OR for a thin, flexible-walled, shell of radius $r=a$ is

$$\frac{\alpha}{a}\int_0^a J_0(\gamma_n r)J_0(\gamma_m r)r\mathrm{d}r = \delta_{mn}C_n + \left\{2-\gamma_m^2-\gamma_n^2-\frac{\tau_1\nu^2\beta^2}{(\eta_n^2-\beta^2)(\eta_m^2-\beta^2)}\right\}\gamma_n J_1(\gamma_n a)\gamma_m J_1(\gamma_m a), \tag{6}$$

with

$$C_n = -\frac{\gamma_n J_1(\gamma_n a)}{2\eta_n(\eta_n^2-\beta^2)}\frac{d}{d\eta}K_1(\eta)\bigg|_{\eta=\eta_n}, \tag{7}$$

where δ_{mn} is the Kronecker delta. The OR for the duct lying in $z>0$ is identical in structure and is obtained on replacing a, τ_1, η_n, γ_n, C_n with b, τ_2, s_n κ_n, D_n.

On substituting (3) and (4) into the pressure condition, multiplying both sides by $\alpha J_0(\gamma_m r)r/a$, integrating over the range $0\le r\le a$ and using (6), it is found that

$$A_m = -F_\ell\delta_{m\ell} + \frac{J_1(\gamma_m a)}{C_m}\left\{E_0+\frac{E_1}{\eta_m^2-\beta^2}+(\gamma_m^2-2)E_2\right\} + \frac{\alpha}{a}\sum_{n=0}^{\infty}\frac{B_n R_{mn}}{C_m} \tag{8}$$

where E_0-E_2 are constants and

$$R_{mn} = \int_0^a J_0(\gamma_m r)J_0(\kappa_n r)r\mathrm{d}r. \tag{9}$$

On using the edge conditions, it is found that $E_0=0$ and

$$E_j = \frac{1}{\Delta}\left\{2F_\ell\Omega_{j\ell}\eta_\ell\gamma_\ell J_1(\gamma_\ell a) - \frac{\alpha}{a}\sum_{m=0}^{\infty}\sum_{n=0}^{\infty}\frac{B_n\Omega_{jm}R_{mn}\eta_m\gamma_m J_1(\gamma_m a)}{C_m}\right\},\ \ j=1,2, \tag{10}$$

where $\Delta = S_1^2+S_0S_2$, $\Omega_{jm}=S_j-S_{j-1}/(\beta^2-\eta_m^2)$ with

$$S_j = \sum_{n=0}^{\infty}\frac{\eta_m\gamma_m^2 J_1^2(\gamma_m a)}{(\beta^2-\eta_m^2)^j C_m},\ j=0,1,2,\ \text{and}\ S_3=\sum_{m=0}^{\infty}\frac{\kappa_m^2 J_1^2(\kappa_m b)}{s_m D_m}. \tag{11}$$

On substituting (3) and (4) into the velocity condition, multiplying through by $\alpha J_0(\kappa_m r)r/b$, integrating over $0\le r\le b$ and using the appropriate OR:

$$B_m = \frac{\alpha F_\ell\ \eta_\ell R_{\ell m}}{b s_m D_m} + \frac{\kappa_m J_1(\kappa_m b)}{s_m D_m}\left\{E_3+\frac{E_4}{s_m^2-\beta^2}+(\kappa_m^2-2)E_5\right\} - \frac{\alpha}{b}\sum_{n=0}^{\infty}\frac{A_n\eta_n R_{nm}}{s_m D_m} \tag{12}$$

where E_3-E_5 are constants. In this case it is found that $E_4=E_5=0$ and

$$E_3 = -\frac{\alpha}{bS_3}\sum_{m=0}^{\infty}\frac{F_\ell\eta_\ell R_{\ell m}\kappa_m J_1(\kappa_m b)}{s_m D_m} + \frac{\alpha}{bS_3}\sum_{m=0}^{\infty}\sum_{n=0}^{\infty}\frac{A_n\eta_n R_{nm}\kappa_m J_1(\kappa_m b)}{s_m D_m}. \tag{13}$$

3 Numerical results and Discussion

The numerical results presented here are obtained by truncating equations (8) and (12), and solving using 100 terms. The shell parameters are $\rho_s = 2700$ kg m^{-3}, $E = 7.2 \times 10^{10}$ Nm^{-2}, $\nu = 0.34$, $\bar{h} = 0.002$m whilst $c = 343.5$ms^{-1} and $\rho = 1.2$ kg m^{-3}. The non-dimensional reflected ($\mathscr{E}_1$) and transmitted ($\mathscr{E}_2$) powers are given by

$$\mathscr{E}_1 = a\alpha^{-1} \sum_{n=0}^{N} |A_n|^2 C_n \eta_n \text{ and } \mathscr{E}_2 = b\alpha^{-1} \sum_{n=0}^{N} |B_n|^2 D_n s_n, \tag{14}$$

where $N+1$ is the number of cut-on modes. For this model problem there are two fundamental modes: the first (wavenumber η_0) is essentially fluid-borne whilst the second (wavenumber η_1) is structure-borne. Either mode can be used as forcing; the respective incident amplitudes are F_0 and F_1. Figure 1 demonstrates that when the

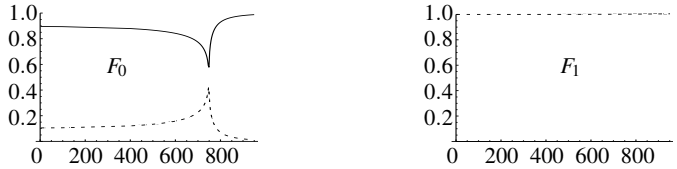

Fig. 1 Reflected (dashed) and transmitted (solid) powers for $\bar{a} = 0.2$m, $\bar{b} = 0.28$m

incident mode is fluid-borne, despite a sharp dip at the first cut-on (≈ 745Hz), the vast majority of the energy is transmitted. In contrast, when the incident mode is structure-borne the power is entirely reflected. Figure 2 shows $\mathscr{E}_1$ and $\mathscr{E}_2$ when the radius of the left-hand ($z < 0$) duct is significantly reduced. In this case, for fluid-borne forcing, much of the power is reflected at frequencies below the first cut-on and there is a sharp inversion of $\mathscr{E}_1$ and $\mathscr{E}_2$ at the first cut-on. Again, the power is entirely reflected for structure-borne forcing.

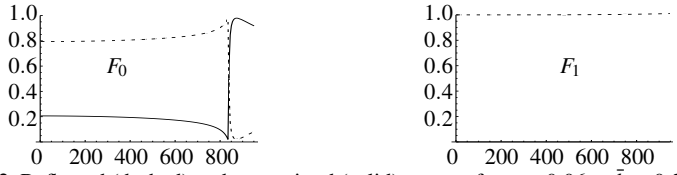

Fig. 2 Reflected (dashed) and transmitted (solid) powers for $\bar{a} = 0.06$m, $\bar{b} = 0.25$m

References

1. J.B. Lawrie: On acoustic propagation in three-dimensional rectangular ducts with flexible walls and porous linings, *J.* Acoust. Soc. Am., **131(3)**, 1890-1901, 2012.
2. M.C. Junger and D. Feit: Sound, structures, and their interaction, *MIT Press*, p. 216-218, 1972.

Low Mach number flow noise from a two-dimensional rough circular cylinder

David Nigro, I.D. Abrahams

Abstract The purpose of this work is to evaluate the effect of roughness on the cross-flow noise around a circular cylinder with an application to towed array sonar noise. It is shown that, for a low Mach number flow, it is characterized by a dipole source involving the surface pressure. If the roughness is small compared to the acoustic wavenumber, and if the surface pressure is statistically spatially homogeneous, the far-field pressure power spectral density (PPSD) is given by a discrete convolution of the wall pressure power spectral density (WPPSD) with a filter function that is purely geometric. This filter function only involves the azimuthal Fourier coefficients of the roughness shape function and its gradient, as well as the Green's function tailored to the smooth geometry.

1 Introduction

Roughness noise is of increasing interest in the aircraft industy as well as in the underwater industry. Most of the models used in hydroacoustics assume a smooth geometry. However, in practice, we cannot avoid some roughness during the industrial manufacturing process. Therefore it is important to be able to quantify the effect of roughness on the noise radiated by turbulent flows over objects. It has been shown experimentally (for the rotating cylinder by Skudrzyk & Haddle [1] and the rotating disk by Chanaud [2]) and theoretically over infinite geometries (for the infinite plate by Glegg & Devenport [3]) that roughness noise is dipolar.

In this paper we will revisit the classical problem of the cross-flow noise around a smooth circular cylinder to incorporate roughness effects. The smooth geometry has been widely studied both experimentally and numerically over the past few decades

David Nigro
University of Manchester, Oxford Rd, M13 9PL e-mail: david.nigro@manchester.ac.uk

I.D. Abrahams
University of Manchester, Oxford Rd, M13 9PL e-mail: i.d.abrahams@manchester.ac.uk

[4] and it is well-known that, at low Mach numbers, the main contribution to the radiated noise comes from the scattering of the fluctuating Reynolds stress tensor by the cylinder and that this contribution is dipolar.

2 Lighthill's analogy

The compressible Navier–Stokes equations for a viscous fluid free of external forces can be combined to give Lighthill's analogy [5]

$$\left(\nabla^2 - \frac{1}{c_0^2}\frac{\partial^2}{\partial t^2}\right)\rho = -\frac{1}{c_0^2}\frac{\partial^2 T_{ij}}{\partial x_i \partial x_j}, \tag{1}$$

where $T_{ij} = \left(\rho v_i v_j + \sigma_{ij} + (p - c_0^2\rho)\delta_{ij}\right) \approx \rho_0 v_i v_j$ at low Mach numbers. Physically this analogy means that the turbulent motion of the fluid is equivalent to a volume distribution of quadrupoles in a fluid otherwise at rest.

In some cases it is easier to work in the frequency domain, and this gives us an inhomogeneous Helmholtz equation

$$(\nabla^2 + k_0^2)\widetilde{\rho}(\mathbf{x},\omega) = -\frac{1}{c_0^2}\frac{\partial^2 \widetilde{T}_{ij}}{\partial y_i \partial y_j}, \tag{2}$$

where $k_0 = \dfrac{\omega}{c_0}$. This can then be solved using a Green's function, $\widetilde{G}$, to obtain

$$\widetilde{p}(\mathbf{x},\omega) = -\int_V \widetilde{T}_{ij}\frac{\partial^2 \widetilde{G}}{\partial y_i \partial y_j}\,\mathrm{d}V(\mathbf{y}) - \int_S \widetilde{p}\frac{\partial \widetilde{G}}{\partial n}\,\mathrm{d}S(\mathbf{y}). \tag{3}$$

We can see from (3) that the solution is independent of the choice of the Green's function. A popular choice is based on the Green's function tailored to the surface, $\widetilde{G}_t$, that satisfies $\dfrac{\partial \widetilde{G}_t}{\partial n} = 0$ on S, yielding

$$\widetilde{p}(\mathbf{x},\omega) = -\int_V \widetilde{T}_{ij}\frac{\partial^2 \widetilde{G}_t}{\partial y_i \partial y_j}\,\mathrm{d}V(\mathbf{y}). \tag{4}$$

This choice allows us to avoid evaluating the surface integral at the price of constructing a tailored Green's function, a task which can be very challenging for complicated geometries.

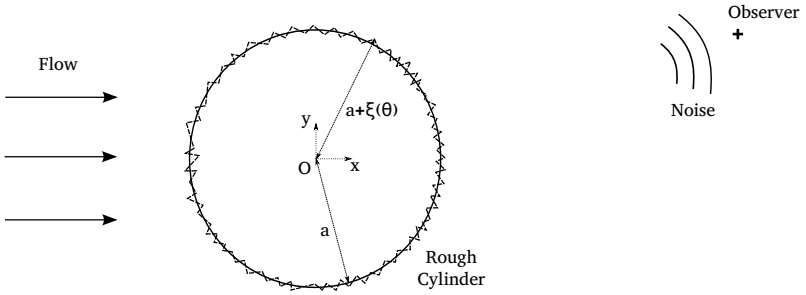

Fig. 1 The acoustic pressure perturbation is radiated away from a region of turbulent flow created by the 2D rough circular cylinder of radius $a+\xi(\theta)$.

3 2D rough cylinder

3.1 Model

The roughness is modelled as a pertubation, $\xi(\theta)$, to a smooth cylinder of radius a as shown in Fig. 1. It is considered small enough that it does not perturb the flow too much i.e. the sources are the same as for the smooth cylinder. We will use the Green's function, G_t, tailored to the smooth cylinder in (3) and keep only the linear terms in ξ. Therefore we neglect the effect of roughness in the volume integral as it can be shown that it is quadratic in ξ under the assumptions we have made. Therefore the effect of roughness is given by

$$\widetilde{p_r}(\mathbf{x},\omega) = -\int_{L(\xi)} \widetilde{p_L}(\mathbf{y},\omega)\nabla\widetilde{G_t}(\mathbf{x}|\mathbf{y},\omega).\mathbf{n}\,\mathrm{d}L. \tag{5}$$

3.2 Application

Using the Taylor expansion of the gradient of the tailored Green's function and projecting the integral onto the smooth geometry to highlight the effect of roughness gives the far-field pressure

$$\begin{aligned}\widetilde{p_r}(\mathbf{x},\omega) \approx &\sqrt{\frac{\pi}{2k_0 r_x}}\mathrm{e}^{\mathrm{i}\left(k_0 r_x+\frac{\pi}{4}\right)}\sum_{n=-\infty}^{\infty}\widetilde{p}_{Ln}(\omega)\\ &\times\sum_{m=-\infty}^{\infty}\mathrm{e}^{-\mathrm{i}m\left(\theta_x+\frac{\pi}{2}\right)}\left(k_0^2 ahB_m(k_0a)\xi_{n+m}^{(1)}-C_m(k_0a)\xi_{n+m}^{(2)}\right),\end{aligned} \tag{6}$$

where $\mathbf{x}=(r_x,\theta_x)$ is the observer's position in polar coordinates, $\widetilde{p}_{Ln}$ are the Fourier coefficients of the pressure fluctuations on the smooth cylinder, B_m and C_m are co-

efficients depending on the geometry of the smooth cylinder, $\tilde{\xi}^{(1)}_{m+n}$ and $\tilde{\xi}^{(2)}_{m+n}$ are the Fourier coefficients of the shape function and its gradient, respectively. The $\tilde{\xi}^{(1)}_{m+n}$ have been normalised by the r.m.s. of the roughness height, h, and the $\tilde{\xi}^{(2)}_{m+n}$ normalised by the radius of the cylinder.

Assuming that the turbulence is statistically stationary and homogeneous, there is a simple relationship between the PPSD, $\psi_{pp}(\mathbf{x},\omega)$, and the WPPSD, $\psi_{PP}(q,\omega)$, where q is some azimuthal mode numbers

$$\psi_{pp}(\mathbf{x},\omega) = \frac{\pi^2}{k_0 r_x} \sum_{n=-\infty}^{\infty} \Gamma_n \psi_{PP}(n,\omega), \tag{7}$$

and

$$\Gamma_n = \mathrm{Ex}\left[\left| \sum_{m=-\infty}^{\infty} \mathrm{e}^{-\mathrm{i}m(\theta_x+\frac{\pi}{2})} (k_0 a k_0 h B_m(k_0 a)\tilde{\xi}^{(1)}_{n+m} - C_m(k_0 a)\tilde{\xi}^{(2)}_{n+m}) \right|^2 \right]. \tag{8}$$

4 Conclusion

We adapted the model introduced by Devenport & Glegg [3] to a 2D cylindrical geometry and showed that roughness noise is indeed dipolar. However, the assumption that the sources are not modified by the roughness is questionable as the boundary layer over a cylinder is really sensitive to small perturbations. We also assumed that the turbulence was statistically stationary and homogeneous around the cylinder, which is unlikely as there are flow separations. Nonetheless this model allows us to evaluate the impact of roughness without having to recompute the source terms for each roughness configuration.

Acknowledgements This work is funded by Thales Underwater Systems Ltd and the EPSRC.

References

1. F.J. Skudrzyk, G.P. Haddle : Noise production in a turbulent boundary layer by smooth and rough surfaces, *J. Acoust. Soc. Am.*, 1960.
2. R.C. Chanaud: Experimental study of aerodynamic sound from a rotating disk, *J. Acoust. Soc. Am.*, 1969.
3. S. Glegg, W. Devenport: The far-field sound from rough wall boundary layers, *Proc. R. Soc. A*, 2009.
4. X. Gloerfelt & *al.*: Flow-induced cylinder noise formulated as a diffraction problem for low Mach numbers, *J. Sound Vib.*, 2005
5. M.J. Lighthill: On sound generated aerodynamically, *Proc. R. Soc. A*, 1952.

Solution of a moving contact problem of dynamic elasticity

M. Brun and L. I. Slepyan

Abstract We consider the problem of a rigid body moving in contact with an elastic half-space. The problem has been studied in the framework of linear elasticity and the general smooth frictionless solution has been obtained. We discuss the general conditions under which the rigid body meets zero driving force drawing a parallelism with the d'Alembert paradox for incompressible and inviscid potential flow. The steady-state general solution is obtained as the limit for the related transient problem which provides the necessary information regarding energy flux from infinity. Mathematically, the elastic solution is found solving a mixed problem for a single analytical function. The solution is based on the introduction of a new condition regarding energy fluxes at singular points in addition to the well-known Signorini conditions.

1 Introduction

The dynamic contact problem of a rigid indenter moving frictionless on a liner elastic half-space is considered. The steady-state problem was analysed in [2, 4, 1, 3] and the complete solution was found only for the sub-Rayleigh velocity regime. The super-Rayleigh, subsonic and intersonic regimes were discussed in [4, 1], where it was given evidence that it was not found a way to make the solutions to be unique

Michele Brun
Dipartmento di Ingegneria Meccanica, Chimica e dei Materiali, Universit di Cagliari, Via Marengo 2, 09123 Cagliari, Italy; e-mail: mbrun@unica.it
Department of Mathematical Sciences, University of Liverpool, Liverpool, L69 3BX, UK; e-mail: M.Brun@liverpool.ac.uk

L. Slepyan
Aberystwyth University, Department of Mathematics and Physics, Ceredigion SY23 3BZ, Wales
Tel Aviv University, School of Mechanical Engineering, IL-69978 Tel Aviv, Israel; e-mail: slepyanl@post.tau.ac.il

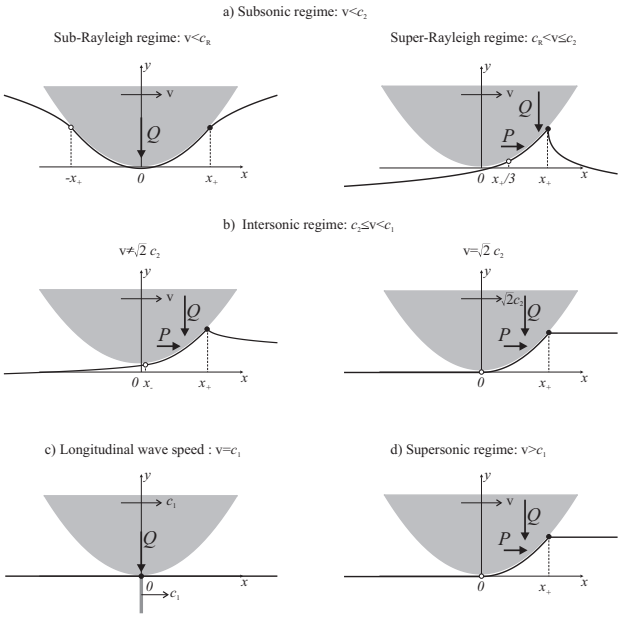

Fig. 1 The contact configurations in different speed regimes. The bold curve is the deformed elastic half-plane boundary. The leading, x_+, and the rear, x_-, end points of the contact region are marked by black and white circles, respectively. The localized longitudinal wave in equilibrium with the indenter is sketched in (c).

and/or physically accepted. We report here the conclusions in [4], "The present paper clearly raises many more questions than it solves, but these questions are very pressing and are apparently being neglected by the elastodynamic community. We shall have achieved our objective if we succeed in generating sufficient interest in this challenging problem to ensure that some progress will be made in the next 26 years." The objective was recently achieved by Slepyan and Brun in [5]. The above-mentioned non-uniqueness in the problem formulation was resolved adding to the well-known Signorini contact conditions, a condition concerning the energy-flux significant singular points in the stress-particle velocity field. Thus, the solutions is based on the following three conditions:

- *positive (tensile) normal contact stresses are not allowed*,
- *penetration of the elastic material into the indenter is not allowed*,
- *energy-source (active) singular points are not allowed.*

The steady-state solution is preceded by an analysis of the transient problem for the normal load moving along the elastic half-plane boundary. The transient solution allows to extract explicitly the general expressions of the normal traction and the derivative of the displacement trough a single analytical function. These expressions are used to address the mixed problem for a single region where the real part of an analytical function is given, whereas the imaginary part of this function is given

outside of this region (the dynamic contact problem for the half-plane). The use of the transient problem with zero initial conditions allows to exclude automatically the energy flux from infinity, which is important for intersonic and supersonic regimes.

2 Steady-state solution

The steady-state regime of a frictionless-contact of a smooth rigid body moving along the half-plane boundary is considered. The displacement and the stress are functions of the coordinates $x \leftarrow x - vt$ and y in a moving coordinate system. The plane strain dynamic problem is examined with the conditions at the boundary, $y = 0$

$$\begin{aligned} u'(x) &= y'(x), \quad x \in (x_-, x_+); \\ \sigma_{yy} &= 0, \quad x \notin (x_-, x_+); \\ u'(x) &= \mathrm{O}(1/|x|) \quad |x| \to \infty. \end{aligned} \tag{1}$$

For a parabolic indenter $y = x^2/2r$ (r is the local radius of curvature of the indenter) the contact configurations are given in Figure 1, while the contact stress distribution is given in Figure 2.

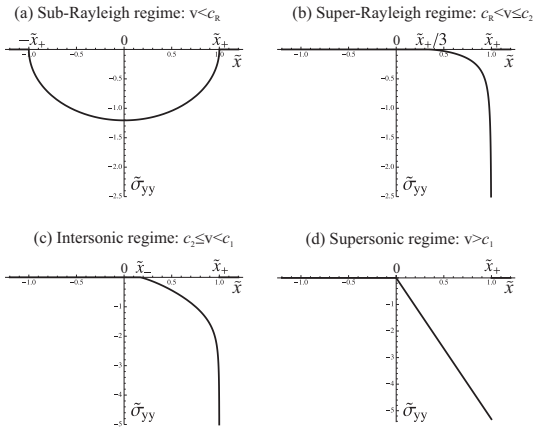

Fig. 2 The contact stress distributions as a function of the normalized coordinate $\tilde{x} = x/x_+$. The special case $v = \sqrt{2}c_2$ is the same as in the supersonic regime. In the super-Rayleigh subsonic (b) and in the intersonic (c) speed regimes, the leading end points of the contact zone, x_+, are singular. In (b) it is an energy absorbing square-root type point, whereas in (c) it is a weak point, which can neither absorb nor release energy.

3 Conclusion

The steady-state solution for an elastic half-plane under a moving frictionless smooth indenter of arbitrary shape is derived. Mathematically, the considered mixed problem is formulated and solved for a single region where the real part of an analytical function is given, whereas the imaginary part of this function is given outside of this region. The related steady-state problems of wedging of an elastic plane by a smooth rigid body and the movement of a finite rigid body along the interface of two elastic half-planes compressed together in the sub-Rayleigh regimes has been also investigated in [5]. Note that the analytical technique used in this paper is applicable for any number of the 'real-part' regions and for a periodic array of the real/imaginary (stress/displacement) regions. So the considered problems can also be solved, in the same way, for the contact zone consisting of several simply connected regions or of a periodic array of such regions.

Acknowledgements M.B. acknowledges the financial supports of the Regione Autonoma della Sardegna (LR7 2010, grant 'M4' CRP-27585) and of the European Community's Seven Framework Programme under contract numbers PIEF-GA-2011-302357-DYNAMETA.

References

1. Brock, L.M., 2002. Exact analysis of dynamic sliding indentation at any constant speed on an orthotropic or transversely isotropic half-space. *ASME J. Appl. Mech.* 69, 340-345.
2. Craggs, J.W., and Roberts, A.M., 1967. On the motion of a heavy cylinder over the surface of an elastic half-space. *ASME J. Appl. Mech.* 34, 207-209.
3. Galin, L.A. and Gladwell, G.M.L. 2008. Contact Problems. Springer.
4. Georgiadis, H.G., and Barber, J.R., 1993. On the super-Rayleigh/subsonic elastodynamic indentation problem. *Journal of Elasticity* 31, 141-161.
5. Slepyan, L., Brun, M. 2012: Driving forces in moving-contact problems of dynamics elasticity: indentation, wedging and free-sliding *J. Mech. Phys. Solids*, 60, 11, 1883-1996, 2012.

Attendees List **European Research Network** **Gregynog - 22nd to 27th June 2014**

Abrahams I. David	University of Manchester	i.d.abrahams@manchester.ac.uk
Bai Long	University of Bristol	lb13340@bristol.ac.uk
Barnwell Ellis	University of Manchester	ellis.barnwell@gmail.com
Baronian Vahan	CEA SACLAY	vahanbaronian@yahoo.fr
Brambley Edward	University of Cambridge	E.J.Brambley@damtp.cam.ac.uk
Brun Michele	University of Liverpool	mbrun@unica.it
Carta Giorgio	University of Cagliari	giorgio_carta@unica.it
Challis Richard	University of Nottingham	richard.challis@nottingham.ac.uk
Colquitt Daniel	Imperial College London	d.colquitt@imperial.ac.uk
Cunningham Laura	University of Strathclyde	l.cunningham@strath.ac.uk
Deschamps Marc	I2M - Université de Bordeaux /CNRS	m.deschamps@I2M.u-bordeaux1.fr
Desoudin Béatrice	I2M - Université de Bordeaux /CNRS	b.desoudin@i2m.u-bordeaux1.fr
Desoudin Philippe	I2M - Université de Bordeaux /CNRS	b.desoudin@free.fr
Destuynder Philippe	Conservatoire National des Arts et Métiers	philippe.destuynder@cnam.fr
Dubus Bertrand	IEMN dept ISEN / CNRS	bertrand.dubus@isen.fr
Forrester Michael	Loughborough University	d.m.forrester@lboro.ac.uk
Gauthier Camille	LOMC - CNRS Université du Havre	camille.gauthier@hotmail.fr
Gunn David	British Geological Survey	dgu@bgs.ac.uk
Habault Dominique	CNRS - LMA Marseille	habault@lma.cnrs-mrs.fr
Haslinger Stewart	University of Liverpool	Stewart.Haslinger@liverpool.ac.uk
Hernando Quintanilla Francisco	Imperial College London	francisco.hernando-quintanilla11@imperial.ac.uk
Huang Jinrui	Loughborough University	J.Huang@lboro.ac.uk
Huthwaite Peter	Imperial College London	p.huthwaite@imperial.ac.uk
Joyce Duncan	University of Manchester	duncan.joyce@manchester.ac.uk
Junca Stéphane	Laboratoire de Mathématiques JAD	junca@unice.fr
Kamta Djakou Audrey	CEA Saclay	audrey.kamta-djakou@cea.fr
Lawrie Jane	Brunel University	jane.lawrie@brunel.ac.uk
Leger Alain	CNRS - LMA Marseille	leger@lma.cnrs-mrs.fr
Li Wenqi	University of Nottingham	wenqi.li@nottingham.ac.uk
Lombard Bruno	CNRS - LMA Marseille	lombard@lma.cnrs-mrs.fr
Lowe Michael	Imperial College, London	m.lowe@imperial.ac.uk
Lubeigt Emma	CEA Cadarache	emma.lubeigt@cea.fr
Luppe Francine	LOMC - CNRS Université du Havre	francine.luppe@univ-lehavre.fr
Mansoura Sid Ali	LOMC - CNRS Université du Havre	sid-ali.mansoura@univ-lehavre.fr
Marrow Paul	University of Nottingham	eexpm10@nottingham.ac.uk
Massacret Nicolas	CNRS - LMA Marseille	nicolas.massacret@gmail.com
Mattesi Vanessa	INRIA / LMAP	vanessa.mattesi@inria.fr
Mora Pierric	I2M - Université de Bordeaux /CNRS	pierric.mora@u-bordeaux.fr
Mulholland Anthony	University of Strathclyde, Glasgow	anthony.mulholland@strath.ac.uk
Nigro David	University of Manchester	david.nigro@manchester.ac.uk
Pagneux Vincent	LAUM, CNRS Université du Maine	vincent.pagneux@univ-lemans.fr
Parnell William J.	University of Manchester	william.parnell@manchester.ac.uk
Peake Nigel	Cambridge University	n.peake@damtp.cam.ac.uk
Pichugin Aleksey	Brunel University	aleksey.pichugin@brunel.ac.uk
Pinfield Valerie	Loughborough University	v.pinfield@lboro.ac.uk
Pullen Ryan	Brunel University	ryan.pullen@brunel.ac.uk
Saidoun Abdelkrim	I2M - Université de Bordeaux /CNRS	abdelkrim.saidoun@u-bordeaux.fr
Sargent Cristina	Imperial College of London	cristina.sargent04@imperial.ac.uk
Selsil Ozgur	University of Liverpool	oselsil@liverpool.ac.uk
Shi Fan	Imperial College London	f.shi12@imperial.ac.uk
Tant Katy	University of Strathclyde	katy.tant@strath.ac.uk
Thompson Ian	University of Liverpool	ian.thompson@liv.ac.uk
Tonnoir Antoine	ENSTA - POEMS.	antoine.tonnoir@ensta.fr
Treyssède Fabien	IFSTTAR, Bouguenais	fabien.treyssede@ifsttar.fr
Yaacoubi Slah	Institut de Soudure, RDI CND	s.yaacoubi@institutdesoudure.com

***C**ommissariat à l'**E**nergie **A**tomique*

***C**entre **N**ational de la **R**echerche **S**cientifique*

*UK **R**esearch **C**entre in **N**on-**D**estructive **E**valuation*

Engineering and Physical Sciences Research Council

University of Manchester

Imperial College London

Université de Bordeaux

Institut de Mécanique et Ingénierie de Bordeaux

Laboratoire de Mécanique et d'Acoustique de Marseille

***I**nstitut **F**rançais des **S**ciences et **T**echnologies des **T**ransports, de l'**A**ménagement et des **R**éseaux*